

# Stellar Superfluids

Dany Page<sup>1</sup>, James M. Lattimer<sup>2</sup>, Madappa Prakash<sup>3</sup>, and Andrew W. Steiner<sup>4</sup>

<sup>1</sup> *Instituto de Astronomía, Universidad Nacional Autónoma de México,  
Mexico, DF 04510, Mexico*

<sup>2</sup> *Department of Physics and Astronomy, State University of New York at Stony Brook,  
Stony Brook, NY 11794-3800, USA*

<sup>3</sup> *Department of Physics and Astronomy, Ohio University,  
Athens, OH 45701-2979, USA*

<sup>4</sup> *Institute for Nuclear Theory, University of Washington,  
Seattle, WA 98195, USA*

## Abstract

Neutron stars provide a fertile environment for exploring superfluidity under extreme conditions. It is not surprising that Cooper pairing occurs in dense matter since nucleon pairing is observed in nuclei as energy differences between even-even and odd-even nuclei. Since superfluids and superconductors in neutron stars profoundly affect neutrino emissivities and specific heats, their presence can be observed in the thermal evolution of neutron stars. An ever-growing number of cooling neutron stars, now amounting to 13 thermal sources, and several additional objects from which upper limits to temperatures can be ascertained, can now be used to discriminate among theoretical scenarios and even to dramatically restrict properties of nucleon pairing at high densities. In addition, observations of pulsars, including their spin-downs and glitch histories, additionally support the conjecture that superfluidity and superconductivity are ubiquitous within, and important to our understanding of, neutron stars.

## 1 Introduction

In this contribution, we describe the roles of neutron superfluidity and proton superconductivity in the astrophysical setting of neutron stars, drawing upon lessons learned from similar phenomena occurring in laboratory nuclei. We will focus on both the thermal evolution (i.e., cooling) as well as the dynamical evolution (i.e., spin-down) of neutron stars. In the former, pairing dramatically affects neutrino emission processes and the specific heat of dense matter. In the latter, pairing may be responsible for the observed anomalous values of the braking index and the glitch phenomenon. We will also briefly describe the possibility of pairing in the presence of hyperons and deconfined quarks.

In fermionic systems, superfluidity and superconductivity occur due to the pairing of neutral and charged fermions, respectively. The *Cooper Theorem* [1]

states that, in a system of degenerate fermions the Fermi surface is unstable due to the formation of “pairs” if there is an attractive interaction in some spin-angular momentum channel between the two interacting particles. The essence of the BCS theory [2] is that as a result of this instability there is a collective reorganization of particles at energies around the Fermi energy and the appearance of a gap in the quasi-particle spectrum. This reorganization manifests itself in the formation of “Cooper pairs”. At high-enough temperature, the energy gap disappears and the system reverts to its normal state.

To begin, in Sec. 2, we motivate the existence of pairing in neutron stars by examining the pairing phenomenon in laboratory nuclei. We then summarize the relevant properties of neutron stars, including their interior compositions and properties of their crusts in Sec. 3. We describe in Sec. 4 how pairing in dense matter is achieved and, in Sec. 5, we present a brief description of expectations of pairing in deconfined quark matter that may be present in the inner core of the most massive neutron stars. Initially, neutron stars cool primarily due to neutrino emission in their interiors before surface photon cooling takes over later in their lives. In Sec. 6, we summarize the various neutrino processes that can occur in dense matter. Theoretically, these processes can proceed either very rapidly (enhanced neutrino emission) or relatively slowly. We also describe an important secondary process that greatly influences the interpretation of observations – neutrino pair emission from the pair breaking and formation (PBF) of Cooper pairs. This process is triggered as the ambient temperature, decreasing because of cooling, approaches the critical temperatures for superfluidity and superconductivity. The discussion in this section shows how the existence of superfluidity or superconductivity dramatically influences neutrino emissions, leading to both the quenching of enhanced neutrino emission and bursts of neutrino emission due to the PBF processes.

We present in Sec. 7 simplified analytical models of neutron star cooling in order to gain physical insight. These analytical models are complemented by detailed numerical simulations which include general relativity and state-of-the-art microphysics, such as the dense matter equation of state, thermal conductivities, neutrino emissivities, and specific heats. We also summarize in this section the abundant observational data, consisting of estimates of surface temperatures and ages, which collectively describe the thermal evolution of neutron stars. We will show in Sec. 8 that the bulk of this data supports the so-called “Minimal Cooling Paradigm”, which supposes that no drastically enhanced neutrino emission processes occur, or if they do, they are quickly quenched by superfluidity or superconductivity. Nevertheless, a few sources suggesting enhanced cooling are observed, and we discuss the implications.

In Sec. 9, we describe an outstanding recent development in which the first real-time cooling of any isolated neutron star – the young neutron star in the supernova remnant of Cassiopeia A – is observed. The observed rate of cooling is more than 10 times faster than expected, unless both neutron superfluidity and proton superconductivity are present in the star’s core. These observations provide the first direct evidence for superfluidity or superconductivity in the interior of a neutron star, and can be verified by continued observations of the

neutron star in Cassiopeia A.

Section 10 is devoted to other observations of neutron stars and their dynamical evolution that may also indicate the presence of superfluidity. One concerns the deceleration observed in the spin-down of pulsars, which could be due to superfluidity in their cores, while the other is related to sporadic spin jumps, commonly known as glitches, thought to stem from superfluidity in neutron star crusts.

Summarizing discussions and conclusions are contained in Sec. 11.

## 2 Pairing in Nuclei

Soon after the development of the BCS theory, Bohr, Mottelson & Pines [3] pointed out that excitation energies of nuclei exhibit a gap, as shown in the left panel of Fig. 1. A nucleon in even-even nuclei, whether neutron or proton, clearly requires a minimum energy for excitation. This energy was interpreted as being the binding energy of a Cooper pair which must break to produce an excitation. In contrast, odd-even nuclei do not show such a gap, and this is due to the fact that they have one unpaired nucleon which can be easily excited. The right panel of Fig. 1 shows that pairing also manifests itself in the binding energies of nuclei, even-even nuclei being slightly more bound than odd-even or odd-odd nuclei<sup>1</sup>.

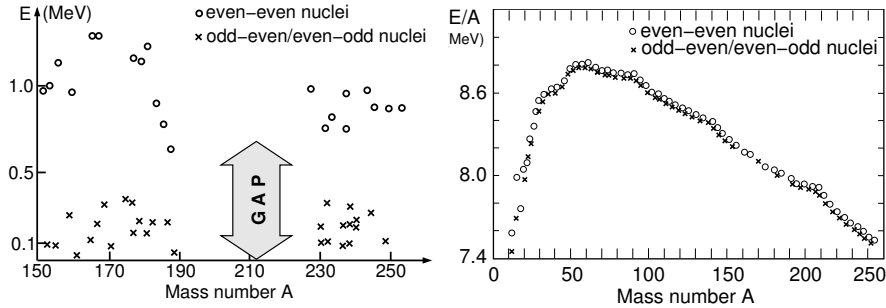


Figure 1: Left panel: Lowest excitation levels of nuclei (adapted from [3]). Right panel: Binding energy per nucleon for the most beta-stable isobars (adapted from [4]).

The systematics of neutron pairing energies in nuclei, defined through

$$\Delta_{Z,N} = \pm \frac{1}{2} (E_{Z,N+1} - 2E_{Z,N} + E_{Z,N-1}), \quad (1)$$

<sup>1</sup>Notice that, as a result of pairing, the only stable odd-odd nuclei are  ${}^2\text{H}(Z=1, N=1)$ ,  ${}^6\text{Li}(3,3)$ ,  ${}^{10}\text{B}(5,5)$ , and  ${}^{14}\text{N}(7,7)$ . All heavier odd-odd nuclei are beta-unstable and decay into an even-even nuclei.

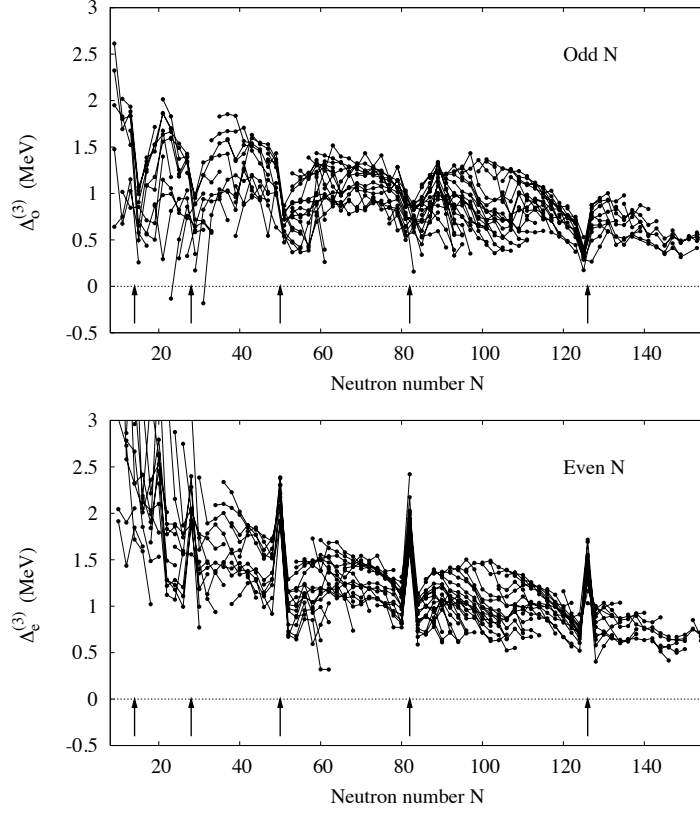


Figure 2: Upper panel: Odd-N pairing energies. Lower panel: Even-N pairing energies. Figure adapted from [5].

where  $E_{Z,N}$  is the binding energy for charge  $Z$  and neutron number  $N$ , and  $+$ ( $-$ ) refers to odd- $N$  and even- $N$  nuclei, are shown in Fig. 2. A few key facts to note are:

1. Pairing energies range from about 3 to 0.5 MeV, decreasing in magnitude with increasing neutron numbers; their behavior with the mass number  $A = N + Z$  is well fit by [5]

$$\Delta_{N,Z} = 24/A + 0.82 \pm 0.27, \quad \text{for } N \text{ odd}, \quad (2)$$

$$\Delta_{N,Z} = 41/A + 0.94 \pm 0.31, \quad \text{for } N \text{ even}. \quad (3)$$

2. Dips (peaks) occur adjacent to (at) the sequence of magic numbers  $N = 14, 28, 50, 82$  and  $126$  for  $N$  odd (even).

Systematics of proton pairing energies for odd- and even- $Z$  as a function of proton number  $Z$  (see Fig. 2 and Table 1 of [5]) show similar qualitative be-

havior, but the magic number effects are less pronounced. If the pairing energy were to be extrapolated to infinite matter using Eq. (2) and  $A \rightarrow \infty$ , the gap should vanish. As gaps in infinite matter are predicted to be finite, a saturation phenomenon is at play. Extended matter in  $^3\text{He}$ , albeit for different reasons, also exhibits finite gaps.

In addition to the excitation spectra and binding energies of nuclei, the pairing phenomenon plays important roles in the dynamical properties of nuclei such as their rotational inertia and the large amplitude collective motion encountered in fissioning nuclei. Tunnelling effects in spontaneously fissioning nuclei receive an enhancement factor  $2\Delta^2/G^2$ , amounting to an order of magnitude or more ( $G$  is a typical pairing interaction matrix element between neighboring mean-field configurations).

Pairing effects are also evident in nuclear reactions. For example, thermal neutrons of energy only  $\sim 0.025$  eV are needed to cause the fission of  $^{235}_{92}\text{U}$  (which results in the even-even compound nucleus  $^{236}_{92}\text{U}$ ), whereas fast neutrons of higher energy  $\sim 1$  MeV are needed to induce fission of  $^{238}_{92}\text{U}$  (the compound nucleus in this case is the even-odd nucleus  $^{239}_{92}\text{U}$ ). What is interesting is that this phenomenon was appreciated well before the BCS theory was formulated, and it lies at the root of building nuclear reactors and purifying naturally-occurring uranium to contain more of the 235 isotope than the 238 isotope.

Besides BCS pairing, the pairing energies shown in Fig. 2 receive contributions from other sources since nuclear sizes are much smaller than the coherence length of the pairing field. The odd-even staggering is caused by a combination of effects including the pair-wise filling of the orbitals, diagonal matrix elements of the two-body interaction, three-nucleon interactions, the bunching of single particle levels near the Fermi energy, and the softness of nuclei with respect to quadrupolar deformations. The global description of the pairing phenomenon in nuclei is based on the Hartree-Fock-Bogoliubov approximation and recent accounts may be found in Refs. [5, 6, 7]. The basic cause for pairing in nuclei is, however, easy to identify. The nuclear interaction between identical nucleons is strongly attractive in the spin  $S = 0$  channel, the di-neutron being nearly bound. The even stronger attraction between neutrons and protons in the spin  $S = 1$  channel produces bound deuterons, but its effects are mitigated in heavy nuclei due to the imbalance of neutrons and protons and attendant many-body effects. In any case, with proton and neutron pairing energies on the order of an MeV, nuclei represent the highest temperature superconductors and superfluid objects in the laboratory. It is interesting that gaps of similar order-of-magnitude are expected for nucleon pairing in neutron stars.

### 3 Neutron Stars

Given that nucleon pairing is important in nuclei, we should expect that pairing will also occur within neutron stars, as was originally pointed out by Migdal in 1959 [8]. Although matter within neutron stars may be heated to more than  $10^{11}$  K during birth, and may remain warmer than  $10^8$  K for hundreds of thou-

sands of years, the nucleons are generally extremely degenerate. Furthermore, given the high ambient densities, the critical temperatures for pairing to occur are large,  $\sim 10^8 - 10^{10}$  K. The onset of pairing is expected to take place in some parts of a neutron star's interior within minutes to thousands of years after birth, and is expected to lead to alteration of several important properties of matter. While pairing will not affect the pressure-density relation significantly<sup>2</sup> and, therefore, the overall structure of neutron stars, the specific heat of dense matter and the emissivity of neutrinos are dramatically influenced. Both emissivities and specific heats are altered at and below the critical temperature, and when the temperature falls well below the pairing critical temperature, both vanish exponentially. This has important consequences for the thermal evolution of neutron stars that will be described in several subsequent sections of this chapter.

Superfluidity can also be important in the dynamical evolution of neutron stars. It has long been suspected that the so-called “glitch” phenomenon observed in pulsars is due to the existence of superfluids within neutron star crusts and perhaps their outer cores. Superfluidity within neutron stars might also significantly contribute to the anomalous braking indices, which are related to the observed long-term deceleration of the spin-down of pulsars. These phenomena will be discussed in Sec. 10.

Neutron stars contain the densest form of cold matter observable in the Universe, in excess of several times the central densities of nuclei (which is often referred to as the nuclear saturation density  $\rho_{\text{nuc}} \simeq 2.7 \times 10^{14} \text{ g cm}^{-3}$ ). Note that  $\rho_{\text{nuc}}$  corresponds to the density where cold matter with a proton fraction  $x_p = 1/2$  has zero pressure. While larger mass-energy densities are transiently reached in relativistic heavy ion collisions, the resulting matter is extremely “hot”. Black holes contain a much denser form of matter, but their interiors are not observable. It has long been believed that neutron stars can only form in the aftermath of the gravitational collapse of a massive star [9], commonly known as gravitational-collapse supernovae to distinguish them from thermonuclear explosions of white dwarfs leading to Type Ia supernovae. However, even the collapse of stars with masses greater than about  $25M_\odot$  are thought to produce briefly existing proto-neutron stars before they collapse further into black holes [10]. Nevertheless, the vast majority of gravitational-collapse supernovae, due to the preponderance of lower-mass stars, will produce stable neutron stars.

Two simple arguments can convince us that neutron stars, very small and very dense, can exist. First, consider the fastest known radio pulsar, Terzan 5 ad (AKA PSR J1748-2446ad) [11], and posit that the observed period of its pulses,  $P = 1.39$  ms, is its rotational period. (Pulses produced by binaries or oscillations of neutron stars are ruled out because nearly all pulsars are observed to be slowing down, while orbital and vibrational frequencies increase as energy is lost.) Using *causality*, that is, imposing that the rotation velocity at its

---

<sup>2</sup>At asymptotically-high densities where deconfined quark matter is thought to exist, pairing gaps could be of order 100 MeV, in which case the EOS is moderately affected by the pairing phenomenon.

equator is smaller than the speed of light  $c$ , one obtains

$$v_{\text{eq}} = \Omega R = \frac{2\pi R}{P} < c \quad \Rightarrow \quad R < \frac{cP}{2\pi} = 65 \text{ km} . \quad (4)$$

This value of 65 km for the radius  $R$  is but a strict upper limit; detailed theoretical models and observations indicate radii on the order of 12 km. Secondly, assuming that the star is *bound by gravity*, we can require that the gravitational acceleration  $g_{\text{eq}}$  at the equator is larger than the centrifugal acceleration  $a_{\text{eq}}$  and obtain

$$\begin{aligned} g_{\text{eq}} = \frac{GM}{R^2} > a_{\text{eq}} = \Omega^2 R = \frac{4\pi^2 R}{P^2} \quad \text{or} \quad \frac{M}{R^3} > \frac{4\pi^2}{GP^2} \\ \Rightarrow \quad \bar{\rho} = \frac{M}{\frac{4}{3}\pi R^3} > 8 \times 10^{13} \text{ g cm}^{-3} . \end{aligned} \quad (5)$$

Obviously, Newtonian gravity is not accurate in this case, but we can nevertheless conclude that the central density of these stars is comparable to, or likely larger than,  $\rho_{\text{nuc}}$ . Theoretical models show that densities up to  $10\rho_{\text{nuc}}$  [12] are possibly reachable. In short, a neutron star is a gigantic, and compressed, nucleus the size of a city.

### 3.1 The Neutron Star Interior

A “pure neutron star”, as originally conceived by Baade & Zwicky [9] and Oppenheimer & Volkoff [13] cannot really exist. Neutrons in a ball should decay into protons through

$$n \rightarrow p + e^- + \bar{\nu}_e . \quad (6)$$

This decay is possible for free neutrons as  $m_n > m_p + m_e$ , where the masses denote rest masses. However, given the large densities expected within the neutron star interior, the relevant quantities are not the masses, but instead the chemical potentials  $\mu_i$  ( $i$  denoting the species) of the participants. The matter is degenerate as typical Fermi energies are on the order of 10 – 100 MeV, whereas the temperature drops below a few MeV within seconds after the birth of the neutron star [14]. Starting with a ball of nearly degenerate neutrons, the decay of Eq. (6) will generate a degenerate sea of protons, electrons and anti-neutrinos. The interaction mean free paths of anti-neutrinos (and neutrinos) far exceed the size of the star. In a neutron star, these can be assumed to immediately vacate the star, implying that  $\mu_\nu = 0$ . Thus, this reaction will ultimately result in the  $\beta$ -equilibrium condition

$$\mu_n = \mu_p + \mu_e , \quad (7)$$

which is equivalent to the energy minimization condition  $\partial\varepsilon/\partial x_p = 0$ , where  $\varepsilon$  is the energy density and the proton fraction is  $x_p$ . At finite, but small temperatures, the inverse reaction

$$p + e^- \rightarrow n + \nu_e \quad (8)$$

also occurs since not all particles are in their lowest energy states at all times.

A neutron star, however, is not born from the collapse of a “ball of neutrons”, but rather from the collapse of the iron core of a massive star. At densities typical of pre-collapse configurations,  $\rho \sim 10^6 \text{ g cm}^{-3}$ ,  $x_p \gtrsim 0.4$ . During collapse, the reaction Eq. (8) therefore initially dominates over Eq. (6) in order to reduce the proton fraction. As the density increases, however, the neutrino mean free paths become smaller than the collapsing core’s size, so  $\nu_e$  temporarily become trapped within the core. In this case,  $\mu_{\nu_e} > 0$ , altering  $\beta$ -equilibrium and permits  $x_p$  to remain relatively large. Only after neutrinos are able to diffuse away, a time of approximately 10 seconds [14], will the final  $\beta$ -equilibrium condition Eq. (7) be achieved.

Eq. (7) allows one to determine the composition of cold dense nucleonic matter. Near  $\rho_{\text{nuc}}$ , a rough approximation to the difference of nucleon chemical potentials is

$$\mu_n - \mu_p \simeq 4S_v \sqrt{\rho/\rho_{\text{nuc}}} (1 - 2x_p), \quad (9)$$

where  $S_v \simeq 31 \text{ MeV}$  is the bulk nuclear symmetry energy parameter. In dense neutron star matter, electrons are relativistic and degenerate, so charge neutrality implies equality between electron and proton number densities and

$$\mu_e = \hbar c (3\pi^2 n_B x_p)^{1/3}, \quad (10)$$

where  $n_B = n_n + n_p = \rho/m_B$  is the baryon density and  $m_B$  is the baryon mass. Therefore, Eq. (7) implies

$$x_p = \left( \frac{4S_v}{\hbar c} \right)^3 \frac{m_B}{3\pi^2 \rho_{\text{nuc}}} \left( \frac{\rho}{\rho_{\text{nuc}}} \right)^{1/2} (1 - 2x_p)^3. \quad (11)$$

This is a cubic equation for  $x_p(\rho)$ , and at the density  $\rho_{\text{nuc}}$  the solution is  $x_{p,\text{nuc}} \simeq 0.034$ . Neutron stars are therefore composed predominantly, but not completely, of neutrons. Eq. (11) predicts that  $x_p$  increases roughly with  $\sqrt{\rho}$  near  $\rho_{\text{nuc}}$ .

Notice that once  $\mu_e > m_\mu \simeq 105 \text{ MeV}$ , muons will appear and be stably present with the conditions of beta equilibrium

$$\mu_\mu = \mu_e \quad (12)$$

and charge neutrality

$$n_p = n_\mu + n_e. \quad (13)$$

The condition for the appearance of muons is fulfilled when the density is slightly above  $\rho_{\text{nuc}}$ . However, even though  $n_p$  and  $n_e$  are no longer equal, the trend that  $x_p$  slowly increases with density is not altered by the presence of muons. Furthermore, in all processes we describe below, there will always be the possibility to replace electrons by muons when the density is large enough for them to appear.

At all but the highest densities, nucleons can be regarded as non-relativistic in neutron star matter, but muons can be either relativistic or non-relativistic



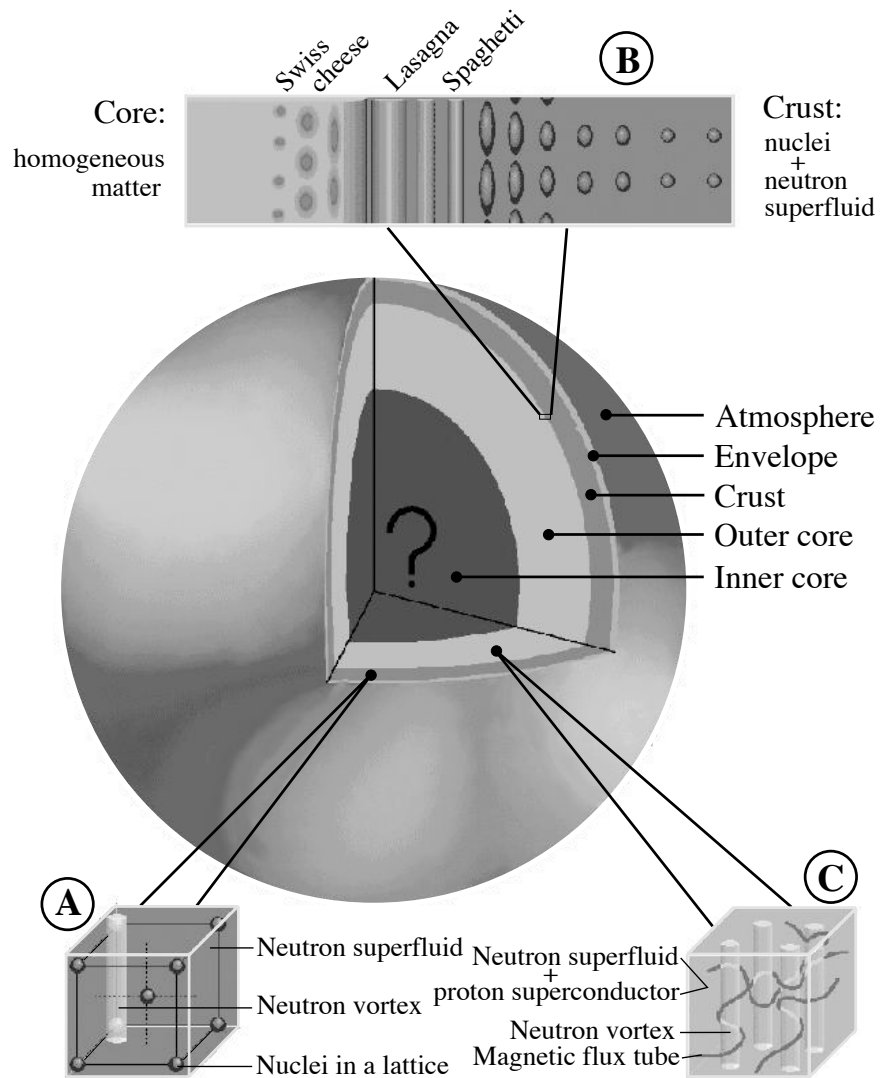


Figure 3: Schematic illustration of the structure of a neutron star; figure taken from [15]. The outermost layers of a neutron star, the atmosphere, envelope, and crust are described in Sec. 3.2. Superfluidity in the crust is schematically represented in inset “A”, and a diagram of the pasta phases in the crust is shown in inset “B”. The core is separated into the outer core, which has the structure given in inset “C”, and the inner core whose nature is currently unknown.

depending on their abundance. For nucleons, the generalization of the simple approximation Eq. (9) is <sup>3</sup>:

$$\mu_n = m_n + \frac{p_{Fn}^2}{2m_n} + V_n, \quad \mu_p = m_p + \frac{p_{Fp}^2}{2m_p} + V_p. \quad (14)$$

For muons,

$$\mu_\mu = \sqrt{m_\mu^2 c^4 + p_{F\mu}^2 c^2}, \quad (15)$$

where  $p_{Fi} = \hbar k_{Fi}$  is the Fermi momentum of species  $i$ , and  $V_n$  and  $V_p$  are the mean-field energies of  $n$  and  $p$ . The Fermi momenta are related to the particle densities by  $k_{Fi}^3 = 3\pi^2 n_i$ . For the leptons,  $V_e$  and  $V_\mu$  are negligibly small. With a knowledge of  $V_n$  and  $V_p$ , the two  $\beta$ -equilibrium relations Eqs. (7) and (12) can be solved. With four chemical potentials and two equations, a unique solution is obtained by imposing charge neutrality, Eq. (12), and fixing  $n_B$ . With the particle densities and chemical potentials known, one can calculate any thermodynamic potential, in particular the pressure  $P$  and energy density  $\epsilon = \rho c^2$ . Varying the value of  $n_B$  gives us the *equation of state* (EOS):  $P(\rho)$ . Given an EOS, an integration of the Tolman-Oppenheimer-Volkoff (TOV, [13]) equations of hydrostatic equilibrium provides us with a well defined model of a neutron star.

The potentials  $V_n$  and  $V_p$  in Eq. (14) turn out to be rapidly growing functions of density, and one can anticipate that eventually reactions such as

$$p + e^- \rightarrow \Lambda + \bar{\nu}_e \quad \text{and/or} \quad n + e^- \rightarrow \Sigma^- + \bar{\nu}_e \quad (16)$$

may produce hyperons. Hyperons can appear once the corresponding  $\beta$ -equilibrium conditions are satisfied, i.e.,  $\mu_n = \mu_\Lambda$  or/and  $\mu_n + \mu_e = \mu_{\Sigma^-}$ . At the threshold, where  $p_{F\Lambda} = 0$  or  $p_{F\Sigma^-} = 0$ , one can expect that  $|V_\Lambda| \ll m_\Lambda$  and  $|V_{\Sigma^-}| \ll m_{\Sigma^-}$  and thus  $\mu_\Lambda \simeq m_\Lambda$  and  $\mu_{\Sigma^-} \simeq m_{\Sigma^-}$ . Since  $m_\Lambda$  and  $m_{\Sigma^-}$  are larger than the nucleon mass by only about 200 MeV these hyperons<sup>4</sup> are good candidates for an “exotic” form of matter in neutron stars. Along similar lines, the lightest mesons, pions and/or kaons, may also appear stably, and can form meson condensates. At even larger densities, the ground state of matter is likely to be one of deconfined quarks. All these possibilities depend crucially on the strong interactions terms,  $V_n$  and  $V_p$ . Figure 3 illustrates our present understanding (or misunderstanding) of the interior of a neutron star, with a black question mark “?” in its densest part. The outer part of the star, its *crust*, is described briefly in the following subsection.

When only nucleons, plus leptons as implied by charge neutrality and constrained by  $\beta$ -equilibrium, are considered, the EOS can be calculated with much more confidence than in the presence of “exotic” forms of matter. For illustrative puposes, we will generally employ the EOS of Akmal, Pandharipande & Ravenhall [16] (“APR” hereafter) in presenting our results.

<sup>3</sup> Relativistic expressions for  $\mu_n$  and  $\mu_p$  also exist, but are omitted here in the interest of simplicity.

<sup>4</sup>The  $\Sigma^+$  is less favored as its  $\beta$ -equilibrium condition is  $\mu_{\Sigma^+} = \mu_p = \mu_n - \mu_e$ . Heavier baryon are even less favored, but cannot *a priori* be excluded.

Although there is no evidence that any observed neutron star or pulsar might actually instead be a pure quark star, theory allows this possibility. Such a star would be nearly completely composed of a mixture of up, down and strange quarks, and would differ from a neutron star in that it would be self-bound rather than held together by gravity.

The reader can find a more detailed presentation and entries to the key literature in [15].

### 3.2 The Neutron Star Envelope and Crust

In the outer part of the star, where  $\rho \lesssim \rho_{\text{nuc}}/2$ , a homogeneous liquid of nucleons is mechanically unstable (known as the spinodal instability). Stability is, however, restored by the formation of nuclei, or nuclear clusters. This region, called the *crust*, has a thickness of  $\lesssim 1$  km.

Above the surface, where the pressure approximately vanishes, we might expect the presence of an *atmosphere*, but there is the possibility of having a solid surface, condensed by a sufficiently-strong magnetic field [17]. A few meters below the surface, ions are completely pressure-ionized (the radius of the first Bohr orbital is larger than the inter-nuclear distance when  $\rho \gtrsim 10^4$  g cm $^{-3}$ ). Matter then consists of a gas/liquid of nuclei immersed in a quantum liquid of electrons. When  $\rho \approx 10^6$  g cm $^{-3}$ ,  $\mu_e$  is of the order of 1 MeV and the electrons become relativistic. Here, and at higher densities, Coulomb corrections are negligible – electrons form an almost perfect Fermi gas. However, Coulomb corrections to the ions are *not* negligible. From a gaseous state at the surface, ions will progressively go through a liquid state (sometimes called the *ocean*) and finally crystallize, at densities between  $10^2$  up to  $\sim 10^{10}$  g cm $^{-3}$  depending on the temperature (within the range of temperatures for which neutron stars are thermally detectable). These low-density layers are commonly referred to as the *envelope*.

With growing  $\rho$ , and the accompanying growth of  $\mu_e$ , it is energetically favorable to absorb electrons into neutrons and, hence, nuclei become progressively neutron-rich. When  $\rho \sim 4 \times 10^{11}$  g cm $^{-3}$  (the exact value depends on the assumed chemical composition), one achieves the *neutron drip* point at which the neutron density is so much larger than that of the protons that some neutrons become unbound (i.e.,  $\mu_n > 0$ ). Matter then consists of a crystal of nuclei immersed in a Fermi gas of electrons and a quantum liquid of dripped neutrons. The region containing dripped neutrons is usually called the *inner crust*. In most of this inner crust, because of the long-range attractive nature of the nucleon-nucleon interaction, the dripped neutrons are predicted to form a superfluid (in a spin-singlet, zero orbital angular momentum, state  $^1S_0$ ). All neutron stars we observe as pulsars are rotating. While a superfluid cannot undergo rigid body rotation, it can simulate it by forming an array of vortices (in the cores of which superfluidity is destroyed). (See, e.g., [18].) The resulting structure is illustrated in inset A of Fig. 3.

At not too-high densities, nucleons are correlated at short distances by strong interaction and anti-correlated at larger distances by Coulomb repulsion be-

tween the nuclei, the former producing spherical nuclei and the latter resulting in the crystallization of the matter. As  $\rho$  approaches  $\sim 0.03\rho_{\text{nuc}}$ , the shapes of nuclei can undergo drastic changes: the nuclear attraction and Coulomb repulsion length-scales become comparable and the system is “frustrated”. From spherical shapes, as the density is increased, nuclei are expected to deform, become elongated into 2D structures (“spaghetti”), and then form 1D structures (“lasagna”), always with denser nuclear matter surrounded by the dilute neutron gas/superfluid which occupies an increasing portion of the volume. When the phases achieve approximately equal volume fractions, the geometry can invert, with dripped neutrons confined into 2D (“anti-spaghetti” or “ziti”) and finally 3D (“swiss cheese”) bubbles. The homogeneous phase, i.e. the *core* of the star, is reached when  $\rho \simeq 0.5 - 0.6\rho_{\text{nuc}}$ . This “pasta” regime is illustrated in inset B of Fig. 3 and is thought to resemble a liquid crystal [19]. A compilation of the most recent progress on neutron star crust physics can be found in the book [20].

## 4 Pairing in the Neutron Star Interior

### 4.1 General Considerations

#### Expectations from measured phase shifts

As a two-particle bound state, the Cooper pair can appear in many spin-orbital angular momentum states (see the left panel of Fig. 4). In terrestrial superconducting metals, the Cooper pairs are generally in the  $^1\text{S}_0$  channel, i.e., spin-singlets with  $L = 0$  orbital angular momentum, whereas in liquid  $^3\text{He}$  they are in spin-triplet states. What can we expect in a neutron star? In the right panel of Fig. 4, we adapt a figure from one of the first works to study neutron pairing in the neutron star core [21] showing laboratory-measured phase-shifts from nucleon-nucleon scattering. A positive phase-shift implies an attractive interaction. From this figure, one can expect that nucleons could pair in a spin-singlet state,  $^1\text{S}_0$ , at low densities, whereas a spin-triplet,  $^3\text{P}_2$ , pairing should occur at high densities. We emphasise that this is only a *presumption* (phase shifts reflect free-space interaction) as medium effects can strongly affect particle interactions.

#### The energy gap

In a normal Fermi system at  $T = 0$ , all particles are in states with energies  $\epsilon \leq \epsilon_F$ . When  $T > 0$ , states with energies  $\epsilon \gtrsim \epsilon_F$  can be occupied (left panel of Fig. 5) resulting in a smearing of the particle distribution around  $\epsilon_F$  in a range  $\sim k_B T$ . It is precisely this smooth smearing of energies around  $\epsilon_F$  which produces the linear  $T$  dependence of  $c_v$ , Sec. 7.1, and the  $T^6$  or  $T^8$  dependence of the neutrino emissivities, Sec. 6.5.

In a superfluid/superconducting Fermi system at  $T = 0$ , all particles are in states with energies  $\epsilon \leq \epsilon_F$  (actually,  $\epsilon \leq \epsilon_F - \Delta$ ). For nonzero temperatures

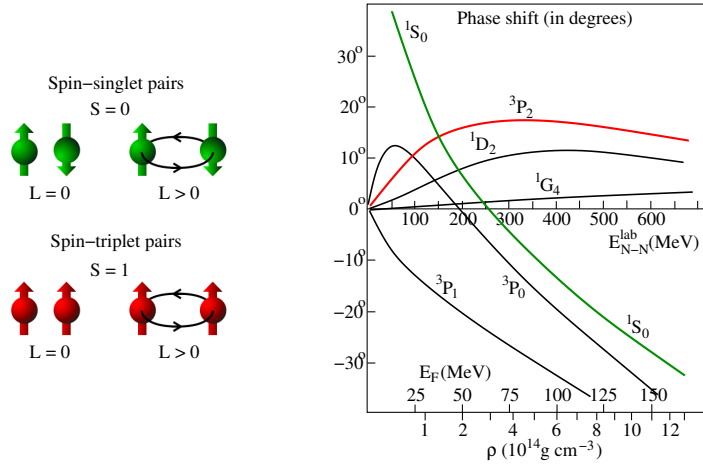


Figure 4: Left panel: Possible spin-angular momentum combinations for Cooper-pairs. Right panel: Phase shifts for N-N scattering as a function of the laboratory energy (middle axis) or the neutron Fermi energy and density for a neutron star interior (lower axis). Adapted from [21].

that permit the presence of Cooper pairs (and hence a gap  $\Delta(T)$ ), states with energy  $\epsilon \geq \epsilon_F + \Delta$  can be populated. However, in contrast to the smooth filling of levels above  $\epsilon_F$  in the case of a normal Fermi liquid, the presence of the  $2\Delta(T)$  gap in the spectrum implies that the occupation probability is strongly suppressed by a Boltzmann-like factor  $\sim \exp[-2\Delta(T)/k_B T]$ . As a result, both the specific heat of paired particles and the neutrino emissivity of all processes in which they participate are strongly reduced.

### The phase transition

The transition to the superfluid/superconducting state through pairing *à la* BCS is usually a second order phase transition and the gap  $\Delta(T)$  is its order parameter (see central panel of Fig. 6). Explicitly,  $\Delta(T) = 0$  when  $T > T_c$ , the critical temperature, and, when  $T$  drops below  $T_c$ ,  $\Delta(T)$  grows rapidly but continuously, with a discontinuity in its slope at  $T = T_c$ . There is no latent heat but a discontinuity in specific heat. (Examples: superfluid  $\leftrightarrow$  normal fluid; ferromagnetic  $\leftrightarrow$  paramagnetic.) In the BCS theory, which remains approximately valid for nucleons, the relationship between the zero temperature gap and  $T_c$  is

$$\Delta(T = 0) \simeq 1.75 k_B T_c. \quad (17)$$

In a first order phase transition there is a discontinuous change of  $\Delta(T)$  at  $T_c$  and the transition occurs entirely at  $T_c$  (see left panel of Fig. 6). There is a latent heat due to the entropy difference between the two states. (Examples: solid  $\leftrightarrow$  liquid; liquid  $\leftrightarrow$  gas below the critical point.) In a smooth state transition there

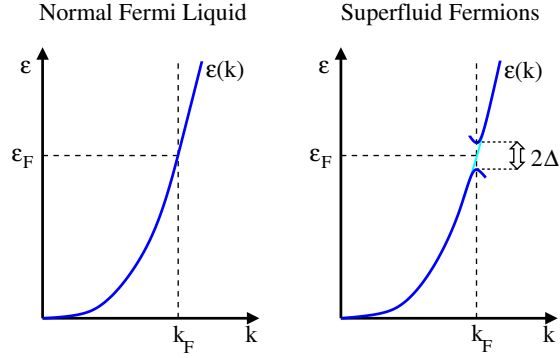


Figure 5: Comparison of quasi-particle spectra,  $\epsilon(k)$ , for a normal and a superfluid Fermi liquid. The reorganization of particles at  $\epsilon \sim \epsilon_F$  into Cooper pairs results in the development a gap  $2\Delta$  in the spectrum so that no particle can have an energy between  $\epsilon_F - \Delta$  and  $\epsilon_F + \Delta$ .

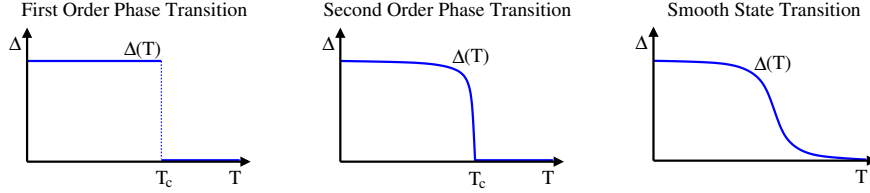


Figure 6: Temperature evolution of the state of a system parametrized by an “order” parameter,  $\Delta(T)$ .

is a continuous change of  $\Delta(T)$  with no critical temperature (see the right panel of Fig. 6). (Examples: liquid  $\leftrightarrow$  gas above the critical point; atomic gas  $\leftrightarrow$  plasma.)

### A simple example

A simple model can illustrate the difficulty in calculating pairing gaps. Consider a dilute Fermi gas with a weak, attractive, interaction potential  $U$ . The interaction is then entirely described by the corresponding scattering length<sup>5</sup>,  $a$ , which is negative for an attractive potential. In this case, the model has a single dimensionless parameter,  $|a|k_F$ , and the dilute gas corresponds to  $|a|k_F \ll 1$ . Assuming the pairing interaction is just the bare interaction  $U$  (which is called the *BCS approximation*), the gap equation at  $T = 0$  can be solved analytically,

<sup>5</sup>The scattering length  $a$  is related to  $U$  by  $a = (m/4\pi\hbar^2)U_0$  with  $U_{\mathbf{k}} = \int d^3r \exp(i\mathbf{k} \cdot \mathbf{r}) U(\mathbf{r})$ .

giving the *weak-coupling BCS-approximation* gap:

$$\Delta(k_F) \xrightarrow{|a|k_F \rightarrow 0} \Delta_{BCS}(k_F) = \frac{8}{e^2} \left( \frac{\hbar^2 k_F^2}{2M} \right) \exp \left[ -\frac{\pi}{2|a|k_F} \right]. \quad (18)$$

This result is bad news: the gap depends exponentially on the pairing potential  $U$ . The Cooper pairs have a size of the order of  $\xi \sim \hbar v_F / \Delta$  (the *coherence length*) and thus  $\xi k_F \propto \exp[+\pi/2|a|k_F] \gg 1$  in the weak coupling limit. There is, hence, an exponentially growing number of other particles within the pair's coherence length when  $|a|k_F \rightarrow 0$ . These particles will react and can screen, or un-screen, the interaction. Including this medium polarization on the pairing is called *beyond BCS*, and in the weak coupling limit its effect can be calculated analytically [22], giving

$$\Delta(k_F) \xrightarrow{|a|k_F \rightarrow 0} \Delta_{GMB}(k_F) = \frac{1}{(4e)^{1/3}} \Delta_{BCS}(k_F) \simeq 0.45 \Delta_{BCS}(k_F) \quad (19)$$

So, screening by the medium can reduce the gap by more than a factor two, even in an extremely dilute system.

## 4.2 Calculations of Pairing Gaps

A significant amount of work has been devoted to the calculation of pairing gaps in the neutron star environment: see, e.g., [23, 24, 25] or A. Schwenk's contribution to this volume for reviews. Below we first briefly describe the Gorkov formalism [26, 27, 23] that will allow us to set up the stage for the presentation of representative results for nucleon gaps. Specifically, we will address the neutron  $^1S_0$  and  $^3P\text{-}F_2$  and the proton  $^1S_0$  and  $^3P\text{-}F_2$  gaps and briefly mention hyperon gaps. The effects of pairing on the thermal evolution of neutron stars are described in Sec. 4.3. Calculations of pairing gaps in quark matter will be described in Sec. 5.

### General formalism

Several significant effects of pairing are due to the change in the quasi-particle spectrum that is obtained from the poles of the propagator  $G$ . In Fig. 7, Eq. (A), we show the definition of  $G$ , the two point Green's function with one particle in and one particle out, and its Dyson equation which relates the free propagator and the self energy  $\Sigma$  in the case of a normal system. The resulting quasi-particle spectrum is then

$$\omega = \epsilon(\mathbf{k}, \omega) = \frac{\hbar^2 \mathbf{k}^2}{2m} + \Sigma(\mathbf{k}, \omega) - \epsilon_F \simeq \frac{\hbar^2 k_F}{m^*} (k - k_F). \quad (20)$$

In obtaining the right-most result above, we assumed the system to be isotropic and the spectrum is evaluated for  $k \simeq k_F$  with the effective mass  $m^*$  defined through

$$\left. \frac{\partial \epsilon(k, \omega = 0)}{\partial k} \right|_{k=k_F} = \frac{\hbar^2 k_F}{m^*}. \quad (21)$$

(A)  $iG(1, 2) = \langle T\{\psi(1)\psi^\dagger(2)\} \rangle = \text{---}\text{---} = \text{---}\text{---} + \text{---}\text{---}\text{---}\text{---}$

Figure 7: The normal state propagator and its Dyson equation.

The resulting spectrum  $\epsilon_F + \omega$  is depicted in the left panel of Fig. 5.

In the presence of a pairing instability, and the concomitant development of a condensate, an *anomalous propagator*  $F$  and its adjoint  $F^\dagger$  can be defined, see Eq. (B) and Eq. (B') in Fig. 8, with their corresponding Gorkov equations that replace the Dyson equation. In addition to the self energy  $\Sigma$ , the Gorkov equations feature an *anomalous self energy*, or the *gap function*  $\Delta$ . The propagator  $F$  violates particle number conservation as it propagates a hole into a particle, and vanishes in the absence of a condensate in a normal system. The gap function is a  $2 \times 2$  matrix in spin space

$$\hat{\Delta}(\mathbf{k}, \omega) = \begin{pmatrix} \Delta_{\uparrow\uparrow}(\mathbf{k}, \omega) & \Delta_{\uparrow\downarrow}(\mathbf{k}, \omega) \\ \Delta_{\downarrow\uparrow}(\mathbf{k}, \omega) & \Delta_{\downarrow\downarrow}(\mathbf{k}, \omega) \end{pmatrix}. \quad (22)$$

In the case the ground state is assumed to be time-reversal invariant,  $\hat{\Delta}(\mathbf{k}, \omega)$  (denoted  $\hat{\Delta}$  for short below) has a unitary structure satisfying

$$\hat{\Delta}\hat{\Delta}^\dagger = \hat{\Delta}^\dagger\hat{\Delta} = \Delta^2 \hat{1} \quad (23)$$

where  $\hat{1}$  is a  $2 \times 2$  unit matrix, and

$$\Delta^2 = \Delta^2(\mathbf{k}, \omega) = \det \hat{\Delta}(\mathbf{k}, \omega). \quad (24)$$

The quantity  $\Delta$  above will appear as the *energy gap* in the quasi-particle spectrum.

The normal propagator  $G$  is also modified, as depicted in Eq. (C) in Fig. 8. Solving the Gorkov equations gives  $G = (\omega + \epsilon)/D$  with

$$D(\mathbf{k}, \omega) = \omega^2 - \epsilon(\mathbf{k}, \omega)^2 - \Delta(\mathbf{k}, \omega)^2 \quad (25)$$

and its modified poles yield a quasi-particle spectrum with two branches:

$$\omega = \pm \sqrt{\epsilon(\mathbf{k}, \omega)^2 + \Delta(\mathbf{k}, \omega)^2}. \quad (26)$$

The resulting spectrum  $\epsilon_F + \omega$  is depicted in the right panel of Fig. 5. Note that,  $G$  and  $\Sigma$  are also  $2 \times 2$  matrices in spin space both being diagonal in structure. The solution of the Gorkov equation for  $F$  gives  $F = \hat{\Delta}^\dagger/D$ . Finally,  $\Sigma$  and  $\Delta$  are defined by Eq. (D) and (E) in Fig. 8 from a kernel  $K$ . Equation (D) is the gap equation and reads

$$\Delta_{\alpha\beta}(k) = i \int \frac{d^4 k'}{(2\pi)^4} \sum_{\alpha', \beta'} \frac{\langle k\alpha, -k\beta | K | k'\alpha', -k'\beta' \rangle \Delta_{\alpha'\beta'}(k')}{D(k')}, \quad (27)$$

where  $k = (\mathbf{k}, \omega)$ ,  $k' = (\mathbf{k}', \omega')$  and  $\alpha, \beta, \dots$  denote spin indices.



$$\begin{aligned}
\text{(B)} \quad iF(1, 2) &= \langle T\{\psi(1)\psi(2)\} \rangle = \longleftrightarrow = \text{---} \textcircled{\Sigma} \text{---} + \text{---} \textcircled{\Delta^*} \text{---} \\
\text{(B')} \quad iF^\dagger(1, 2) &= \langle T\{\psi^\dagger(1)\psi^\dagger(2)\} \rangle = \longleftrightarrow = \text{---} \textcircled{\Sigma} \text{---} + \text{---} \textcircled{\Delta} \text{---} \\
\text{(C)} \quad iG(1, 2) &= \langle T\{\psi(1)\psi^\dagger(2)\} \rangle = \longleftrightarrow = \text{---} + \text{---} \textcircled{\Sigma} \text{---} + \text{---} \textcircled{\Delta} \text{---} \\
\text{(D)} \quad \text{---} \textcircled{\Sigma} \text{---} &= \text{---} \textcircled{K} \text{---} \\
\text{(E)} \quad \text{---} \textcircled{\Delta} \text{---} &= \text{---} \textcircled{K} \text{---}
\end{aligned}$$

Figure 8: The Gorkov equations

Solving the full set of equations in Fig. 8 requires many approximations, notably in the choice of the kernel  $K$ . In particular, different approximate kernels  $K$  are used in (D) and (E) as it appears in the particle-hole channel in (D), whereas in (E) it is in the particle-particle channel. In the *BCS approximation*, the self energy is calculated in the normal phase (e.g., with a Brückner-Hartree-Fock or BHF scheme) with its energy dependence being neglected, i.e.  $\Sigma(\mathbf{k}, \omega) \rightarrow \Sigma(\mathbf{k})$ , and the kernel for  $\Delta$  is simply taken as the bare interaction. The latter can be a two-body force (2BF) from a potential adjusted to laboratory N-N scattering data or that derived from an effective interaction such as a Skyrme force. Recently, the effect of three-body forces (3BF), absent in the laboratory N-N scattering experiment, has been considered. Inclusion of 3BF is necessary to reproduce the nuclear saturation density; they are, in the bulk, repulsive and their importance grows with increasing density. Even at the 2BF level, a severe problem is encountered: to date, none of the N-N interaction models reproduce the measured phase shifts for  $E_{\text{lab}}$  larger than 300 MeV in the channels needed (particularly for  $^3\text{P}_2$ ) for the conditions prevailing in the core of a neutron star. The source of this problem is easy to identify; beyond 290 MeV (the threshold for pion production), inelastic channels begin to become dominant.

Models *beyond BCS* have proceeded in two directions. In the first approach, in the gap equation, the bare interaction is supplemented by the inclusion of short-range correlations. In a further step, long-range correlations to account for medium polarization are added. As illustrated above with the weak-coupling result of Eq. (19), polarization effects can be significant. In the second approach, which goes beyond the BHF level, the self energy  $\Sigma$  is calculated by including its energy dependence. Calculations of  $\Sigma$  in the paired phase, see Eq. (D) in Fig. 8, do not yet exist and are necessary. In the following, we will neglect the energy dependence of the gap, i.e., write it as  $\hat{\Delta}(\mathbf{k})$  instead of  $\hat{\Delta}(\mathbf{k}, \omega)$ .

### Pairing in single spin-angular momentum channels

In pairing calculations, the potential and the gap function are usually expanded in partial waves so as to focus on specific spin-angular momentum channels,  $\lambda =$

$(s, j)$ . At low  $k_{Fn}$ , or  $k_{Fp}$ , it is theoretically predicted that the preferred channel is  $\lambda = (0, 0)$  in  $S$ -wave, i.e., the spin-singlet  $^1S_0$ . At large Fermi momenta, the  $^1S_0$  interaction becomes repulsive and the preferred channel is  $\lambda = (1, 2)$  in  $P$  and  $F$  waves (the mixing being due to the tensor interaction [28]), i.e., the spin-triplet  $^3P$ - $F_2$ . In the  $^1S_0$  channel, which has also been called the “A” phase, the gap is spherically symmetric and can be written as

$$\text{A phase } (^1S_0): \hat{\Delta}_{(0,0)}(\mathbf{k}) = \begin{pmatrix} 0 & \Delta(k) \\ -\Delta(k) & 0 \end{pmatrix} \quad [\Delta(k_F) = \text{energy gap}] \quad (28)$$

In the  $^3P$ - $F_2$  channel,  $\hat{\Delta}_\lambda$  has contributions from all possible orbital angular momenta  $l$  and their  $m_j$  components, i.e.,  $\hat{\Delta}_\lambda = \sum_{l,m_j} \Delta_{l\lambda}^{m_j}(k) \hat{G}_{l\lambda}^{m_j}(\hat{\mathbf{k}})$ , where the  $\hat{G}_{l\lambda}^{m_j}(\hat{\mathbf{k}})$  are  $2 \times 2$  spin matrices describing the angular dependence of  $\hat{\Delta}_\lambda$  which is thus *not* spherically symmetric. Microscopic calculations restricted to the  $^3P_2$  channel [29, 30] indicate that the largest component of  $\hat{\Delta}_\lambda$  corresponds to the  $m_j = 0$  sub-channel or, possibly, the  $m_j = \pm 2$  channels, sometimes called the “B” and “C” phases, respectively. For these two special cases, the energy gap  $\Delta(\mathbf{k}_F)$  is given by [29]

$$\text{B phase } (^3P_2, m_j = 0): \quad \Delta^2(\mathbf{k}_F) = \frac{1}{2} [\Delta_{2\lambda}^0(k_F)]^2 \frac{1 + 3 \cos^2 \theta_k}{8\pi} \quad (29)$$

$$\text{C phase } (^3P_2, m_j = \pm 2): \quad \Delta^2(\mathbf{k}_F) = [\Delta_{2\lambda}^2(k_F)]^2 \frac{3 \sin^2 \theta_k}{8\pi}, \quad (30)$$

where  $\theta_k$  is the angle between  $\mathbf{k}_F$  and the arbitrary quantization axis. Notice that in the B phase, the gap is nodeless whereas in the C phase it vanishes on the equator,  $\theta_k = \pi/2$ .

### Temperature dependence of $\Delta$ and $T_c$

The preceding discussion was restricted to the zero temperature case. It is naturally extended to finite temperature whence the gap becomes  $\hat{\Delta}(\mathbf{k}; T)$ . However, effects of thermal excitations are important only for values of  $\mathbf{k} \simeq \mathbf{k}_F$ . We will often omit either of the arguments  $\mathbf{k}_F$  or  $T$  when not necessary, but they are always implied (as is its  $\omega$  dependence). Notice that microscopic calculations are often limited to the  $T = 0$  case only.

The relationship between the critical temperature  $T_c$  for the phase transition and the energy gap  $\Delta(\mathbf{k}_F)$  is approximately given by the usual result

$$k_B T_c \approx 0.57 \bar{\Delta}(k_F; T = 0) \quad (31)$$

for all three phases A, B, and C [29, 30], where  $\bar{\Delta}(k_F; T)$  is obtained by angle averaging of  $\Delta^2(\mathbf{k}_F, T)$  over the Fermi surface

$$[\bar{\Delta}(k_F; T)]^2 \equiv \int \int \frac{d\Omega}{4\pi} \Delta^2(\mathbf{k}_F; T). \quad (32)$$

Obviously,  $\bar{\Delta}(k_F; T) = \Delta(k_F; T)$  for an isotropic  $^1S_0$  gap. The temperature dependence of the energy gap  $\Delta(k_F, T)$  for  $^1S_0$  pairing and of the angle averaged  $\bar{\Delta}(k_F; T)$  for the  $^3P_2$  pairing in the  $m_j = 0$  case are shown in Fig. 9.

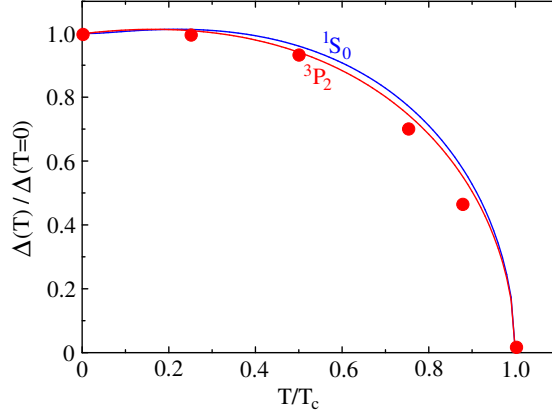


Figure 9: Temperature dependence of the energy gap  $\Delta(k_F, T)$  for  $^1S_0$  pairing and of the angle averaged  $\bar{\Delta}(k_F; T)$  for the  $^3P_2$  pairing in the  $m_j = 0$  case. Continuous lines show the commonly used analytical fits of [31] whereas the dots are from the calculations of [30].  $^3P_2$  pairing in the  $m_j = 2$  case results in values very close to the  $m_j = 0$  case.

### The isotropic $^1S_0$ neutron gap

In Fig. 10, we show sets of predicted  $T_c$  for the neutron  $^1S_0$  pairing in uniform pure neutron matter. The two dotted lines marked “BCS” and “GMB” show the simple analytical results of Eq. (18) and Eq. (19), respectively, with  $a = -18.5$  fm and  $T_c = 0.56 \Delta(k_F)$ . Formally, these results are only valid when  $|a|k_F \ll 1$ , i.e.,  $k_F \ll 0.1$  fm $^{-1}$ . The curve “SCLBL”, from [32], illustrates the results of a numerical solution of the gap equation, using the Argonne  $V_{14}$  N-N potential, within the BCS approximation. The results merge with the “BCS” curve in the weak coupling limit  $k_F \rightarrow 0$ . Also shown are results from calculations that take into account more sophisticated medium effects, including medium polarization (with different schemes): “CCDK”, from [33], employed a variational method within the correlated basis functions scheme, “WAP”, from [34], employed an extension of the induced interaction scheme, whereas “SFB”, from [35], went beyond [34] with renormalization group methods. In line with the simple GMB result of Eq. (19), these model calculations show that polarization has a screening effect that quenches the gap, by a factor  $\sim 3$ . These three calculations yield some agreement, particularly in the predicted maximum value of  $T_c$ , but with a non-negligible difference in the density dependence. The other two curves show more recent results: “GIPSF”, from [36], utilizes the auxiliary-field diffusion Monte Carlo technique while “GC”, from [37], stems from a Quantum Monte Carlo calculation. These last two models result in gaps that are intermediate between the previous models and the BCS approximation; moreover, they converge toward the GMB value when  $k_F \rightarrow 0$ .

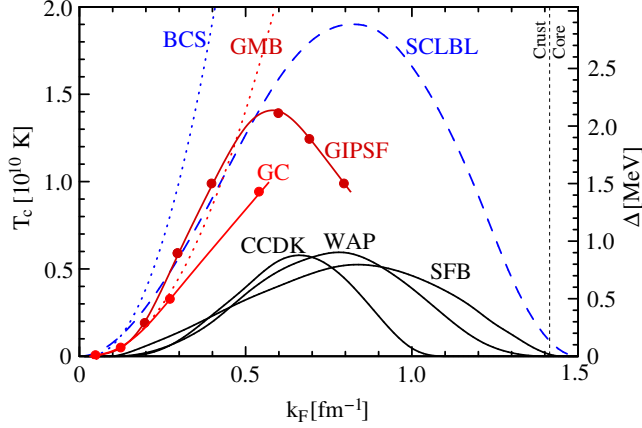


Figure 10: Some theoretical predictions of  $T_c$  and  $\Delta$ , vs neutron  $k_F$ , for the neutron  $^1S_0$  gap in uniform pure neutron matter. The value of  $k_F$  corresponding to the transition from the crust to the core is indicated. See text for description.

Transcribed to the neutron star context, the range of Fermi momenta for which these neutron  $^1S_0$  gaps are non vanishing corresponds mostly to the dripped neutrons in the inner crust. The presence of nuclei, or nuclear clusters in the pasta phase, may modify the sizes of these gaps from their values in uniform matter. The coherence length  $\xi$  of the dripped neutrons is larger than the sizes of nuclei, leading to proximity effects. This issue has received some attention, see, e.g., [38, 39, 40, 41], and position dependent gaps, from inside to outside of nuclei, have been calculated. However, in most of the crust  $\xi$  is smaller than the internuclear distance, and the size of the gap far outside the nuclei is close to its value in uniform matter.

### The isotropic $^1S_0$ proton gap

The magnitudes of proton  $^1S_0$  gaps are similar to those of neutrons, but with the important difference that, in the neutron star context in which beta equilibrium prevails, protons are immersed within the neutron liquid, and constitute only a small fraction of the total baryon number (3 to 20% in the density range where they are expected to be superconducting). Proton-neutron correlations cause the effective mass of the proton to be smaller than that of the neutron, a simple effect that reduces the size of the proton  $^1S_0$  gap compared to that of the neutron.

Several theoretical predictions of  $T_c$  for the proton  $^1S_0$  gap are shown in Fig. 11: “CCY” from [42], “T” from [43], and “AO” from [44] that are among the first historical calculations, whereas “BCLL” from [30], “CCDK” from [33], and “EEHO” from [45] are more recent results. All of these calculations were performed within the BCS approximation and very few works have gone beyond

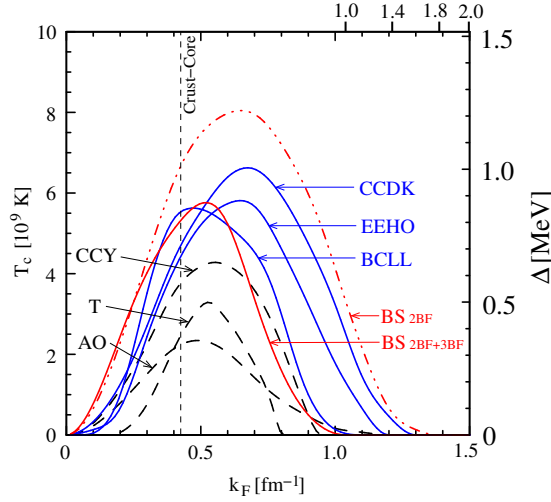


Figure 11: Some theoretical predictions of  $T_c$  and  $\Delta$ , vs proton  $k_F$ , for the proton  $^1S_0$  gap in  $\beta$ -equilibrium uniform neutron-proton matter. The value of  $k_F$  corresponding to the transition from the crust to the core is indicated: values on the right of this line correspond to the neutron star core but values on the left are not realized since protons in the crust are confined within nuclei which are finite size systems while this figure presents results for infinite matter. On the top margin are marked the values of the proton  $k_F$  at the center of a 1.0, 1.4, 1.8, and 2.0  $M_\odot$  star built with the APR EOS [16]. See text for description.

BCS for the proton  $^1S_0$  gap. Among the latter, we show results from [46]: these authors used either only two body forces in the interaction kernel, curve “BS<sub>2BF</sub>”, or two body forces supplemented by the inclusion of three body forces, curve “BS<sub>2BF+3BF</sub>” which shows that three body forces are *repulsive* in the  $^1S_0$  channel. These “BS” results also include effects of medium polarization. Recall that for the  $^1S_0$  pairing of neutrons in pure neutron matter, polarization has a screening effect and quenches the gap. However, in neutron star matter, where the medium consists mostly of neutrons, the strong  $np$ -correlations result in medium polarization inducing *anti-screening* [47] for the  $^1S_0$  pairing of protons.

### The anisotropic $^3P\text{-}F_2$ neutron (and proton) gap

The  $^1S_0$  neutron gap vanishes at densities close to the crust-core transition and the dominant pairing for neutrons in the core occurs in the mixed  $^3P\text{-}F_2$  channel. Uncertainties in the actual size and the range of density in which this gap persists are however considerable. As previously mentioned, a major source of uncertainty is the fact that even the best models of the N-N interaction *in vacuum* fail to reproduce the measured phase shift in the  $^3P_2$  channel [48]. Also significant are the effects of the medium on the kernel and 3BF, even at the

level of the BCS approximation. It was found in [49] that 3BF at the Fermi surface are strongly *attractive* in the  $^3\text{P-F}_2$  channel in spite of being repulsive in the bulk. Moreover, due to medium polarization a long-wavelength tensor force appears that is not present in the interaction *in vacuum* and results in a strong suppression of the gap [50].

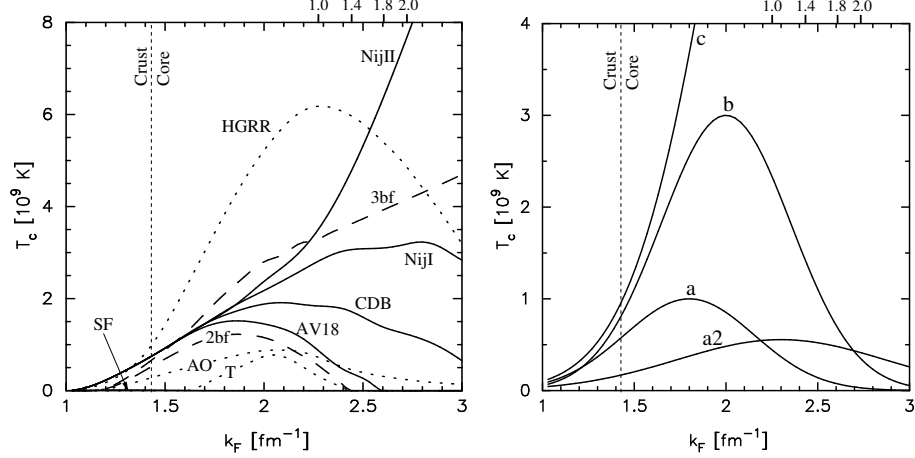


Figure 12: Left panel: some theoretical predictions of  $T_c$  for the neutron  $^3\text{P-F}_2$  gap in uniform pure neutron and  $\beta$ -equilibrium matter. See text for description. Right panel: some phenomenological models of  $T_c$  for the neutron  $^3\text{P-F}_2$  gap used in neutron star cooling simulations. Models “a”, “b”, and “c” are from [51] and [52], model “a2” from [53]. On the top margin are marked the values of  $k_{Fn}$  at the center of a 1.0, 1.4, 1.8, and 2.0  $M_\odot$  star built with the APR EOS [16].

Figure 12 shows examples of theoretical predictions of  $T_c$  for the neutron  $^3\text{P-F}_2$  gap. The three dotted lines show some of the first published models: “HGR” from [54], “T” from [55] and “AO” from [29]. The four continuous lines show results of models from [48] calculated using the Nijmegen II (“NijII”), Nijmegen I (“NijI”), CD-Bonn (“CDB”), and Argonne  $V_{18}$  (“AV18”) potentials (displayed values are taken from the middle panel of Figure 4 of [48]). The results of these four models start to diverge at  $k_{Fn}$  above  $1.8 \text{ fm}^{-1}$  and illustrate the failure of all four N-N interactions models to fit the  $^3\text{P}_2$  laboratory phase-shifts above  $E_{\text{lab}} \simeq 300 \text{ MeV}$ . All of these calculations were performed for pure neutron matter using the BCS approximation.

In the case of the  $^1\text{S}_0$  gap, medium polarization is known to result in screening and to reduce the size of the gap. In the case of a  $^3\text{P}_2$  gap, polarization with central forces is expected to result in anti-screening and to increase the size of the gap. However, Schwenk & Friman [50] showed that spin-dependent non-central forces do the opposite and strongly screen the coupling in the  $^3\text{P}_2$  channel, resulting in a  $T_c$  lower than  $10^7 \text{ K}$ : this “SF” value is indicated in the

Figure by an arrow.

The two dashed lines in Fig. 12 present results from [56] where the “2BF” model only considers 2-body forces (from the Argonne  $V_{18}$ ) while the “3BF” model includes a meson exchange model 3-body force: the result is a growing  ${}^3\text{P-F}_2$  gap which shows no tendency to saturate at high density. This work, for  $\beta$ -equilibrium matter, moreover emphasized the importance of the proton component.

Other delicate issues are the effect of the proton contaminant and the likely development of a  $\pi^0$  condensate<sup>6</sup> which also strongly affects the size of the neutron (and proton) gap(s).

In summary, the size and extent in density of the neutron  ${}^3\text{P-F}_2$  gap in the neutron star core is poorly known. Given these large uncertainties in the size of the neutron  ${}^3\text{P-F}_2$  gap (about three orders of magnitude) and the fact that neutrino emissivity is suppressed by an exponential Boltzmann-like factor, this gap is often considered as a free parameter in neutron star cooling models. The extreme sensitivity of the cooling history on the size of this gap can be utilized to one’s advantage by inverting the problem, as it may allows us to *measure* it by fitting theoretical models to observational data [57]. The right panel of Fig. 12 presents the phenomenological neutron  ${}^3\text{P-F}_2$  gaps used in cooling calculations in a later section.

In the case of protons, their  ${}^3\text{P-F}_2$  gaps have generally been overlooked due to their small effective masses, and considered to be likely negligible [58]. However, in view of the strong enhancing effect of the 3BF on the neutron  ${}^3\text{P-F}_2$  gap, this issue has been reconsidered in [49] where it was shown that the proton  ${}^3\text{P-F}_2$  gap can be sizable.

## Hyperon gaps and nucleon gaps in hyperonic matter

Many calculations of dense matter indicate that strangeness-bearing hyperons will be present in neutron star matter once the neutron chemical potential exceeds the rest masses of hyperons [59] (see Sec. 3.1). In the likely presence of hyperons (denoted by Y) arise the issues of, first, the effect of their presence on the nucleon gaps, and second, the possibility of hyperon pairing. Nucleon gaps in the presence of hyperons have been studied in [49] and [60]: depending on the N-N, N-Y, and Y-Y interaction models employed, the nucleon gaps may be either enhanced or reduced by the presence of hyperons.

Since the suggestion in [61] and the first detailed work of [62], hyperon gaps have attracted some attention. All uncertainties present in the nucleon case immediately translate to the hyperon case. An additional problem is that very little is known about hyperon-hyperon interactions<sup>7</sup> which is generally guessed

<sup>6</sup>In the presence of a charged  $\pi^-$  condensate a new Urca neutrino emission pathway is open, see Table 1. The development of a neutral  $\pi^0$  condensate has, however, little effect on neutrino emission.

<sup>7</sup>Some experimental information is available from hypernuclei [63, 64] and hadronic atoms [65], but the data do not yet uniquely determine the hyperon-nucleon or hyperon-

from theory by extrapolation from the N-N interaction. At densities not much larger than their threshold densities for appearance, hyperons have low enough concentration that they will pair in the  $^1S_0$  channel. In both cases of  $\Lambda$ 's and  $\Sigma^-$ 's, the estimated gap sizes are similar to those of nucleons. We refer the reader to [67, 68, 69] and references therein for details.

At very high densities, the presence of deconfined quark matter is also likely. Quarks are expected to pair and form a color superconductor. This subject has developed into a field of its own, and we dedicate Sec. 5 for a brief account and refer the reader to other articles in this monograph.

### 4.3 Effects of Pairing for Neutron Star Cooling

The occurrence of pairing leads to three important effects of relevance to neutron star cooling:

- A) Alteration, and possible strong suppression when  $T \ll T_c$ , of the specific heat  $c_V$  of the paired component.
- B) Reduction, and possible strong suppression when  $T \ll T_c$ , of the emissivity  $\epsilon_\nu$  of the neutrino processes the paired component is involved in.
- C) Triggering of the ‘‘Cooper pair breaking and formation’’ (PBF) with concomitant neutrino pair emission which is very efficient in the case of spin-triplet pairing.

These effects are direct consequences of the development of the energy gap  $\Delta(\mathbf{k})$  and the resulting two branches in the quasi-particle spectrum, Eq. (26). The gap severely limits the available phase space when  $T \ll T_c$  and the spectrum is usually treated in the effective mass approximation with an angle averaged gap, see Eq. (32),

$$\epsilon(\mathbf{k}) = \pm \sqrt{[\hbar v_F(k - k_F)]^2 + \overline{\Delta}(k_F, T)}, \quad (33)$$

where  $v_F \equiv \hbar k_F/m^*$ .

In cooling calculations, these effects are introduced through ‘‘control functions’’:

$$c_V \longrightarrow R_c c_V \quad \text{and} \quad \epsilon_\nu^X \longrightarrow R_X \epsilon_\nu^X. \quad (34)$$

There is a large family of such control functions for the various types of pairing and the numerous neutrino processes ‘‘X’’. For nodeless gaps, the  $R$ 's are Boltzmann-like factors  $\sim \exp[-2D(T)/k_B T]$  and result in a strong suppression when  $T \ll T_c$ , whereas for gaps with nodes the suppression is much milder. Regarding the specific heat, there is a sudden increase, by a factor  $\sim 2.4$  at  $T = T_c$ , followed by a reduction at lower  $T$ . Examples of such control functions are shown in Fig. 13.

---

hyperon interaction. Future work in lattice QCD [66] may prove fruitful, but current results are limited to unphysically large pion masses.



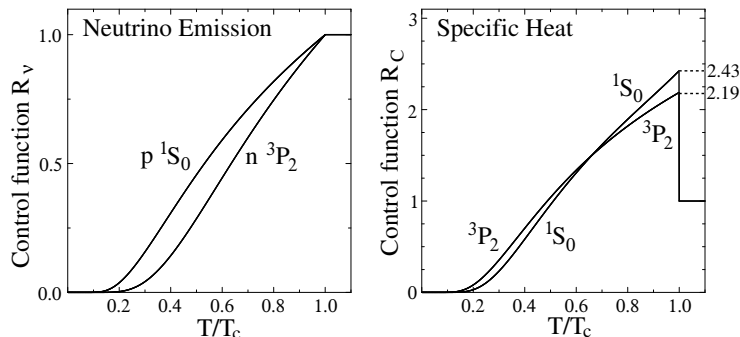


Figure 13: Control functions for neutrino emission from the modified Urca process (as, e.g.,  $n + n \rightarrow n + n + \nu\bar{\nu}$ ) (left panel) and the specific heat (right panel), in the presence of  $^1S_0$  pairing and  $^3P_2$  in the B phase (see Eq. (29)), from the analytical fits of [31] and [70].

The effect C, neutrino emission from the formation and breaking of Cooper pairs [71, 72], can be interpreted as an inter-band transition (as, e.g.,  $n \rightarrow n + \nu\bar{\nu}$ ) where a neutron/proton quasiparticle from the upper (+) branch of the spectrum of Eq. (33) falls into a hole in the lower (−) branch. Such a reaction is kinematically forbidden by the excitation spectrum of the normal phase, Eq. (20), but becomes possible in the presence of an energy-gap, Eq. (33). This process is described in more detail in Sec. 6.6. The resulting emissivity can be significantly larger than that of the modified Urca process (as, e.g.,  $n + n \rightarrow n + n + \nu\bar{\nu}$ ) in the case of spin-triplet pairing.

## 5 Superfluidity in Dense Quark Matter

The central densities of neutron stars can exceed the nuclear density  $\rho_{\text{nuc}} \sim 2.7 \times 10^{14} \text{ g cm}^{-3}$  by significant amounts. At sufficiently high densities, a description of neutron star interiors in terms of nucleons becomes untenable and sub-nucleonic degrees of freedom, namely quarks, must be invoked. Interactions between quarks is fundamentally grounded in Quantum Chromodynamics (QCD), the theory of strong nuclear interactions. The theory has a gauge symmetry based on the Lie group  $SU(3)$ , and the associated charge is referred to as “color”. QCD is asymptotically free: interactions between quarks mediated by gluons become weak at short distances, or equivalently, high densities. At low densities, strong interactions “confine” quarks into neutrons and protons which are color neutral. Asymptotic freedom guarantees that, at some large density, the ground state of zero-temperature matter will consist of nearly-free, “deconfined” quarks [73].

QCD has been amply tested by experiments at high energies where asymptotic freedom has been confirmed [74]. Lattice-gauge calculations of hadron

masses, and of baryon-free matter at finite temperature, have made enormous strides in recent years [75]. However, first-principle QCD calculations for finite baryon density have been stymied due to the fermion-sign problem in lattice gauge calculations. While many guesses are available, perturbation theory is unable to accurately predict the density at which the deconfinement phase transition occurs. However, it is possible that the phase transition occurs at a density lower than the central density of some (or even all) neutron stars. In that case, at least some neutron stars will contain deconfined quark matter. Such objects are referred to as hybrid quark stars. In their cores, up ( $u$ ), down ( $d$ ), and strange ( $s$ ) quarks are the principal degrees of freedom, the other three quark flavors (charm ( $c$ ), bottom ( $b$ ), and top ( $t$ )) being excluded because of their large masses. It is theoretically possible that the energy of zero-pressure strange quark matter has a lower energy than Fe [76, 77, 78], in which case a hybrid star would be metastable or unstable, and nucleonic matter would spontaneously convert into strange quark matter, creating pure quark stars that are self bound [79, 80]. There is no experimental or observational evidence for pure quark stars, however, and we do not consider them further in this contribution.

## 5.1 Pairing in Quark Matter

Cooper pairing between quarks was first investigated in the late 1970s [81, 82]. As all quarks are charged, pairing between quarks is often referred to as color superconductivity because the paired phase breaks the  $SU(3)$  gauge symmetry of QCD. First estimates of pairing gaps in quark matter were of order 1 MeV. In this case, neutron stars with deconfined quark matter cool very rapidly through the quark direct Urca processes (see Table 1). Because some older neutron stars are observed to be relatively warm, this naturally implies that not all neutron stars can contain quark matter.

This situation changed drastically with the discovery [83, 84] that color superconductivity implies gaps as large as 100 MeV (see a recent review in [85]). These works suggested two possibilities: either the so-called “color-flavor-locked” (CFL) phase in which all nine combinations of flavor (up, down, strange) and color (red, green, blue) participate in pairing, or the “2SC” phase where only four of the nine combinations pair (corresponding to up and down quarks which are either red or green).

## 5.2 Theoretical Descriptions of Dense Quark Matter

There are several formalisms which have been applied to describe color superconducting quark matter. High-density effective theories (HDET) were first developed in 1990s [86, 87] and then developed further for color superconductivity in [88, 89]. To construct an effective theory, one begins with the QCD Lagrangian, rewrites it in terms of a  $1/\mu$  expansion ( $\mu$  being the chemical potential), and then integrates out hard gluons and fermionic modes corresponding to the Dirac sea.

Another commonly used alternative consists of using Nambu–Jona-Lasinio (NJL) [90] models. The original NJL model was a theory of strong interactions before the advent of QCD. The four-fermion interaction of the NJL Lagrangian bears close resemblance to that in the BCS theory of superconductivity and gives rise to analogous effects. Originally framed in terms of nucleon fields, quartic interactions serve to give the nucleon its mass through a self-energy generated by the formation of a condensate. Modern versions involve quark fields that develop a “quark condensate” which is then related to the mass of constituent quarks [91]. NJL models for color superconductivity presume that gluonic degrees of freedom have been integrated out resulting in point-like couplings between quarks. For a review of the NJL model applied to dense quark matter see [92]. Confinement is sometimes implemented by the addition of Polyakov loop terms giving rise to “PNJL” models. HDET and NJL methods give qualitatively similar results, but the NJL Lagrangian is a bit more transparent, so we describe some of its details here. A chiral SU(3) Lagrangian with superconducting quarks (adapted from [93]) is

$$\begin{aligned}
\mathcal{L} = & \bar{q}_{i\alpha} \left( i\partial_\mu \gamma^\mu \delta_{ij} \delta_{\alpha\beta} - m_{ij} \delta_{\alpha\beta} - \mu_{ij,\alpha\beta} \gamma^0 \right) q_{j\beta} \\
& + G_S \sum_{a=0}^8 \left[ \left( \bar{q} \lambda_f^a q \right)^2 + \left( \bar{q} i\gamma_5 \lambda_f^a q \right)^2 \right] \\
& + G_\Delta \sum_k \sum_\gamma \left( \bar{q}_{i\alpha} \epsilon_{ijk} \epsilon_{\alpha\beta\gamma} q_{j\beta}^C \right) \left( \bar{q}_{i'\alpha'}^C \epsilon_{i'j'k'} \epsilon_{\alpha'\beta'\gamma'} q_{j'\beta'} \right) \\
& + G_\Delta \sum_k \sum_\gamma \left( \bar{q}_{i\alpha} i\gamma_5 \epsilon_{ijk} \epsilon_{\alpha\beta\gamma} q_{j\beta}^C \right) \left( \bar{q}_{i'\alpha'}^C i\gamma_5 \epsilon_{i'j'k'} \epsilon_{\alpha'\beta'\gamma'} q_{j'\beta'} \right), \quad (35)
\end{aligned}$$

where Roman indices are for flavor and greek indices are for color, except for  $a$  which enumerates the SU(3) matrices,  $m_{ij}$  is the quark mass matrix,  $\mu_{ij,\alpha\beta}$  is the chemical potential matrix,  $q$  is the quark field,  $q^C = C\bar{q}^T$ , and  $\epsilon$  is the Levi-Civita tensor. The first term is the Dirac Lagrangian which describes free relativistic massive quarks at finite density. The second term is a combination of four quark fields which model non-superfluid quark-quark interactions and obeys the  $SU(3)_L \times SU(3)_R$  chiral symmetry present in QCD. The third and fourth terms, which give rise to color superconductivity, are the chirally symmetric analog of the second term in the quark-quark channel. QCD breaks  $U_A(1)$  symmetry, and so these four-fermion interactions can be supplanted by six-fermion interactions in order to do the same [94].

The first step in obtaining the thermodynamic potential in the mean-field approximation is to replace the quark bilinears  $\bar{q}_i q_i$  and  $\bar{q}_{i\alpha} i\gamma_5 \epsilon^{ijk} \epsilon^{\alpha\beta\gamma} q_{j\beta}^C$  with their ground-state expectation values. The former is the quark condensate associated with the breaking of chiral symmetry and the latter gives rise to the superconducting gap,  $\Delta^{k\gamma}$ . Having made this replacement, the non-constant terms in the Lagrangian take the form  $\bar{q} M q$ , where  $M$  is a matrix representing the inverse propagator. This matrix can be diagonalized in the standard way to obtain the individual quark dispersion relations and the thermodynamic

potential

$$\begin{aligned}\Omega = & -2G_S \sum_{i=u,d,s} \langle \bar{q}_i q_i \rangle^2 - \sum_k \sum_\gamma \frac{|\Delta^{k\gamma}|^2}{4G_\Delta} \\ & - \int \frac{d^3p}{(2\pi)^3} \sum_i \left[ \frac{\lambda_i}{2} + T \ln(1 + e^{-\lambda_i/T}) \right],\end{aligned}\quad (36)$$

where  $\lambda_i$  give the energy eigenvalues and  $i$  runs over 3 flavors, 3 colors, and the Dirac indices (36 total). In this formulation, there is a manifest parallelism between the quark condensates,  $\langle \bar{q}q \rangle$ , and the superconducting gaps. The minimum of the thermodynamic potential with respect to the superconducting gap gives the gap equation, and the minimum of the thermodynamic potential with respect to the quark condensates gives the “mass gap” equation, i.e. the equation which controls the dependence of the dynamically generated quark masses.

The energy eigenvalues  $\lambda_i$  cannot be computed analytically at all densities, except in two limiting situations. At low densities, where chiral symmetry is spontaneously broken, the gaps are zero. In this case, the quark dispersion relations are  $\sqrt{p^2 + m_i^{*2}} \pm \mu$ , where  $m_i^* = m_i - 4G_S \langle \bar{q}_i q_i \rangle$  are effective masses. The corresponding quark condensates are given by [95]

$$\langle \bar{q}_i q_i \rangle = -\frac{3}{\pi^2} \int_{p_{Fi}}^\Lambda p^2 dp \frac{m_i^*}{\sqrt{p^2 + m_i^{*2}}}. \quad (37)$$

At high densities, the gaps are larger than the quark masses, hence the latter do not play significant roles and can be ignored. With progressively increasing density color-flavor locking becomes increasingly perfect, hence the name the CFL phase. In this phase, we can assume flavor symmetry and 8 of 9 quarks (3 colors times 3 flavors) have the dispersion relation  $\sqrt{(p - \mu)^2 + \Delta^2}$ , while the remaining quark has the dispersion relation  $\sqrt{(p - \mu)^2 + 4\Delta^2}$ . In general, these properties are coupled so that both the masses and the gaps appear in the dispersion relations in a nontrivial fashion.

Results of calculations based on the above model are displayed in Fig. 14 using Eq. (35). The dynamically generated quark masses are larger than the current quark masses at low density where chiral symmetry is spontaneously broken. In the CFL phase, the superconducting gaps form among all three combinations of unlike flavors, up-down, up-strange, and down-strange. In the 2SC phase, the only pairing is between up and down quarks. This model exhibits a first-order phase transition between the gapped and ungapped phases, so the gaps do not continuously go to zero at low densities. The decrease in the gaps as a function of increasing density or large values of the quark chemical potential  $\mu$  is an artifact of the ultraviolet cutoff (a necessity imposed by the nonrenormalizable Lagrangian). HDET models show that the gaps increase with increasing  $\mu$ .

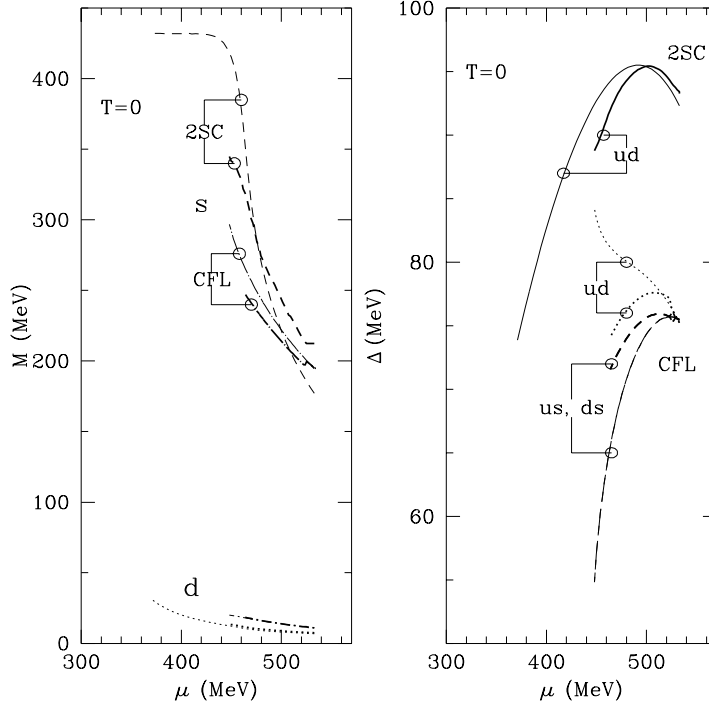


Figure 14: Down and strange dynamical quark masses (left panel) and superconducting gaps (right panel) as a function of density from [93]. The abscissa shows the quark chemical potential  $\mu$ . The thin (bold) curves show values when color neutrality is not (is) enforced. Different results are obtained in the CFL and 2SC phases as shown.

### 5.3 The Many Phases of Quark Matter

There are many different possible pairing configurations in addition to the CFL and 2SC phases described above, including gapless phases [96], and color-spin locked pairing. Color superfluids also admit a new set of Goldstone bosons associated with flavor rotations of the pairing condensate which have a similar group structure to the pseudoscalar Goldstone bosons in QCD ( $\pi$ ,  $K$ , etc.). These bosons can condense [97], forming a new phase of superconducting quark matter. The most common is the “CFL-K” phase which contains CFL quarks with a  $K$  meson condensate. All of these phases have their own associated exotic neutrino emissivities, including their own associated quark PBF neutrino cooling processes. A caricature phase diagram is shown in Fig. 15.

For densities near the deconfinement phase transition, the ground state of the quark superfluid may be similar to the Larkin-Ovchinnikov-Fulde-Ferrell [99, 100] (LOFF) pairing observed in condensed matter systems. LOFF pairing oc-

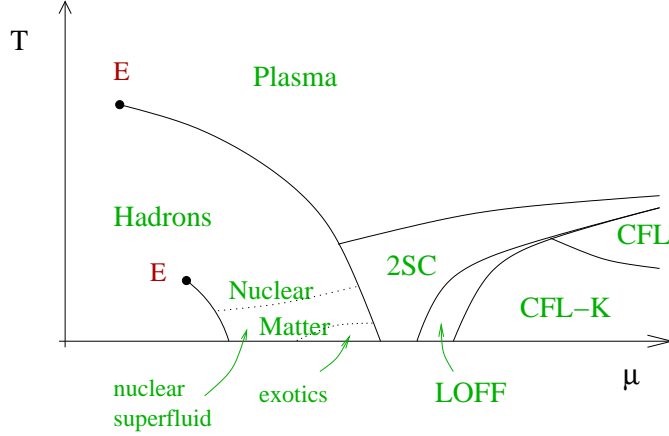


Figure 15: A schematic model QCD phase diagram, adapted from [98].

curs when two species participating in a pairing interaction have different Fermi momenta thus creating Cooper pairs with nonzero momentum. This pairing configuration breaks translational symmetry and encourages the formation a crystal. This creates a novel mechanism for pulsar glitches: the superfluid vortices pin to the crystalline part of the quark phase and during a glitch event the vortices move outwards by unpinning and repinning to the lattice [101]. This mechanism has not been either verified or ruled out by the data.

## 5.4 Detecting Quark Matter

The appearance of quark degrees of freedom often lowers the pressure at high densities, yielding neutron stars with smaller radii and smaller maximum masses compared to those in which quarks are absent. This is not guaranteed, however, as quark-quark interactions are sufficiently uncertain that quark matter can be nearly indistinguishable from matter consisting entirely of neutrons, protons, electrons and muons [102]. The presence (or absence) of quark matter will be difficult to determine from observations of neutron star structure alone. The neutron star mass-radius relation is dependent on the pressure of matter at a given energy density, but is insensitive to the nature of the particular degrees of freedom which provide that pressure. For this reason, it is natural to look to neutron star cooling to discern the composition of a neutron star's core. This topic will be considered in Sec. 7.7.

## 6 Neutrino Emission Processes

The thermal evolution of neutron stars with ages  $\lesssim 10^5$  yrs is driven by neutrino emission. We will here briefly describe the dominant processes; the interested reader can find a detailed description in [103] and an alternative point of view in [104]. Table 1 presents a short list of neutrino processes with estimates of their emissivities. Most noticeable is the clear distinction between processes involving 5 degenerate fermions with a  $T^8$  dependence, which are labeled as “slow”, and those with only 3 degenerate fermions with a  $T^6$  dependence, which are several orders of magnitude more efficient and labeled as “fast”. The difference in the  $T$  dependence is important and is simply related to phase space arguments which are outlined in Sec. 6.5. The last subsection, § 6.6, describes the “PBF” (Pair Breaking and Formation) process, which can provide a signal of the onset of a pairing phase transition that may be directly observable (and has likely been recently observed as described in Sec. 9).

### 6.1 The Direct Urca Process

The simplest neutrino emitting processes are Eq. (6) and Eq. (8) (see also Table 1), which collectively are generally referred to as the nucleon *direct Urca* (“DU” or “DUrca”) cycle. By the condition of  $\beta$ -equilibrium, both reactions naturally satisfy energy conservation, but momentum conservation is more delicate. Due to the high degree of degeneracy, all participating particles have momenta  $p(i)$  equal (within a small  $T \ll T_F$  correction) to their Fermi momenta  $p_F(i)$ . As  $p_F(i) \propto n_i^{1/3}$  and  $n_p \sim n_e \ll n_n$  in neutron star matter, momentum conservation is not *a priori* guaranteed. In the absence of muons and hence with  $n_p = n_e$ , the “triangle rule” for momentum conservation requires that the proton concentration  $x_p > 1/9 \simeq 11\%$ , whereas at  $\rho \sim \rho_{\text{nuc}}$  we have  $x_p \simeq 4\%$ . In the presence of muons, which appear just above  $\rho_{\text{nuc}}$ , the condition is stronger and one needs  $x_p$  larger than about 15% [105]. The proton fraction  $x_p$  grows with density (see Eq. (11)), its growth being directly determined by the growth of the nuclear symmetry energy, so that the critical proton fraction for the DU process is likely reached at some supra-nuclear density [105]. For the APR EOS [16] that we will frequently use, the corresponding critical neutron star mass for the onset of the nucleon DU process is  $1.97M_\odot$ , but other EOSs can predict smaller critical densities and masses.

It should also be noted that the direct Urca process, and for that matter, all the processes discussed in this section, can involve other leptons. Thus, for  $\rho \gtrsim \rho_{\text{nuc}}$ , where  $\mu^-$  appear, one also has

$$n \longrightarrow p + \mu^- + \bar{\nu}_\mu, \quad p + \mu^- \longrightarrow n + \nu_\mu. \quad (38)$$

Name	Process	Emissivity erg cm <sup>-3</sup> s <sup>-1</sup>	Efficiency
Modified Urca (neutron branch)	$\begin{cases} n + n' \rightarrow p + n' + e^- + \bar{\nu}_e \\ p + n' + e^- \rightarrow n + n' + \nu_e \end{cases}$	$\sim 2 \times 10^{21} R T_9^8$	Slow
Modified Urca (proton branch)	$\begin{cases} n + p' \rightarrow p + p' + e^- + \bar{\nu}_e \\ p + p' + e^- \rightarrow n + p' + \nu_e \end{cases}$	$\sim 10^{21} R T_9^8$	Slow
Bremsstrahlung	$\begin{cases} n + n' \rightarrow n + n' + \nu + \bar{\nu} \\ n + p \rightarrow n + p + \nu + \bar{\nu} \\ p + p' \rightarrow p + p' + \nu + \bar{\nu} \end{cases}$	$\sim 10^{19} R T_9^8$	Slow
Cooper pair	$\begin{cases} n + n \rightarrow [nn] + \nu + \bar{\nu} \\ p + p \rightarrow [pp] + \nu + \bar{\nu} \end{cases}$	$\begin{matrix} \sim 5 \times 10^{21} R T_9^7 \\ \sim 5 \times 10^{19} R T_9^7 \end{matrix}$	Medium
Direct Urca (nucleons)	$\begin{cases} n \rightarrow p + e^- + \bar{\nu}_e \\ p + e^- \rightarrow n + \nu_e \end{cases}$	$\sim 10^{27} R T_9^6$	Fast
Direct Urca ( $\Lambda$ hyperons)	$\begin{cases} \Lambda \rightarrow p + e^- + \bar{\nu}_e \\ p + e^- \rightarrow \Lambda + \nu_e \end{cases}$	$\sim 10^{27} R T_9^6$	Fast
Direct Urca ( $\Sigma^-$ hyperons)	$\begin{cases} \Sigma^- \rightarrow n + e^- + \bar{\nu}_e \\ n + e^- \rightarrow \Sigma^- + \nu_e \end{cases}$	$\sim 10^{27} R T_9^6$	Fast
Direct Urca (no-nucleon)	$\begin{cases} \Lambda + e^- \rightarrow \Sigma^- + \nu_e \\ \Sigma^- \rightarrow \Lambda + e^- + \bar{\nu}_e \end{cases}$	$\sim 2 \times 10^{27} R T_9^6$	Fast
Direct Urca ( $\pi^-$ condensate)	$\begin{cases} n + \langle \pi^- \rangle \rightarrow n + e^- + \bar{\nu}_e \\ n + e^- \rightarrow n + \langle \pi^- \rangle + \nu_e \end{cases}$	$\sim 10^{26} R T_9^6$	Fast
Direct Urca ( $K^-$ condensate)	$\begin{cases} n + \langle K^- \rangle \rightarrow n + e^- + \bar{\nu}_e \\ n + e^- \rightarrow n + \langle K^- \rangle + \nu_e \end{cases}$	$\sim 10^{25} R T_9^6$	Fast
Direct Urca cycle ( $u - d$ quarks)	$\begin{cases} d \rightarrow u + e^- + \bar{\nu}_e \\ u + e^- \rightarrow d + \nu_e \end{cases}$	$\sim 10^{27} R T_9^6$	Fast
Direct Urca cycle ( $u - s$ quarks)	$\begin{cases} s \rightarrow u + e^- + \bar{\nu}_e \\ u + e^- \rightarrow s + \nu_e \end{cases}$	$\sim 10^{27} R T_9^6$	Fast

Table 1: A sample of neutrino emission processes.  $T_9$  is temperature  $T$  in units of  $10^9$  K and the  $R$ 's are control factors to include the suppressing effects of pairing (see Sec. 4.3).



## 6.2 The Modified Urca Process

At densities below the threshold density for the nucleon DU process, where the DU process is forbidden at low temperatures, a variant of this process, the *modified Urca* (“MU” or “MUrca”) process (see Table 1) can operate, as advantage is taken of a neighboring nucleon in the medium [106] to conserve momentum. As it involves the participation of five degenerate particles, the MU process is much less efficient than the DU process. Unlike the nucleon DU process, which requires sufficient amount of protons, both branches of the MU process operate at any density when neutrons and protons are present.

## 6.3 Bremsstrahlung

Related to the MU processes is another class of processes, bremsstrahlung, made possible through neutral currents [107]. These differ from MU processes in that each reaction results in the production of a  $\nu\bar{\nu}$  pair, and the pair can have any neutrino flavor. Bremsstrahlung reactions are less efficient, by about 2 orders of magnitude, than the MU processes, but may make important contributions in the case that the MU process is suppressed by pairing of neutrons or protons. Bremsstrahlung involving electron-ion scattering is also an important source of neutrino emission in neutron star crusts:

$$e^- + (A, Z) \longrightarrow e^- + (A, Z) + \nu + \bar{\nu}, \quad (39)$$

where (A,Z) designates the participating ion.

## 6.4 Exotic Matter: Hyperons, Deconfined Quarks, Meson Condensates

In the presence of hyperons, DU processes which are obvious generalizations of the nucleon-only process, can also occur [59] and several are displayed in Table 1. When they appear, the  $\Lambda$ ’s initially have a density much smaller than that of the neutron and hence a smaller Fermi momentum. Consequently, momentum conservation in the  $\Lambda$  DU cycle is easily satisfied, requiring a  $\Lambda$  concentration  $x_\Lambda \sim 3\%$ . Notice that if the nucleon DU process is kinematically forbidden, the  $\Sigma^-$  DU process is also kinematically forbidden, whereas no-nucleon DU processes, of which one example is shown in Table 1, *are* possible. This particular no-nucleon DU process requires relatively low  $\Lambda$  and  $\Sigma^-$  threshold concentrations. Other examples involving  $\Sigma^-, \Sigma^0, \Sigma^+, \Xi^-$  and  $\Xi^0$  hyperons are given in [59].

In deconfined quark matter, DU processes involving all three flavors are possible, as indicated in Table 1. Rates for these processes have been calculated by Iwamoto [108].

Although not shown in Table 1, hyperons or quarks could also be involved in MU-like and bremsstrahlung processes (a quark MU process would involve an additional quark in the entrance and the exit channels, for example), but with greatly reduced rates compared to their corresponding DU processes and a  $T^8$

dependence. These processes are usually neglected since the DU processes are almost invariably allowed in the presence of hyperons or quarks.

In the presence of a meson condensate, copious neutrino emission in the processes listed in Table 1 occurs [109, 110]. As the meson condensate is a macroscopic object, there is no restriction arising from momentum conservation in these processes.

## 6.5 Temperature Dependence of Neutrino Emission

We turn now to briefly describe how the specific temperature dependence of the neutrino processes described above emerges. Consider first the simple case of the neutron  $\beta$ -decay. The weak interaction is described by the Hamiltonian  $\mathcal{H}_I = (G_F/\sqrt{2})B_\mu L^\mu$ , where  $G_F$  is Fermi's constant, and  $L^\mu = \bar{\psi}_e \gamma^\mu (1 - \gamma_5) \psi_\nu$  and  $B_\mu = \bar{\psi}_p \gamma_\mu (C_V 1 - C_A \gamma_5) \psi_n$  are the lepton and baryon weak currents, respectively. In the non relativistic approximation, one has  $B^0 = \cos \theta_c \Psi_p^\dagger \Psi_n$  and  $B^i = -\cos \theta_c g_A \Psi_p^\dagger \sigma^i \Psi_n$  where  $\theta_c$  is the Cabibbo angle and  $g_A$  the axial-vector coupling. Fermi's Golden rule gives us for the neutron decay rate

$$W_{i \rightarrow f} = \iiint \frac{d^3 p_\nu}{(2\pi)^3} \frac{d^3 p_e}{(2\pi)^3} \frac{d^3 p_p}{(2\pi)^3} (2\pi)^4 \delta^4(P_f - P_i) \cdot |M_{fi}|^2, \quad (40)$$

i.e., a sum of  $(2\pi)^4 \delta^4(P_f - P_i) \cdot |M_{fi}|^2$  over the phase space of all final states  $f = (\vec{p}_\nu, \vec{p}_e, \vec{p}_p)$ . The integration gives the well known result  $W_\beta = G_F^2 \cos^2 \theta_c (1 + 3g_A^2) m_e^5 c^4 w_\beta / (2\pi^3)$ , where  $w_\beta \sim 1$  takes into account small Coulomb corrections. This gives the neutron mean life,  $\tau_n \simeq 15$  minutes. Alternatively, a measurement of  $\tau_n$  determines  $G_F$  (modulo  $\cos \theta_c$  and  $w_\beta$ ).

The emissivity  $\epsilon^{\text{DU}}$  of the DU process (the Feynman diagram for this process is shown in Fig. 16) can be obtained by the same method, leading to

$$\epsilon^{\text{DU}} = \iiint \frac{d^3 p_{\bar{\nu}}}{(2\pi)^3} \frac{d^3 p_e}{(2\pi)^3} \frac{d^3 p_p}{(2\pi)^3} \frac{d^3 p_n}{(2\pi)^3} (1 - f_e)(1 - f_p) f_n (2\pi)^4 \delta^4(P_f - P_i) |M_{fi}|^2 E_\nu \quad (41)$$

with an extra factor  $E_\nu$  for the neutrino energy and the phase space sum now includes the initial  $n$ . The  $f_i$  terms,  $f_i$  being the Fermi-Dirac distribution for particle  $i$  at temperature  $T$ , take into account: (1) the probability to have a  $n$  in the initial state,  $f_n$ , and (2) the probabilities to have available states for the final  $e$  and  $p$ , denoted by  $(1 - f_e)$  and  $(1 - f_p)$ , respectively. We do not introduce a Pauli blocking factor  $(1 - f_{\bar{\nu}})$  for the anti-neutrino as it is assumed to be able to freely leave the star (i.e.,  $f_{\bar{\nu}} = 0$ ). When performing the phase space integrals, each degenerate fermion gives a factor  $T$ , as particles are restricted to be within a shell of thickness  $k_B T$  of their respective Fermi surfaces. The anti-neutrino phase space gives a factor  $T^3$ . The factors  $E_\nu$  is  $\sim T$  and the delta function  $\delta^4(P_f - P_i)$  gives a factor  $T^{-1}$  from  $\delta(E_f - E_i)$ . Altogether, we find that

$$\epsilon^{\text{DU}} \propto T^3 \cdot T \cdot T \cdot T \cdot \frac{1}{T} \cdot (1)^2 \cdot T = T^6, \quad (42)$$

where the  $(1)^2$  factor emphasizes that the squared matrix element  $|M_{fi}|^2$  is  $T$ -independent. An explicit expression for the neutrino emissivity for the DU process can be found in [105].

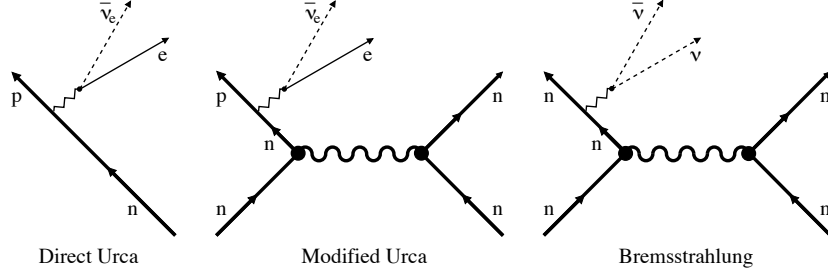


Figure 16: Feynman diagrams for the indicated neutrino emitting processes.

Figure 16 shows a Feynman diagram for the MU process. There are two more such diagrams in which the weak interaction vertex is attached to one of the two incoming legs. In this case, the  $T$ -power counting gives

$$\epsilon^{\text{MU}} \propto T^3 \cdot T \cdot T \cdot T \cdot T \cdot T \cdot \frac{1}{T} \cdot (1)^2 \cdot T = T^8. \quad (43)$$

In this case, the  $|M_{fi}|^2$  involves two strong interaction vertices, connected by the wavy line in Fig. 16, which is momentum independent and hence  $T$ -independent. The numerical difference  $\sim 10^{-6} T_9^2$  between the MU and the DU rates, see Table 1, comes mostly from the extra phase space limitation  $\propto T^2$  from the two extra nucleons: as a dimensionless factor it is  $(k_B T / E_F)^2 \simeq 10^{-6} T_9^2$  with  $E_F \simeq 100$  MeV and  $k_B 10^9$  K  $\simeq 0.1$  MeV. Notice that in the MU case, the internal neutron is off-shell by an amount  $\simeq \mu_e$  which does not introduce any extra  $T$ -dependence as we are working in the case  $E_F(e) \gtrsim 100$  MeV  $\gg T$ . Reference [106] contains the expression from which neutrino emissivity from the MU process can be calculated.

Turning to the  $n-n$  bremsstrahlung process, one diagram is shown in Fig. 16 and there are three more diagrams with the weak interaction vertices attached to the other three external lines. The  $T$ -power counting now gives

$$\epsilon^{\text{Br}} \propto T^3 \cdot T^3 \cdot T \cdot T \cdot T \cdot T \cdot \frac{1}{T} \cdot \left(\frac{1}{T}\right)^2 \cdot T = T^8 \quad (44)$$

with two  $T^3$  factors for the neutrino pair. The factor  $(T^{-1})^2$  arises from the matrix element as the intermediate neutron is almost on-shell, with an energy deficit  $\sim T$ , and its propagator gives us a  $T^{-1}$  dependence for  $M_{fi}$ . A working expression for the bremsstrahlung process can be found in [106].

## 6.6 The Cooper Pair Neutrino Process

The formation of the fermionic pair condensate also triggers a new neutrino emission process [71, 111, 112] which has been termed the “pair breaking and formation”, or PBF, process [113]. Whenever any two fermions form a Cooper pair, the binding energy can be emitted as a  $\nu - \bar{\nu}$  pair. Under the right conditions, this PBF process can be the dominant cooling agent in the evolution of a neutron star [114]. Such efficiency is due to the fact that the pairing phase transition is second order in nature. During the cooling of the star, the phase transition starts when the temperature  $T$  reaches  $T_c$  when pairs begin to form, but thermal agitation will constantly induce the breaking of pairs with subsequent re-formation and possible neutrino pair emission.

The emissivity of the PBF process (see the left panel of Fig. 17 for a Feynman diagram) can be written as

$$\epsilon^{\text{PBF}} = \iiint \frac{d^3 p_\nu}{(2\pi)^3} \frac{d^3 p_{\bar{\nu}}}{(2\pi)^3} \frac{d^3 p}{(2\pi)^3} \frac{d^3 p'}{(2\pi)^3} f(E_p) f(E_{p'}) \cdot (2\pi)^4 \delta^4(P_f - P_i) |M_{fi}|^2 \cdot E_\nu \quad (45)$$

Under degenerate conditions, the expression above can be reduced to read as

$$\begin{aligned} \epsilon^{\text{PBF}} &= \frac{12 G_F^2 m_f^* p_{F,f}}{15 \pi^5 \hbar^{10} c^6} (k_B T)^7 a_{f,j} R_j [\Delta_j(T)/T] \\ &= 3.51 \times 10^{21} \frac{\text{erg}}{\text{cm}^3 \text{ s}} \times \tilde{m}_f \tilde{p}_{F,f} T_9^7 a_{f,j} R_j [\Delta_j(T)/T] \end{aligned} \quad (46)$$

for a fermion  $f$  in a pairing state  $j = {}^1\text{S}_0$  or  ${}^3\text{P}_2$ . The coefficients  $a_{f,j}$  depend on the type of fermion and on the vector and axial couplings  $C_V$  and  $C_A$  (see, e.g., [52]). The control functions  $R_j$  are plotted in the right panel of Fig. 17. These functions encapsulate the effect that the PBF process turns on when  $T$  reaches  $T_c$  and practically turns off at  $T \lesssim 0.2 T_c$  when there is not enough thermal energy to break pairs.

The PBF process has had an interesting history. It was first discovered by Flowers, Ruderman, and Sutherland [71] and, independently, by Voskresensky and Senatorov [111]. It was, however, overlooked for 20 years, until implemented in a cooling calculation in [113] and its importance emphasized in [114]. Then in 2006, Leinson and Perez [115] showed that the previous computations of the PBF emissivity were incompatible with vector current (e.g. baryon number) conservation. Neutrino pair-production is mediated by the weak interaction, which can be decomposed in the traditional manner into vector and axial-vector parts. In pure neutron matter, the vector part of the PBF emissivity is suppressed because of vector current conservation by a factor of order  $(p_F/m^*c)^4 = (v_F/c)^4$ . This is equivalent to the simple observation that a one-component system of charges does not have a time-varying dipole moment [116]. The axial part of the PBF process is, however, unimpeded and dominates the emissivity.

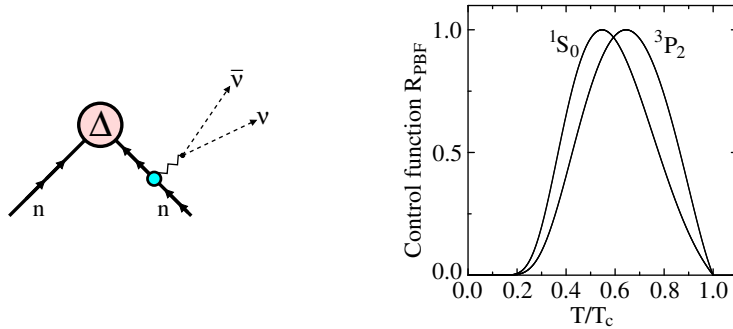


Figure 17: Left panel: Feynman diagram for  $\nu\bar{\nu}$  emission from the formation of a  $nn$  Cooper pair (pair breaking and formation, PBF, process). Right panel: control functions  $R_{\text{PBF}}$  for the PBF process.

### Temperature dependence of the PBF neutrino emissivity

The temperature dependence of the PBF process (left panel of Fig. 17) can be ascertained from Eq. (45) according to the following  $T$ -power counting:

$$\epsilon^{\text{PBF}} \propto T^3 \cdot T^3 \cdot T \cdot 1 \cdot \frac{1}{T} \cdot R(\Delta/T) \cdot T = T^7 R(\Delta/T), \quad (47)$$

where the two  $T^3$  and the first  $T$  factors arise from the phase space integrations of the neutrino pair and the first participating nucleon, respectively. The factor 1 results from the phase space integration of the second nucleon. As there are only two degenerate fermions in this process (in contrast to the Urca and bremsstrahlung processes that involve 3, 4, or 5 degenerate fermions), the momenta of the neutrino pair and the first nucleon are chosen the momentum of the second nucleon is fixed by the three-momentum conserving delta function. Thus, this second nucleon does not introduce any  $T$  dependence. The  $T^{-1}$  dependence arises from the energy conserving delta function. The last  $T$  factor is from the neutrino pair's energy, whereas the  $T$  and  $\Delta$  dependence of the matrix element of the reaction are included in the function  $R(\Delta/T)$ , which is shown in the right panel of Fig. 17.

An alternative way of looking at the PBF process is simply as an interband transition of a nucleon [117]. Considering the particle spectrum in a paired state (the right panel of Fig. 5), the lower branch (with  $\epsilon < \epsilon_F - \Delta$ ) corresponds to paired particles whereas the upper branch to excited ones, i.e., the “broken pair” leaves a hole in the lower branch. A transition of a particle from the upper branch to a hole in the lower branch corresponds to the formation of a Cooper pair.

### Dominance of triplet-pairing

In the non-relativistic limit for nucleons, the leading contribution from the axial-vector part is proportional to  $(v_F/c)^2$ . To this order, the control function  $R(z = \Delta/T)$  receives a contribution from the axial-vector part which can be expressed as [117]

$$R(z) = \frac{c_A^2}{8\pi} \int d\Omega \int_0^\infty \frac{z^6 dx}{(e^z + 1)^2} I, \quad (48)$$

where  $x = v_F(p - p_F)/T$  and the quantity  $I = I_{xx} + I_{yy} + I_{zz}$  with

$$I_{ik} = \sum_{\eta\eta'} \langle B | \hat{\Psi}^\dagger \sigma_i \hat{\Psi} | A \rangle \langle B | \hat{\Psi}^\dagger \sigma_k \hat{\Psi} | A \rangle^*, \quad (49)$$

where  $\hat{\Psi}$  is the second-quantized non-relativistic spinor wave function of the nucleons in superfluid matter (see [117] for its detailed structure in terms of the Bogoliubov transformation matrix elements  $U_{\sigma\eta}(\mathbf{p})$  and  $V_{\sigma\eta}(\mathbf{p})$ ),  $|A\rangle$  is the initial state of the system and  $|B\rangle$  its final state. The total spin states of the pair  $\eta, \eta'$  and  $\sigma$  each take on values  $\pm 1$  and  $\sigma_i$ 's are the Pauli spin matrices. The energy of a pairing quasiparticle is given by  $E = \sqrt{\epsilon^2 + \Delta_{\mathbf{p}}^2}$ , where  $\epsilon = v_F(p - p_F)$ . For singlet-state pairing, the momentum-dependent gap  $\Delta_{\mathbf{p}}$  is independent of  $\mathbf{p}$ , so that the occupation probabilities  $u_p$  and  $v_p$  associated with the matrix elements  $U_{\sigma\eta}(\mathbf{p})$  and  $V_{\sigma\eta}(\mathbf{p})$  depend only on  $p = |\mathbf{p}|$ . In the case of singlet pairing, the Bogoliubov matrix elements satisfy the symmetry properties  $V_{\alpha\beta}(-\mathbf{p}) = V_{\alpha\beta}(\mathbf{p})$  and  $V_{\alpha\beta}(\mathbf{p}) = -V_{\beta\alpha}(\mathbf{p})$ , so that the diagonal elements of this  $2 \times 2$  matrix are zero, and the non-diagonal elements are  $v_p$  and  $-v_p$ , respectively. These symmetry properties, together with the traceless property of the Pauli matrices, ensure that the quantity  $I = 0$ . Thus, to order  $(v_F/c)^2$ , the axial-vector part does not contribute in the spin-singlet channel rendering the triplet pairing channel, which does not vanish, to be the sole contribution to the PBF process.

### Time history of the PBF process

The Cooper pair neutrino process operates at different times in a neutron star's cooling history according to the time during which the local temperature is nearly equal to the critical temperature of any superfluid gap. In neutron stars consisting of neutrons, protons, and electrons, there are three relevant superfluid gaps: singlet neutron superfluidity, singlet proton superfluidity, and triplet neutron superfluidity at high densities when the singlet channel of the neutron-neutron interaction becomes repulsive above the saturation density. In neutron stars which contain exotic matter in their interiors, each additional superfluid fermion potentially opens up new Cooper pair cooling processes. If neutron stars contain deconfined quark matter in their cores, then pairing between quark flavors creates new Cooper pair neutrino processes which involve pairing between unlike fermions [118].

## 7 Cooling of Neutron Stars

The study of neutron star cooling is a Sherlock Holmes investigation, following the tracks of energy. At its birth, some 300 B (1 Bethe =  $10^{51}$  ergs) of gravitational energy are converted largely into thermal energy. About 98% of it is emitted in neutrinos during the first minute, the *proto-neutron star* phase, 1% is transferred to the supernova ejecta (with 1% of this 1% powering the light show), and the remainder is left in thermal energy of the *new-born neutron star*, i.e., the star produced during the proto-neutron star phase. Following the tracks of energy, the subsequent evolution of the neutron star can, in a simplified way, be described by an energy balance equation

$$\frac{dE_{th}}{dt} = C_V \frac{dT}{dt} = -L_\nu - L_\gamma + H, \quad (50)$$

where  $E_{th}$  is the star’s total thermal energy,  $C_V$  its specific heat, and  $L_\gamma$  and  $L_\nu$  its photon and neutrino luminosities, respectively. The term  $H$ , for “heating”, represents possible dissipative processes, such as friction from differential rotation or magnetic field decay. In this simplified equation it is assumed that the star’s interior is isothermal with temperature  $T$ , a state reached within a few decades after birth in the core-collapse supernova (see Sec. 7.4). A more detailed study would include general relativistic effects and consider a local energy balance equation for each layer in the star, instead of the global one of Eq. (50), complemented by a heat transport equation, in order to follow the evolution of the temperature profile in the stellar interior (see, e.g., [51] and references therein).

After the proto-neutron star phase, matter is highly degenerate within most of the star, except the outermost, lowest density, layers. As a consequence, the gross structure of the star does not evolve with time and is determined, once and for all, by solving the Tolman-Oppenheimer-Volkoff equations [13] of hydrostatic equilibrium. An equation of state is required to not only solve these equations, which determine the mass and radius of the star, but also to evaluate the internal chemical composition of each species of nucleus and particle as well as their effective masses, chemical potentials, specific heats, etc. A complete cooling model requires, moreover, inclusion of neutrino and surface photon emissions as well as a description of the pairing properties of matter, i.e., the pairing gaps for each fermionic species, together with their respective density dependences.

Within the isothermal approximation of Eq. (50), the three major ingredients needed for the study are  $C_V$ ,  $L_\gamma$ , and  $L_\nu$ . Neutrino emission processes were described in Sec. 6 and the specific heat and photon emission are briefly described below. We continue this section by describing simple analytical solutions of Eq. (50) and displaying the results of representative numerical simulations of the complete set of general relativistic evolutionary equations.

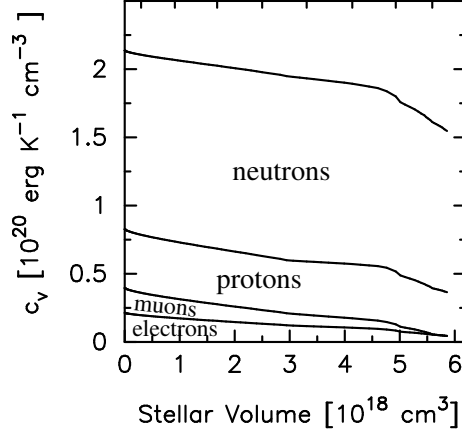


Figure 18: Cumulative specific heats of  $e$ ,  $\mu$ ,  $p$ , and  $n$  as a function of stellar volume within the core of a  $1.4 M_{\odot}$  star built using the APR EOS at  $T = 10^9$  K. Nucleons are assumed to be unpaired which implies  $c_v \propto T$ . No hyperons or quarks are permitted by the EOS. This figure is adapted from [51].

## 7.1 Specific Heat

The dominant contributions to the specific heat  $C_V$  come from the core, which makes up more than 90% of the total volume and 98% of the mass. Its constituents are quantum liquids of leptons, baryons, mesons, and, possibly, deconfined quarks at the highest densities. Hence, one has

$$C_V = \sum_i C_{V,i} \quad \text{with} \quad C_{V,i} = \iiint c_{v,i} dv, \quad (51)$$

where  $c_{v,i}$  is the specific heat per unit volume of constituent  $i$  ( $i = e, \mu, n, p$ , hyperons, quarks), but those of meson condensates is usually neglected.. For normal (i.e., unpaired) degenerate fermions, the standard Fermi liquid result [119]

$$c_{v,i} = N(0) \frac{\pi^2}{3} k_B^2 T \quad \text{with} \quad N(0) = \frac{m_i^* p_{F,i}}{\pi^2 \hbar^3} \quad (52)$$

can be used, where  $m^*$  is the fermion's effective mass. In Fig. 18, the various contributions to  $C_V$  are illustrated.

When baryons, and quarks, become paired, as briefly described in Sec. 4.3, their contribution to  $C_V$  is strongly suppressed at temperatures  $T \ll T_c$  ( $T_c$  being the corresponding critical temperature). Extensive baryon, and quark, pairing can thus significantly reduce  $C_V$ , but by no more than a factor of order ten because leptons do not pair. The crustal specific heat is, in principle, dominated by neutrons in the inner crust but, as these are certainly extensively paired, only the nuclear lattice and electrons contribute in practice.



## 7.2 Photon Thermal Luminosity and the Envelope

The photon thermal luminosity  $L_\gamma$  is commonly expressed through the *effective temperature*  $T_e$  defined by

$$L_\gamma = 4\pi R^2 \sigma_{\text{SB}} T_e^4, \quad (53)$$

where  $\sigma_{\text{SB}}$  is the Stefan-Boltzmann constant. Thermal photons from the neutron star surface are effectively emitted at the *photosphere*, which is usually in an atmosphere, but could be located on the solid surface if a very strong magnetic field exists [17]. The atmosphere, which is only a few centimeters thick, contains a temperature gradient;  $T_e$  gives an estimate of its average temperature. The opacity in the atmosphere receives a strong contribution from free-free scattering that has a strong ( $\sim E^{-3}$ ) energy dependence. As a result photons of increasing energy escape from deeper and hotter layers and the emitted thermal spectrum shows an excess of emission in its Wien's tail compared to a blackbody of the same temperature  $T = T_e$  [120]. In the presence of heavy elements, “metals” in astronomical parlance, which may be not fully ionized, absorption lines increase the bound-free opacity contributions, and push the Wien's tail of the observable spectrum closer to the blackbody one. The presence of a strong magnetic field also alters the opacity in such way as to mimic a blackbody with the same chemical composition and  $T_e$ . There were great expectations that, with the improved spectral capabilities of *Chandra* and *Newton* observatories, many absorption lines would be observed and allow the determination of the gravitational redshifts and chemical composition of isolated neutron star surfaces. This expectation has, unfortunately, not been fulfilled; only in a very few cases have lines been detected, and their interpretation is controversial.

Observationally,  $L_\gamma$  and  $T_e$  are red-shifted and Eq. (53) is rewritten as

$$L_\gamma^\infty = 4\pi R_\infty^2 \sigma_{\text{SB}} (T_e^\infty)^4, \quad (54)$$

where  $L_\gamma^\infty = e^{2\phi} L_\gamma$ ,  $T_e^\infty = e^\phi T_e$ , and  $R_\infty = e^{-\phi} R$ . Here  $e^{-\phi} = 1 + z$ , with  $z$  being the redshift, and  $e^{2\phi}$  is the  $g_{00}$  coefficient of the Schwarzschild metric, i.e.,

$$e^\phi \equiv \sqrt{1 - \frac{2GM}{Rc^2}}. \quad (55)$$

Notice that  $R_\infty$  has the physical interpretation of being the star's radius corresponding to its circumference divided by  $2\pi$ , and would be the radius one would measure trigonometrically, if that were possible [121].

$L_\gamma^\infty$  and  $T_e^\infty$  are the observational quantities that are compared with theoretical cooling models. In principle, both are independently observable:  $T_e^\infty$  is deduced from a fit of the observed spectrum while  $L_\gamma^\infty$  is deduced from the observed total flux<sup>8</sup>, and knowledge of the distance  $D$ , via  $L_\gamma = 4\pi D^2 F$ . The star's distance can be deduced either from the radio signal dispersion measure, if it is a radio pulsar, or from the distance of an associated supernova remnant,

<sup>8</sup>The flux must, however, be corrected for interstellar absorption.

if any. Then Eq. (53) or (54) provides a consistency check: the inferred radius  $R$  should be of the order of 10 - 15 km. Given the lack of determination of the atmospheric composition from spectral lines, this consistency check is generally the only criterion to decide on the reliability of a  $T_e$  measurement from an atmosphere model spectral fit (besides the obvious requirement that the model must give a good fit to the data, i.e. a  $\chi^2 \simeq 1$ ).

In a detailed cooling calculation, the time evolution of the temperature profile in the star is followed. However, the uppermost layers have a thermal time-scale much shorter than the interior of the star and are practically always in a steady state. It is, hence, common to treat these layers separately as an *envelope*. Encompassing a density range from  $\rho_b$  at its bottom (typically  $\rho_b = 10^{10}$  g cm $^{-3}$ ) up to  $\rho_e$  at the photosphere ( $\rho_e \lesssim 1$  g cm $^{-3}$ ), and a temperature range from  $T_b$  to  $T_e$ , the envelope is about one hundred meters thick. Due to the high thermal conductivity of degenerate matter, stars older than a few decades have an almost uniform internal temperature, except within the envelope which acts as a thermal blanket insulating the hot interior from the colder surface. A simple relationship between  $T_b$  and  $T_e$  can be formulated [122]:

$$T_e \simeq 10^6 \left( \frac{T_b}{10^8 \text{ K}} \right)^{0.5+\alpha} \quad (56)$$

with  $\alpha \ll 1$ . The precise  $T_e - T_b$  relationship depends on the chemical composition of the envelope. The presence of light elements like H, He, C, or O, which have large thermal conductivities, leads to a larger  $T_e$  for the same  $T_b$  relative to the case of a heavy element, such as iron, envelope. Light elements are not expected to survive densities larger than  $\sim 10^{10}$  g cm $^{-3}$  due to pycnonuclear reactions. Thus, the maximum possible mass in light elements amounts to  $\Delta M_{\text{Light}} \simeq 10^{-6} M_{\odot}$ , which is enough to raise  $T_e$  by a factor of two. Magnetic fields also alter the  $T_e - T_b$  relationship, but to a lesser extent (see, e.g., [123] for more details) unless they are super-strong as in the case of magnetars, i.e.  $B_s \sim 10^{15}$  G.

### 7.3 Analytical Solutions

As the essential ingredients entering Eq. (50) can all be approximated by power-law functions, one can obtain simple and illustrative analytical solutions (see also [124]). We adopt the notation

$$C_V = C_9 T_9, \quad L_\nu = N_9 T_9^8, \quad \text{and} \quad L_\gamma = S_9 T_9^{2+4\alpha}, \quad (57)$$

where  $T_9 \equiv T/(10^9 \text{ K})$  refers to the isothermal temperature  $T_b$  in the star's interior. As written,  $L_\nu$  considers slow neutrino emission involving five degenerate fermions from the modified Urca and the similar bremsstrahlung processes, summarized in Table 1. The photon luminosity  $L_\gamma$  is obtained from Eq. (53) using the simple expression in Eq. (56). We will ignore redshift. Typical parameter values are  $C_9 \simeq 10^{39}$  erg K $^{-1}$ ,  $N_9 \simeq 10^{40}$  erg s $^{-1}$  and  $S_9 \simeq 10^{33}$  erg s $^{-1}$  (see Table 3 in [123] for more details). In young stars, neutrinos dominate

the energy losses (in the so-called *neutrino cooling era*), and photons take over after about  $10^5$  years (the *photon cooling era*).

**Neutrino cooling era:** In this case  $L_\gamma$  can be neglected in Eq. (50), so that

$$t = \frac{10^9 C_9}{6N_9} \left( \frac{1}{T_9^6} - \frac{1}{T_{0,9}^6} \right) \rightarrow T_9 = \left( \frac{\tau_{\text{MU}}}{t} \right)^{1/6} \quad (\text{when } T \ll T_0) \quad (58)$$

with a MU cooling timescale  $\tau_{\text{MU}} = 19^9 C_9 / 6N_9 \sim 1$  year when the star reaches the asymptotic stage ( $T \ll T_0$ ,  $T_0$  being the initial temperature at time  $t = 0$ ). The observed slope of the *cooling track* during the asymptotic stage is

$$\left| \frac{d \ln T_e}{d \ln t} \right| \simeq \frac{1}{12} + \frac{\alpha}{6}, \quad (59)$$

using the core-envelope relation Eq. (56). This slope is not sensitive to the core-envelope relation.

**Photon cooling era:** In this era,  $L_\nu$  is negligible compared to  $L_\gamma$ . Since  $|\alpha| \ll 1$ , one finds

$$t = t_1 + \tau_\gamma [\ln T_9 - \ln T_{1,9}] \rightarrow T_9 = T_{1,9} e^{(t_1 - t)/\tau_\gamma}, \quad (60)$$

where  $T_1$  is  $T$  at time  $t = t_1$  and  $\tau_\gamma = 10^9 C_9 / S_9 \sim 3 \times 10^7$  years, the photon cooling timescale. The observed slope of the cooling track is, when  $T \ll T_1$ ,

$$\left| \frac{d \ln T_e}{d \ln t} \right| \simeq \frac{t}{2\tau_\gamma}. \quad (61)$$

This slope becomes steeper with time.

## 7.4 Numerical Simulations and the Effects of Pairing

Numerical simulations of a cooling neutron star use an evolution code in which the energy balance and energy transport equations, in their fully general relativistic forms, are solved, usually assuming spherical symmetry and with a numerical radial grid of several hundred zones<sup>9</sup>. Compared to the analytic solutions discussed in Sec. 7.3, detailed conductivities, neutrino emissivities, and possible pairing are taken into account.

A set of cooling curves that illustrate the difference between cooling driven by the modified Urca and the direct Urca processes is presented in Fig. 19. Cooling curves of eight different stars of increasing mass are shown, using an equation of state model from [125], which allows the DU process at densities above  $1.35 \times 10^{15} \text{ g cm}^{-3}$ , i.e., above a critical neutron star mass of  $1.35 M_\odot$ . Notice that the equation of state used has parameters *specifically adjusted* to obtain a critical mass of  $1.35 M_\odot$  which falls within the expected range of isolated neutron star masses; other equations of state can result in very different

<sup>9</sup>Such a code, NSCool, is available at: <http://www.astroscu.unam.mx/neutrones/NSCool/>

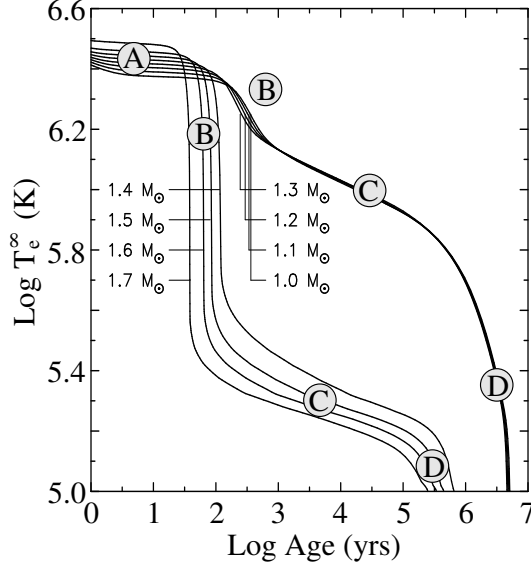


Figure 19: Cooling curves illustrating the difference between slow cooling driven by the modified Urca process, for masses below  $1.35M_{\odot}$ , and fast cooling from the direct Urca process in more massive stars [57].

critical masses. The difference arising from *slow* and *fast* neutrino processes is clear. The various cooling phases, A to D are discussed below.

To further illustrate some of the possible cooling behaviors of neutron stars, and the effects of pairing, we show in Fig. 20 simulations based on a  $1.4M_{\odot}$  star built with the APR EOS [16] and a heavy-element envelope. The “slow cooling” models include, in the core, the slow neutrino processes of Table 1 and the PBF process only. For the “fast cooling” models, a fast process with emissivity  $\epsilon_{Fast}^{(q)} = 10^q \cdot T_9^6 \text{ erg cm}^{-3} \text{ s}^{-1}$ , with  $q = 25, 26$ , and  $27$ , was added at  $\rho > 3\rho_{nuc}$ . These  $q$  values simulate neutrino emission from a kaon condensate, a pion condensate, or a direct Urca, respectively. These models, being based on the same EOS, are not self-consistent, but they have the advantage that the only differences among them is the presence or absence of the fast cooling process with  $\epsilon_{Fast}^{(q)}$  and the presence or absence of nucleon pairing. The models with pairing include the neutron  $^1S_0$  gap “SFB” of Fig. 10 in the inner crust, the  $^1S_0$  proton gap model “T” of Fig. 11, and the phenomenological neutron  $^3P\text{-}F_2$  gap “b” of the right panel of Fig. 12.

The distinctive phases of evolution are labelled “A”, “B”, “C”, and “D” on the cooling curves in Fig. 19 and above the cooling curves in the left panel of Fig. 20. Phases A and B are determined by the evolution of the crust while C and D reflect the evolution of the core. We describe these four phases in more detail according to Fig. 20:

**Phase A:** The effective surface temperature  $T_e$  here is determined by the evolution of the outer crust only. At such early stages, the temperature profile in the outer crust is independent of the rest of the star and, as a result, all models have the same  $T_e$ .

**Phase B:** The age of the star during this phase is similar to the thermal relaxation timescale of the crust, the heat flow in which controls the evolution of  $T_e$ . The evolution of the temperature profile for the fast cooling model with  $q = 26$  in the absence of pairing (marked as “Normal” in the left panel of Fig. 20) is depicted in the right panel of this figure 20. Very early in the evolution, a cold “pit” develops in the core where fast neutrino emission is occurring. During the first 30 years, heat flows from the outer core into this pit until the core becomes isothermal. Afterwards, heat from the crust rapidly flows into the cold core and the surface temperature  $T_e$  drops rapidly. Well before 300 years, during phase C, the stellar interior becomes isothermal and it is only within the shallow envelope, not shown in this figure to preserve clarity, that a temperature gradient is still present.

Notice that models of with pairing have shorter crust relaxation times due to the strong reduction of the neutron specific heat in the inner crust by  $^1\text{S}_0$  neutron superfluidity there.

**Phase C:** This is the “neutrino cooling phase” in which the star’s evolution is driven by neutrino emission from the core:  $L_\nu \gg L_\gamma$ . The difference between “slow” and “fast” neutrino emission, with or without core superfluidity, is clearly seen.

Quite noticeable is the effect of pairing-induced suppression of the neutrino emissivity in the fast cooling models. Once  $T$  drops below  $T_c$ , which happens only a few seconds or minutes after the star’s birth, neutrino cooling is quenched. Which fast cooling process occurs is much less important in the presence of pairing than in its absence. It takes half a minute, if  $q = 27$ , or half an hour, if  $q = 25$ , for the “pit’s” temperature to fall below  $T_c$ , which does not matter when looking at the star thousands of years later. The evolution is more dependent on  $T_c$  than on  $q$ .

In the case of the slow cooling models, the effects of pairing are more subtle than that in the fast cooling models, if one ignores the artificial case with the PBF process turned off. The burst of neutrino emission occurring when  $T \simeq T_c$ , from the PBF process, induces an additional, if temporary, rapid cooling episode. The impact of the PBF process, however, depends on the size of the neutron  $^3\text{P-F}_2$  gap. If the gap is large enough, the PBF cooling occurs during stage B and is hidden; if the gap is small enough, the PBF cooling occurs during stage D and is again hidden. *Only intermediate size gaps reveal the presence of the PBF process.* The effect of this gap on the evolution is considered in more detail in Sec. 8. The effect of the proton  $^1\text{S}_0$  gap is more subtle still, and its effects are considered in detail in Sec. 9.

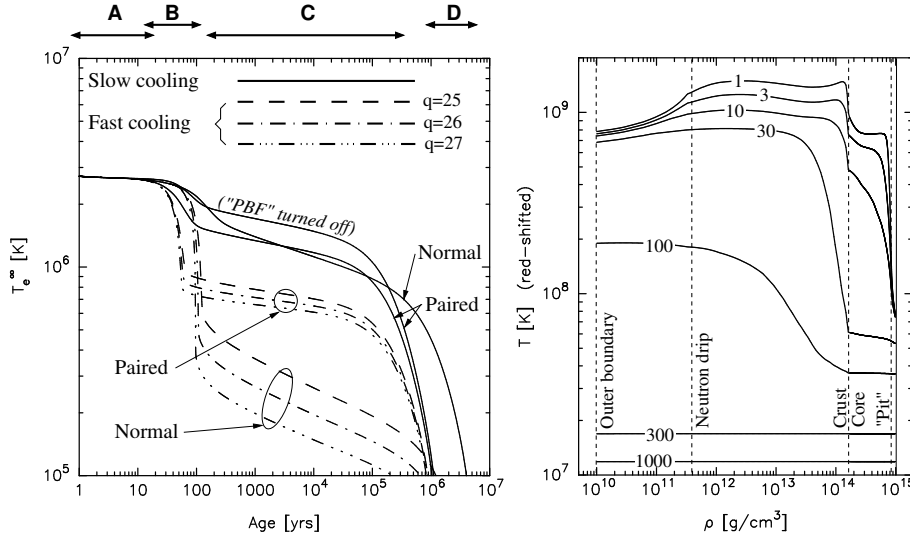


Figure 20: Left panel: cooling curves for various illustrative cooling scenarios. Right panel: temperature profile evolution for the fast cooling model with  $q = 26$ . The numbers on the curves give the age of the star, in years. See text for description. Figure taken from [126].

**Phase D:** At late times,  $L_\nu$  has decreased significantly due to its strong  $T$  dependence and photon emission,  $L_\gamma$ , which is less  $T$ -dependent, now drives the evolution. This is reflected by the larger slopes of the cooling curves. During this “photon cooling era”, models with pairing cool faster due to the reduction of the specific heat from superfluidity.

### The effect of a very strong magnetic field

In this contribution, we have neglected effects of the presence of a magnetic field. A strong magnetic field can alter the cooling of a neutron star in two ways. In the envelope and the crust, heat is transported by electrons. A surface magnetic field of strength  $\sim 10^{12}$  G, a typical value for the majority of pulsars, is sufficient to induce anisotropy in the thermal conductivity of the envelope resulting in a non-uniform surface temperature [121] that manifests itself as a modulation of the thermal flux with the pulsar’s rotational period. As mentioned in Sec. 7.2, this effect only slightly alters the  $T_b - T_e$  relationship of Eq. (56) [127]. However, a strong magnetic field deep in the crust [128] will have larger effects. For example, a  $\gtrsim 10^{14}$  G toroidal field within the crust can act as an efficient insulator, rendering most of the star’s surface very cold, but having two hot spots on the symmetry axis of the torus [129, 130]. This results in peculiar cooling trajectories [131]. The second effect of a magnetic field is that a slowly decaying field can act as a source of energy (i.e., the “H” term in Eq. (50))

which can keep old neutron stars warm. If the magnetic energy reservoir is large enough, and small scale magnetic structures exist that can decay rapidly<sup>10</sup>, aided by the Hall drift, the thermal evolution is significantly altered [132].

## 7.5 Observations of Cooling Neutron Stars

It is useful at this juncture to compare these general behaviors with observations. We summarize the observational information relevant to neutron star cooling in Fig. 21. The data is separated into three subsets of stars. In the upper panel of Fig. 21 are presented 13 stars for which a thermal spectrum, in the soft X-ray band (0.1 - 3.0 keV) is clearly detected. In the lower panel, we show data from 4 pulsars, labeled (A) through (D), that are seen in the X-ray band with a power-law spectrum, but whose detected emission is of magnetospheric origin. Since the surface thermal emission from these 4 stars is undetected, being covered by the magnetospheric emission, only upper limits on their effective temperatures could be inferred. Finally, the lower panel of this figure contains 6 upper limits resulting from the absence of detection of any emission from compact objects in 6 gravitational collapse supernova remnants, labeled (a) through (f), from a search by Kaplan and collaborators [133]. Since no compact object has been detected in these supernova remnants, some of them may contain an isolated black hole, but that is unlikely to be the case for all 6 of them. The observations and estimates of ages and temperatures, or upper limits, are detailed in [51] and updated in [52].

Estimates of surface temperatures (redshifted to infinity) require atmospheric modeling in which three factors are involved: (1) the composition of the atmosphere (i.e., H, He or heavy element); (2) the column density of X-ray absorbing material (mostly H) between the star and the Earth; and (3) the surface gravitational redshift. The column density is important because the bulk of the emitted flux is absorbed before reaching the Earth. The redshift does not affect blackbody models, but can influence heavy-element atmosphere models. In most cases, this quantity is not optimized, but set to the canonical value for  $M = 1.4M_{\odot}$  and  $R = 10$  km stars.

Narrow spectral lines are not observed in any of these sources, so their atmospheric compositions are unknown. However, some information can be deduced from the shape of the spectral distribution as heavy-element atmospheres closely resemble blackbodies. Fitting the flux and temperature of a source to a model yields the neutron star radius, if the distance is known. In some cases, clothing a star with a light-element atmosphere results in a predicted radius much larger than the canonical value, and one can infer the presence of a heavy-element atmosphere. Chang & Bildsten [134] have noted from such radius arguments that there exists a trend for stars younger than  $10^5$  years to be better fit by light-element atmospheres and stars older than  $10^5$  years to be better fit by heavy-element atmospheres. The possible evolution of stars leading to this trend is discussed further in [51].

---

<sup>10</sup>The Ohmic decay time, e.g., is  $\propto l^2$ ,  $l$  being the length-scale of the field structure.

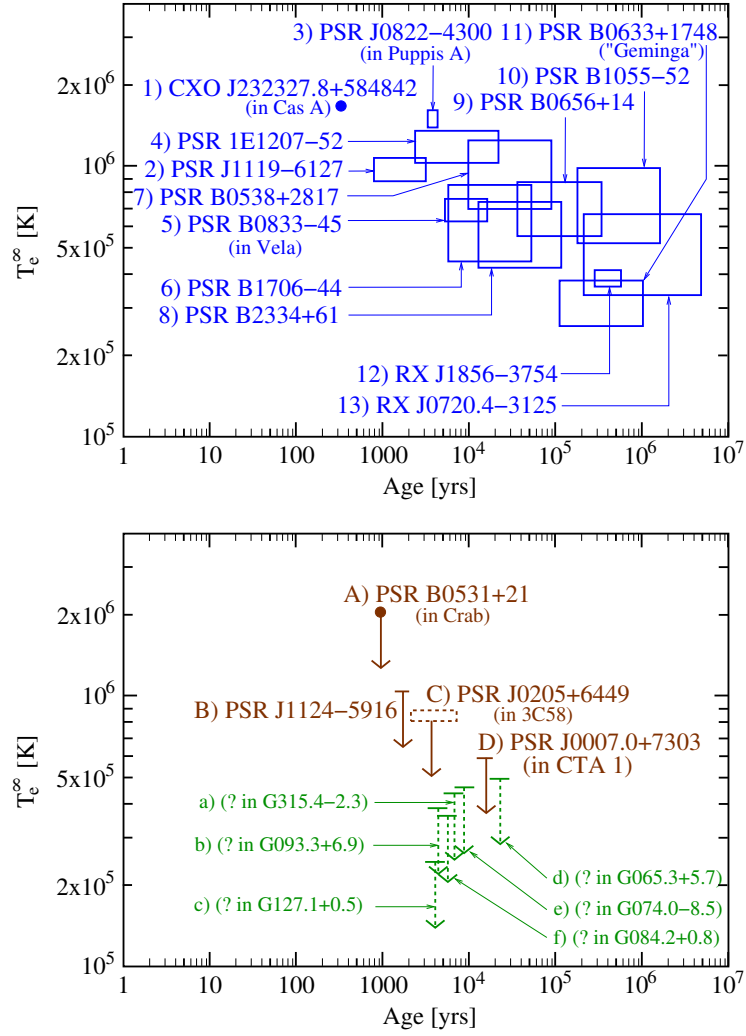


Figure 21: The present data set of cooling neutron stars. See text for presentation.



Before embarking on the presentation of detailed cooling scenarios and comparing them with data, it is worthwhile to discuss one general feature here. The four oldest stars, numbered 10 to 13 in Fig. 21, will appear to be much warmer than most theoretical predictions. These stars are prime candidates for the occurrence of some late “heating”, i.e. the “ $H$ ” term in Eq. (50). Models can be easily adapted to incorporate such heating (which has nothing to do with neutrino emission or pairing) that may become important at these times [123]. We will therefore concentrate on younger objects in the comparison with data.

## 7.6 An Example: Fast Cooling with Pairing

The thermal evolution of a neutron star undergoing fast neutrino emission was illustrated in Fig. 20 which showed that such a star, after the initial crust relaxation phase, has a very low  $T_e$  unless the neutrino emission is suppressed by pairing. In the presence of a gap that quenches fast neutrino emission, the resulting  $T_e$  is more sensitive to the size of the quenching gap than to the specific fast neutrino process in action.

In Fig. 22, we compare one specific scenario with the observational data described in the previous Sec. 7.5. This scenario employs the same EOS as in the models of Fig. 19 and is more realistic than what was described in Sec. 7.4 insofar as it takes into account uncertainties concerning the chemical composition of the envelope. If the neutron star has an envelope containing the maximum possible amount of light elements, ( $\sim 10^{-6}M_\odot$ ), its  $T_e$  is raised by a factor of two compared to the case when its envelope contains only heavy elements. Results for these two extreme scenarios of envelope composition are separately shown in the two panels of Fig. 20. In each panel, the first noticeable feature is the mass dependence of results when the mass exceeds  $1.35M_\odot$  and the direct Urca process is activated. This is partially due to the increasing size of the fast neutrino emitting “pit” as the star’s mass increases, but more dominantly due to the decrease in the neutron  ${}^3\text{P-F}_2$  gap with increasing density. More massive neutron stars, at least in this model, will have the direct Urca process acting in their inner cores for a longer time until their central temperatures drop below the corresponding central values of  $T_c$ . Notice that in a model where the  ${}^3\text{P-F}_2$  gap keeps growing with density as, in the “3bf” model of Fig. 12, this mass dependence essentially disappears.

When comparing the cooling trajectories of Fig. 22 with the displayed data we find that, with the exception of some of the oldest stars, all observed temperatures can be reasonably well fit. This result implies that different neutron stars have different masses, and some stars require an envelope containing light elements. This conclusion is common to all fast cooling scenarios that involve either the simple direct Urca process with nucleons or any direct Urca process with hyperons or quarks, as well as scenarios with charged mesons condensates. The successful *recipe* consists of having some fast neutrino process allowed in massive enough neutron stars. Then, in order to prevent intermediate mass stars from cooling too much, it is necessary to have a gap, or several gaps, large enough so that all fast neutrino processes are quenched at some point.

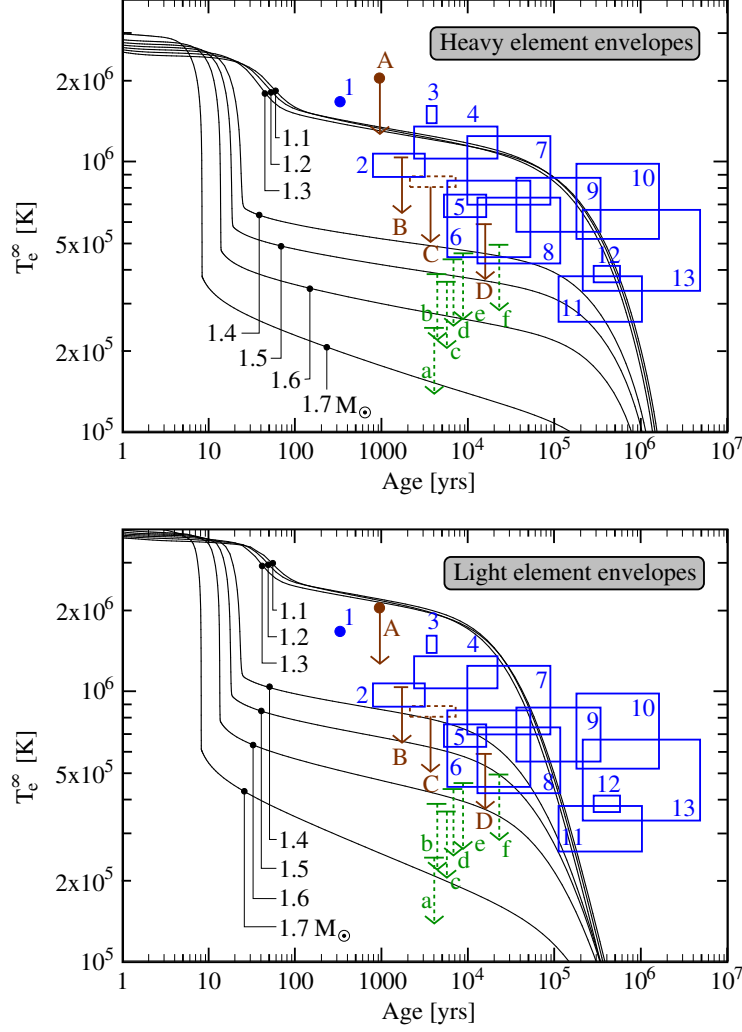


Figure 22: Comparison of a cooling scenario with data. The dense matter EOS used to build the stars is a PAL [125] version [57] that has only nucleons and leptons, and allows for the direct Urca process to occur in stars of mass larger than  $M_{\text{cr}} = 1.35M_{\odot}$ . Cooling trajectories are shown for seven different masses and two different envelope chemical compositions. The neutron  ${}^3\text{P-F}_2$  gap from model “b” of Fig. 12 is implemented while the neutron and proton  ${}^1\text{S}_0$  gaps are from models “SFB” of Fig. 10 and “T” from Fig. 11, respectively.

## 7.7 Can Quark Matter Be Detected from Cooling Observations?

The previous subsection presented one specific fast cooling scenario, while Sec. 7.4 only described very general trends of fast cooling scenario with pairing. It is interesting, however, to briefly consider if observations could determine not only whether or not fast cooling has occurred but also which fast cooling mechanism operates. The first study of cooling of hybrid stars with superconducting quarks [135] showed, in fact, that it will be difficult to establish that neutron stars contain deconfined quark matter based solely on the cooling data of isolated neutron stars. When quark superconductivity is present, for example in the 2SC phase, neutrino emission is suppressed by a factor of  $e^{-\Delta/T}$  for each flavor and color quark which is paired. Cooling in the CFL phase is special because of the Goldstone bosons, which provide new cooling processes, and other pairing configurations also have their own cooling behaviors. Quark gaps that are typically larger than baryonic gaps therefore imply that hybrid star cooling is driven by other degrees of freedom present at lower densities. On the other hand, small quark gaps, or the absence of quark matter entirely, imply similar cooling behaviors that are easily reproduced by models with varying masses.

The above conclusions are demonstrated in Fig. 23, in different ways in the two panels, using two pairs of EOSs. In the left panel, cooling curves with a fixed neutron star mass and employing two EOSs, one containing only nucleons (np) and the other with nucleons with quark matter (npQ), are shown. These simulations utilize a range of nucleon and quark pairing gaps. In the right panel, cooling curves of neutron stars of various masses and employing two EOSs, one with nucleons and hyperons (npH) and the other with quark matter added (npHQ), are compared. This second set of simulations utilizes fixed nucleon/hyperon/quark pairing gaps.

We refer the reader to [135] for details, but the figure illustrates that, given our poor knowledge of the size and density extent of the various pairing gaps, nearly indistinguishable cooling curves can be obtained with very different dense matter models, i.e with or without hyperons and/or with or without quark matter.

## 7.8 Can Superfluid Gaps Be Measured, or Predicted?

We are led, by the discussions in Sec. 7.6 and Sec. 7.7, to an intriguing result: *Any equation of state that permits fast neutrino emission is compatible with the presently available cooling data on isolated neutron stars IF pairing is present with gap(s) of the appropriate size(s).*<sup>11</sup> This result, unfortunately, is ambiguous: it means that theoretical uncertainties in the description of dense matter make it difficult to determine the composition of neutron star cores from isolated

---

<sup>11</sup>The ultimate theory of neutron star matter will yield the equation of state and the superfluid gaps. However, at present, this is far from being the case since the gaps, as described in Sec. 4, are very sensitive to many intricate Fermi surface processes to which the equation of state, which is a bulk property, is quite insensitive.

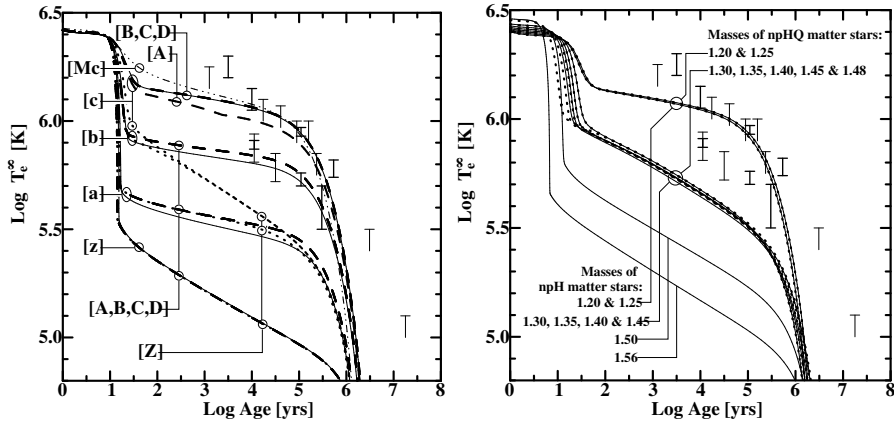


Figure 23: Left panel: cooling of a  $1.4M_{\odot}$  neutron star composed only of nucleons (continuous lines) or nucleons and quark matter (dashed and dotted curves), with various assumptions on the pairing gaps. Right panel: mass dependent cooling histories for two dense matter scenarios: “npH” matter contains nucleons and hyperons; “npHQ” matter also includes deconfined quarks. In these two scenarios, pairing gaps are assumed fixed. Figures from [135].

neutron star cooling observations alone.

One could, however, take an optimistic approach and reverse the argument. As the cooling of neutron stars is very sensitive to the presence, and the sizes, of pairing gaps, we can *apply this fact to attempt to measure the gap(s)* [57]. This is in line with the idea of using neutron stars as extra-terrestrial laboratories to study dense matter. However, as massive neutron stars may contain hyperons, meson condensates or deconfined quarks, the question arises: *which gap would we be measuring?* [135]. This situation, as demonstrated in the *maximally* complicated models of Fig. 23, may appear to render further studies of neutron star cooling a waste of time.

However, our discussion so far has assumed the presence of “fast” cooling. Is fast cooling, in fact, actually necessary? This question motivates the *minimal* cooling scenario, to which we turn in Sec. 8, which considers only models in which enhanced cooling processes do not occur.

## 8 Minimal Cooling and Superfluidity

The comparison in the previous section of theoretical cooling models with available data suggests the presence of extensive pairing in the cores of neutron stars. However, the plethora of possible scenarios makes it difficult to go beyond this generic conclusion. And, in spite of the fact that many theoretical models of dense matter predict the presence of some form of “exotica”, one should still

ask the question “do we need them?” and, if yes, how strong is the evidence for them? To address these questions, the *minimal cooling paradigm* was developed in [51, 52]. In this scenario, all possible fast neutrino emission processes (from direct Urca processes involving baryons or quarks, and from any form of exotica) are excluded *a priori*. Superfluid effects along with the PBF process are, however, included in the slow neutrino emission processes, such as the modified Urca processes involving neutrons and protons. This is a very restrictive scenario that minimizes the number of degrees of freedom, but fully incorporates uncertainties associated with the equation of state, envelope composition and its mass, etc. A detailed presentation of this scenario can be found in [51, 52] and a variant of it was developed by the Ioffe group in [136, 137]. Extensive studies of these two groups have pinned down two major sources of uncertainties: (i) our present lack of knowledge on the chemical composition of the envelope, and (ii) the size and extent of the neutron  ${}^3\text{P-F}_2$  gap. It turns out that, in the absence of any “fast process”, neutrino emissivity resulting from the PBF process involving  ${}^3\text{P-F}_2$  Cooper pairs is a major factor in the thermal evolution of a neutron star and its effect is strongly dependent on the size of the neutron  ${}^3\text{P-F}_2$  gap. We describe in some detail effects of the PBF process in the next subsection before turning to a comparison of the predictions of the minimal cooling paradigm with available data.

## 8.1 Effects of the PBF Induced Neutrino Process

The PBF process is distinctive in the sense that, in any layer in the star’s interior, it turns on when the temperature  $T$  reaches the corresponding  $T_c$  of the ambient density. Then the pairing phase transition is triggered and while  $T$  is not too much lower than  $T_c$ , there is constant formation and breaking of Cooper pairs induced by thermal excitation. However, when  $T$  falls below  $\sim 0.2T_c$ , there is not enough thermal energy to break pairs and the process shuts off (see its control function displayed in the right panel of Fig. 17). As described in Sec. 6.6 the neutrino emissivity of the PBF process is significant only in the case of anisotropic pairing, as in the case of a  ${}^3\text{P-F}_2$  gap.

The schematic Fig. 24 illustrates the effect of the pairing phase transition on the total neutrino luminosity of the star,  $L_\nu$ , depicted in the upper part of each panel as a function of the core temperature  $T$ . The long-dashed curves labelled “MUrca” show the modified Urca luminosity,  $L_\nu^{\text{MU}} \propto T^8$  in the absence of neutron  ${}^3\text{P-F}_2$  pairing while the short-dashed lines labelled “PBF” show the maximum possible PBF luminosity,  $L_\nu^{\text{PBF}} \propto T^7$ , i.e. from Eq. (46) with the control function  $R_j$  set to 1. The lower part of each panel shows a neutron  ${}^3\text{P-F}_2$   $T_c$  versus radius curve (displayed with its  $T$  axis horizontal to coincide with the upper part’s  $T$  axis). Assuming the temperature  $T$  to be nearly uniform in space in the entire core, the core  $T$  profile is just a vertical straight line that moves from the right to the left as the star cools down. Each panel considers a different type of  $T_c$  curve and in its upper part, the thick continuous line shows the actual evolution of the total  $L_\nu$  in the presence of pairing. As the star cools, and while  $T > T_{cn}^{\text{max}}$ , the total  $L_\nu$  is dominated by the MUrca process with small

contributions from other much less efficient processes. When  $T$  reaches  $T_{cn}^{\max}$ , there is a thick layer in which the phase transition starts and where neutrino emission from the PBF process is triggered which increases  $L_\nu$ . As  $T$  decreases, but is still larger than  $T_{cn}^{\min}$ , there will be one or two layers in the star where  $T$  is only slightly lower than the corresponding value of  $T_c$  in that layer(s) and where the PBF process is efficiently acting. (At these times, neutrino emission is strongly suppressed in the layers where  $T$  is much smaller than  $T_c$ .) Finally, when  $T$  drops well below  $T_{cn}^{\min}$ , neutrino emission by the dominant processes is suppressed everywhere in the core and  $L_\nu$  drops rapidly to reflect the much less efficient neutrino emissivity from the crust. The higher the value of  $T_{cn}^{\max}$  the earlier in the star's history will the enhanced cooling from the PBF process be triggered, while the lower the value of  $T_{cn}^{\min}$  the longer this enhanced cooling will last, as illustrated by the difference between the left and right panels of Fig. 24. This description will be pursued with a simple analytical model in Sec. 9.1 and 9.2.

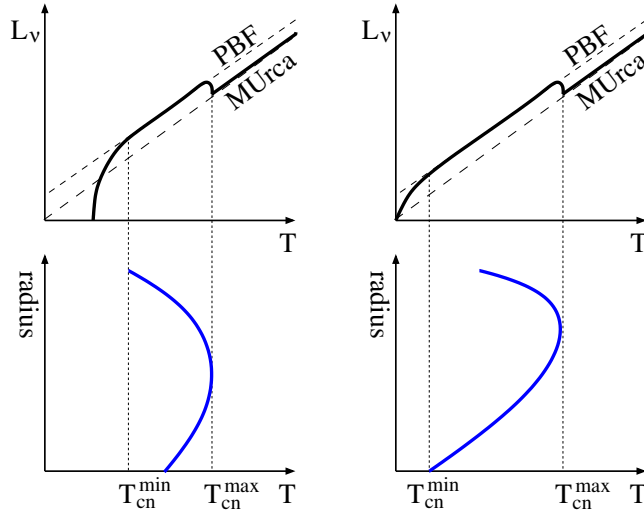


Figure 24: Schematic illustration of the PBF process induced neutrino luminosity as controlled by the shape of the  $T_c$  curve. See text for a detailed description.

From the above discussion, we learn that the effect of the PBF process depends strongly on the size and density dependence of the neutron  ${}^3\text{P-F}_2$  gap. To explore the possible impact of these two physical ingredients, we show in Fig. 25 two sets of cooling trajectories resulting from different assumptions. For contrast, both panels show a curve with no pairing, i.e., the same as the slow cooling model marked “Normal” in the left panel of Fig. 20. The various cooling curves are labelled by  $T_{cn}^{\max}$ , the maximum value of  $T_c$  reached in the stellar core. In the left panel, large values of  $T_{cn}^{\max}$  corresponding to the three phenomenological gaps “a”, “b”, and “c” of the right panel of Fig. 12, are

employed. All three gaps lead to the same result during the photon cooling era ( $t > 10^5$  yrs), but case “a” strongly differs from the other two cases during the neutrino cooling era. All three models have large enough gaps and  $T_{cn}^{\max}$  that the enhanced cooling from the PBF process started well before the end of the crust relaxation phase. The gaps and  $T_{cn}^{\min}$  of models “b” and “c” are so large that they induce a very strong suppression of  $L_\nu$  at early times and hence high values of  $T_e$  during the neutrino cooling phase. In contrast, the gap “a” has a moderate  $T_{cn}^{\max}$  and also a very small  $T_{cn}^{\min}$  which guarantees that at ages  $10^2 - 10^5$  yrs there is always a significant layer going through the pairing phase transition in which  $L_\nu^{\text{PBF}}$  is large which results in a colder star.

As small gaps have the strongest effect in inducing some enhanced cooling of the neutron star, we explore in the right panel of Fig. 25 the effect of increasingly small neutron  $^3\text{P-F}_2$  gaps by scaling down the model “a” gap by a factor 0.6, 0.4, and 0.2, respectively. A new feature now emerges: with decreasing values of  $T_{cn}^{\max}$ , the pairing phase transition is initiated at progressively later stages. This feature is signaled by cooling trajectories (dotted curves) departing from the  $T_{cn}^{\max} = 0$  trajectory. This late onset of pairing then manifests itself as a sudden rapid cooling of the star (due to the sudden increase of  $L_\nu$  from  $L_\nu^{\text{MU}}$  to  $L_\nu^{\text{PBF}}$  at the moment when  $T$  reaches  $T_{cn}^{\max}$ ) and interestingly within the age range for which we have many observations available.

Armed with these considerations, we turn now to compare the predictions of the minimal cooling paradigm with data.

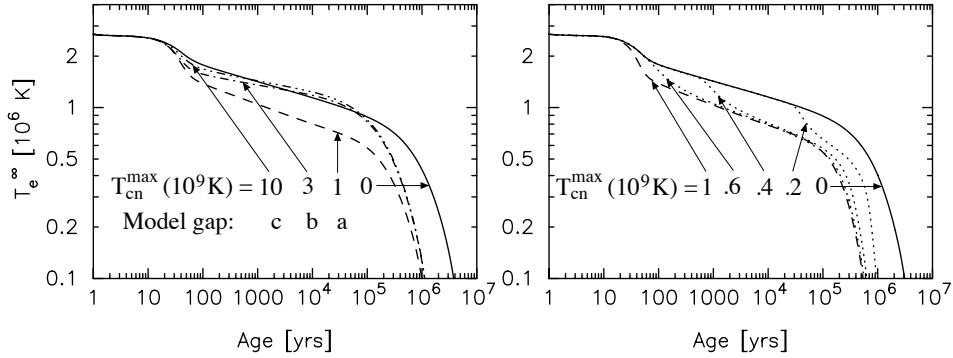


Figure 25: Neutron star cooling trajectories varying the magnitude of the neutron  $^3\text{P-F}_2$  gap. See text for description.

## 8.2 Comparison of Minimal Cooling With Observations

Fig. 26 shows ranges of predicted thermal evolutions of a canonical neutron star of  $1.4M_\odot$  built with the EOS of Akmal & Pandharipande [16]. The density dependence of the symmetry energy in this EOS precludes the occurrence of the direct Urca process in a  $1.4M_\odot$  neutron star. Furthermore, this EOS does

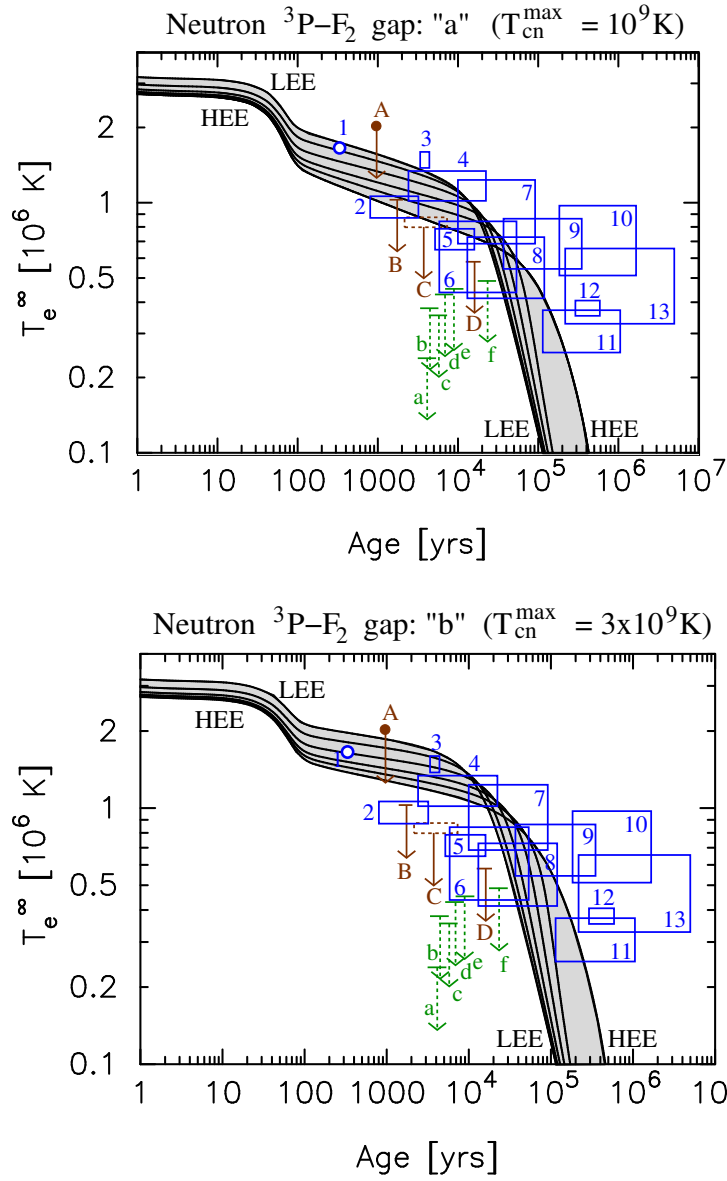


Figure 26: Comparison of two minimal cooling scenarios with observational data. The neutron  ${}^3\text{P}-\text{F}_2$  gaps employed are shown in Fig. 12. See text for description. Adapted from the results of [52]



not permit hyperons, kaon condensates, pions or deconfined quark matter, all of which could lead to enhanced cooling. It was shown in [51] that all EOS's compatible with the restrictions imposed by the minimal cooling scenario yield almost identical predictions. Moreover, within the range of neutron  ${}^3\text{P-F}_2$  pairing gaps explored, for which  $T_{cn}^{\text{max}}$  is reached at a density that is smaller than the central density of any neutron star (see right panel of Fig. 12), the neutron star mass of any model also has very little effect <sup>12</sup>.

The various possible assumptions about the neutron  ${}^1\text{S}_0$  gap have only a small effect on the early crust thermal relaxation phase, phase (B) of Fig. 20. Changes in the proton  ${}^1\text{S}_0$  gap produce significantly differing effects, but dominant effects are due to changes in the neutron  ${}^3\text{P-F}_2$  gaps. The full range of possibilities is (almost) covered by considering the two neutron  ${}^3\text{P-F}_2$  gaps in models “a” and “b” of Fig. 12 and is depicted in the two panels of Fig. 26. The various curves in the grey shaded areas show the uncertainty in the predictions due to lack of knowledge of the envelope compositions, which can range from pure heavy elements (“HEE”) to pure light elements (“LEE”). In agreement with the results of Fig. 25 and the discussion of the previous subsection, the large gap “b” results in warmer stars than the smaller gap “a” during the neutrino cooling era.

Comparing model tracks with observations, we can conclude, following [51] and [52], that if the neutron  ${}^3\text{P-F}_2$  gap is of small size ( $T_{cn}^{\text{max}} \sim 10^9$  K) as that of model “a” all neutron stars with detected thermal emission are compatible with the minimal cooling scenario with the exception of the oldest objects (labelled 10, 12, and 13 in Fig. 26, see the discussion at the end of Sec. 7.5). These older stars are candidates for the presence of internal heating, i.e., the “H” term in Eq. (50) [123], a possibility that can easily be incorporated within the minimal cooling scenario. In addition, it is found that young neutron stars must have heterogeneous envelope compositions: some must have light-element compositions and some must have heavy-element compositions, as noted above. The updated comparison by [52] more precisely quantifies the required size of this gap. In the notations used in Fig. 24, maximal compatibility of the minimal scenario requires the neutron  ${}^3\text{P-F}_2$  gap to satisfy  $T_{cn}^{\text{max}} \gtrsim 5 \times 10^8$  K and  $T_{cn}^{\text{min}} \lesssim 2 \times 10^8$  K. The constraint on  $T_{cn}^{\text{max}}$ , which determines when the PBF process will be triggered, derives from the necessity of having a PBF enhanced  $L_\nu$  already acting in the youngest observed stars at ages  $\lesssim 10^3$  yrs. On the other side, the constraint on the low  $T_{cn}^{\text{min}}$ , which determines when core neutrino emission will be strongly suppressed, including the PBF process, is obtained by the requirement that  $L_\nu$  should not be strongly suppressed before the star reaches an age of a few times  $10^4$  yrs. This constraint assures compatibility with the low  $T_e$  of objects 5 and 6. Considering the smooth  $k_F$ , and thus density, dependence of gaps, the constraint on  $T_{cn}^{\text{min}}$  likely prevents  $T_{cn}^{\text{max}}$  from being too large: gaps with  $T_{cn}^{\text{max}} \gg 10^9$  K usually also have  $T_{cn}^{\text{min}} \gg 10^8$  K.

<sup>12</sup> The Ioffe group, in their version of minimal cooling [136, 137], assumed neutron  ${}^3\text{P-F}_2$  gaps that are small at  $\rho_{\text{nuc}}$  and grow rapidly at high densities. Consequently,  $T_{cn}^{\text{max}}$  is reached in the center of the star and stars of increasing mass have increasing values of  $T_{cn}^{\text{max}}$  resulting in a mass dependence of the cooling evolution.

In the case the neutron  ${}^3\text{P-F}_2$  gap is as large as our model “b”, one reaches the opposite conclusion that minimal cooling cannot explain about half of the young isolated stars, implying the occurrence of some fast neutrino process. The same conclusion is also reached in the case this gap is very small. As seen in the left panel of Fig. 25, a vanishing gap leads to cooling trajectories very close to those obtained using large gaps during the neutrino cooling era.

Only one object, the pulsar in the supernova remnant CTA 1 (object “D” in the figure) for which only an upper limit on  $T_e$  is available, stands out as being significantly below all predictions of minimal cooling.

Finally, irrespective of the magnitude of the neutron  ${}^3\text{P-F}_2$  gap, if any of the six upper limits marked “a” to “f” in Fig. 26 are, in fact, neutron stars, they can only be explained by enhanced cooling. As it is unlikely that all of these remnants contain black holes, since the predicted neutron star/black hole abundance ratio from gravitational collapse supernovae is not small, these objects provide additional evidence in favor of enhanced cooling in some neutron stars<sup>13</sup>. As the nuclear symmetry energy likely increases continuously with density, larger-mass stars, which have larger central densities, likely have larger proton fractions and a greater probability of enhanced cooling. The dichotomy between minimal cooling and enhanced cooling might simply be due to a critical neutron star mass above which the direct Urca process can operate before being quenched by superfluidity.

### 8.3 Conclusions from the Minimal Cooling Paradigm

The study of the minimal cooling scenario allows progress beyond the conclusions reached in Sec. 7.8, but we are still faced with a clear dichotomy:

(1) In the case the neutron  ${}^3\text{P-F}_2$  gap is small in size (satisfying  $T_{cn}^{\min} \lesssim 2 \times 10^8$  K and  $T_{cn}^{\max} \gtrsim 5 \times 10^8$  K), neutron stars undergoing fast neutrino cooling must be relatively rare as among the dozen of known young isolated neutron stars, only one candidate, the pulsar in the supernova remnant CTA1, exists. This candidate is augmented by possible neutron stars represented by one or more of the (green) upper limits in Fig. 26. Nevertheless, the total number of fast cooling candidates remains small.

(2) In the case the neutron  ${}^3\text{P-F}_2$  gap is either larger, or smaller than in (1), a much larger fraction of neutron stars appear to undergo fast neutrino cooling.

Both conclusions are extremely interesting, but more information is needed to choose the (hopefully) correct one. Such information may be at hand and is presented in the next section. These conclusions also have implications in terms of neutron star masses. Neutron star mass measurements are only available for about 3 dozen pulsars in binary systems, and these may not be indicative

<sup>13</sup> Further evidence for enhanced cooling is provided by two neutron stars, SAX J1808.4-3658 and 1H 1905+00, in transiently accreting low-mass X-ray binaries. In contrast to the six, yet to be detected, candidates “a” to “f”, these two stars are known to be neutron stars from their characteristics during the accretion phases, but their thermal emission is not detectable after accretion stops, implying extremely fast neutrino emission occurring in their cores [138, 139].

of the overall neutron star population. However, we can appeal to theoretical predictions of the neutron star initial mass function, which are shown in Fig. 27. The predicted distributions are actually similar to the observed distributions from binary neutron stars [140]. In the case that conclusion (1) above is correct, the critical mass  $M_{\text{cr}}$  for fast neutrino cooling would appear to be much larger than the average mass, perhaps in the range  $1.6 - 1.8M_{\odot}$ . Alternatively, if conclusion (2) above is correct,  $M_{\text{cr}} \sim 1.4M_{\odot}$ , around the average mass.

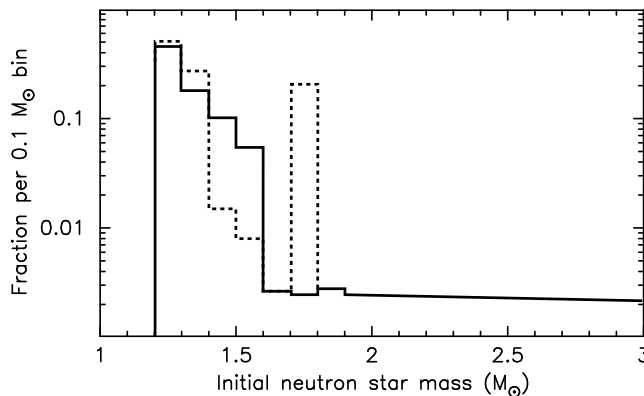


Figure 27: The initial mass function of neutron stars as predicted by stellar evolution models. The continuous line shows results from [141] and the dotted line is adapted from [10]. Figure from [15].

## 9 Cassiopeia A and its Cooling Neutron Star

The Cassiopeia A (Cas A) supernova remnant (SNR) was discovered in radio in 1947 and is the second brightest radio source in the sky (after the Sun). It has since then been observed at almost all wavelengths. Very likely, the supernova was observed by the first *Astronomer Royal*, John Flamsteed [142] who, on August 16, 1680, when describing the stars in the Cassiopeia constellation, listed the star “3 Cassiopeia” at a position almost coincident with the supernova remnant. This star had never been reported previously, and was never to be seen again, until August 1999 when the first light observation of **Chandra** found a point source in the center of the remnant (see Fig. 28).

The distance to the SNR is  $3.4^{+0.4}_{-0.1}$  kpc [143], and the direct observation, by the **Hubble Space Telescope**, of the remnant expansion implies a birth in the second half of the 17<sup>th</sup> century [144] and supports Flamsteed’s observation. These observations give a present age of 333 yrs for the neutron star in Cas A. The optical spectrum of the supernova has been observed through its light echo from scattering of the original light by a cloud of interstellar dust and shows the supernova was of type IIb [145]. The progenitor was thus a red supergiant

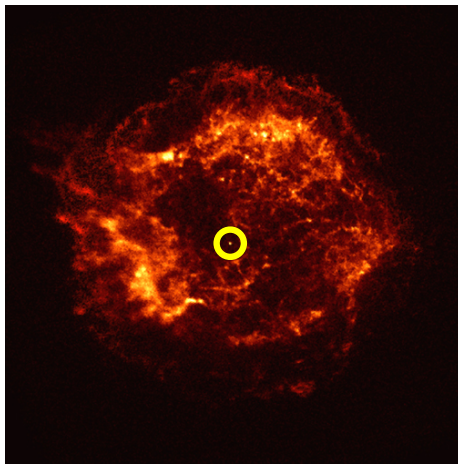


Figure 28: The Cassiopeia supernova remnant in X-rays: first light of **Chandra**, August 1999. (The neutron star is highlighted by the authors.) Image from ©NASA/CXC/SAO.

that had lost most of its hydrogen envelope, with an estimated zero age main sequence (ZAMS) mass of 16 to 20  $M_{\odot}$  [146, 147, 148] or even up to 25  $M_{\odot}$  in the case of a binary system [149]. This implies a relatively massive neutron star, i.e. likely  $\gtrsim 1.4 M_{\odot}$  [149]. The large amount of circumstellar material associated with mass loss from its massive progenitor could have diminished its visibility from Earth and could explain why it wasn't as bright as the two renaissance supernovae, Kepler's SN 1572 and Tycho's SN 1604.

The soft X-ray spectrum of the point source in the center of the SNR in Cas A is thermal, but its interpretation has been challenging [150]. With a known distance, a measurement of the temperature implies a measurement of the star's radius, but spectral fits with a blackbody or a H atmosphere model resulted in an estimated radius of 0.5 and 2 km, respectively. This suggests a hot spot, but that should lead to spin-induced variations in the X-ray flux, which are not observed. It was only in 2009 that a successful model was found: a non-magnetized<sup>14</sup> C atmosphere, which implies a stellar radius between 8 to 18 km [151]. Models with heavier elements, or a blackbody, produced significantly poorer fits. With the C model, and analyzing 5 observations of the SNR, Heinke & Ho [152] found that the inferred neutron star surface temperature had dropped by 4% from 2000 to 2009, from  $2.12$  to  $2.04 \times 10^6$  K, and the observed flux had decreased by 21%. The neutron star in Cas A, the youngest known neutron star, is the first one whose cooling has been observed in real time!

<sup>14</sup>There is, to date, no evidence for the presence of a significant magnetic field in the Cas A neutron star.

## 9.1 Superfluid Neutrons in the Core of Cas A

The *Chandra* observations of Cas A, together with its known distance, imply that the photon luminosity of the neutron star is

$$L_\gamma \simeq 10^{34} \text{ erg s}^{-1} . \quad (62)$$

With a measured  $T_e^\infty \simeq 2 \times 10^6$  K [151], we deduce an internal  $T \simeq 4 \times 10^8$  K from Eq. (56). The star's total specific heat is thus  $C_V \simeq 4 \times 10^{38}$  erg K<sup>-1</sup> (from Fig. 18 or Eq. (57)). The observed  $\Delta T_e^\infty / T_e^\infty \simeq 4\%$  [152] gives a change of core temperature  $\Delta T / T \simeq 8\%$  over a ten years period since  $T \sim (T_e^\infty)^2$ . Assuming the observed cooling corresponds to the *global cooling* of the neutron star, its thermal energy loss is

$$\dot{E}_{\text{th}} = C_V \dot{T} \simeq (4 \times 10^{38} \text{ erg K}^{-1}) \times (0.1 \text{ K s}^{-1}) \simeq 4 \times 10^{37} \text{ erg s}^{-1} , \quad (63)$$

which is 3–4 orders of magnitude larger than  $L_\gamma$ ! For a young neutron star, neutrinos are the prime candidates to induce such a large energy loss.

The cooling rate of this neutron star is so large that it must be a transitory event, which was initiated only recently. Otherwise it would have cooled so much it would probably now be unobservable. Something critical occurred recently within this star! “Something critical” for a cooling neutron star points toward a critical temperature, and a phase transition is a good candidate. The previous section highlighted that a phase of accelerated cooling occurs when the neutron <sup>3</sup>P-F<sub>2</sub> pairing phase transition is triggered. With  $T_{cn}^{\text{max}} \simeq 5 \times 10^8$  K, a transitory cooling episode can occur at an age  $\simeq 300$  yrs as shown in the right panel of Fig. 25 and in Fig. 29.

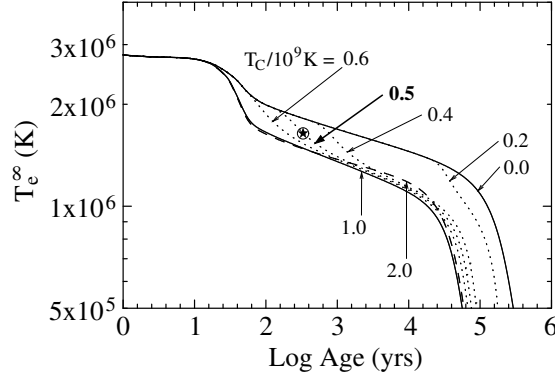


Figure 29: Similar to the right panel of Fig. 25, but showing the observed age and temperature of the Cas A neutron star (the star) and its consistency with  $T_C \simeq 5 \times 10^8$  K for the magnitude of the neutron <sup>3</sup>P-F<sub>2</sub> gap. Taken from [53].

The interpretation that the observed rapid cooling of the neutron star in Cas A was triggered by the recent onset of the neutron <sup>3</sup>P-F<sub>2</sub> superfluid phase

transition and consequent neutrino emission from the formation and breaking of Cooper pairs in the neutron superfluid was recently proposed in [53] and, independently, in [153].

### A simple analytical model

The simple analytical solution of Eq. (58) gives some insight into the observed behavior. When  $T > T_C \equiv T_{cn}^{\max}$ , but  $\ll T_0$ , the star follows the asymptotic “MU trajectory”,  $T_9 = (\tau_{\text{MU}}/t)^{1/6}$ , and when  $T$  reaches  $T_C$ , at time  $t = t_C$ , the neutrino luminosity suddenly increases (see Fig. 24). Despite the complicated  $T$  dependence of  $\epsilon^{\text{PBF}}$ , Eq. (46), the resulting luminosity, once integrated over the entire core (also, aided by the bell shape of the  $T_c(k_F)$  curve), is well approximated by a  $T^8$  power law in the  $T$  regime in which some thick shell of neutrons is going through the phase transition. If we write

$$L_\nu^{\text{PBF}} = f \cdot L_\nu^{\text{MU}} = f N_9 T_9^8, \quad (64)$$

with  $f \sim 10$ , the solution of Eq. (58), replacing  $t_0$  by  $t_C$  and  $T_0$  by  $T_C$ , gives

$$T = \frac{T_C}{[1 + f(t - t_C)/t_C]^{1/6}} \rightarrow T_9 = \left( \frac{\tau_{\text{MU}}}{ft} \right)^{1/6} \quad (T \ll T_C). \quad (65)$$

Thus, at late times, the asymptotic “PBF trajectory” is a factor  $f^{-1/6} \simeq 0.7$  lower than the “MU trajectory” while the time-scale for the transit from the “MU trajectory” to the asymptotic “PBF trajectory”,  $T_9 = (\tau_{\text{MU}}/ft)^{1/6}$ , is  $\tau_{\text{TR}} = t_C/f$ . This behavior is shown schematically in the left panel of Fig. 30.

Since the initiation of the rapid transit, when the neutron star left the MU trajectory, must have occurred recently, i.e.  $t_C \simeq (0.5 - 0.9) \times 333$  yrs, we obtain

$$T_C = T_{cn}^{\max} = 10^9 \text{ K} (\tau_{\text{MU}}/t_C)^{1/6} \sim 5 \times 10^8 \text{ K}. \quad (66)$$

This is the first important result from this simple analytical model: given the observation of rapid cooling, the inferred value of  $T_C$  depends *only* on the known age,  $t = 333$  yrs, of this neutron star and the value of  $\tau_{\text{MU}} \sim 1$  year. This result is also in good agreement with the numerical models of Fig. 29. The 1/6 exponent in Eq. (66) confirms it to be a robust result without much dependence on microphysical details.

## 9.2 Superconducting Protons in the Core of Cas A

How “rapid” is the observed “rapid cooling” of the Cas A neutron star can be quantified by the observed slope

$$s_{\text{obs}} = \left| \frac{d \ln T_e^\infty}{d \ln t} \right| \simeq 1.4 \quad (67)$$

from the six data points reported in [152, 153]. This slope is much larger than the one of the “MU trajectory”,

$$s_{\text{MU}} = \left| \frac{d \ln T_e^\infty}{d \ln t} \right| = \frac{d \ln T_e^\infty}{d \ln T} \times \left| \frac{d \ln T}{d \ln t} \right| \simeq \frac{1}{2} \times \frac{1}{6} \simeq 0.08. \quad (68)$$

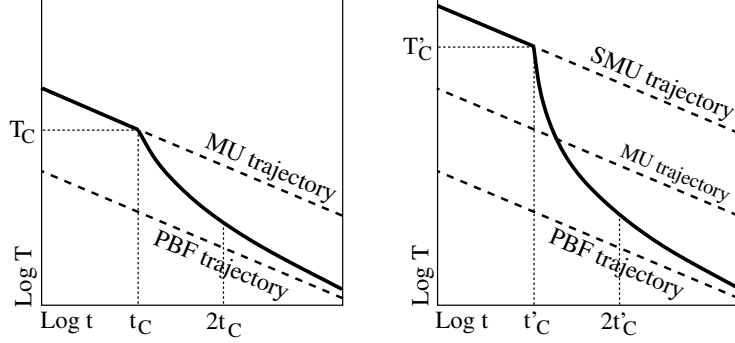


Figure 30: Schematic cooling trajectories (heavy curves) showing the effect of superconductivity. Left panel: Without superconductivity,  $T$  initially follows the modified Urca (MU) trajectory,  $T_9 = (\tau_{\text{MU}}/t)^{1/6}$  until  $T$  reaches the neutron critical temperature  $T_C$  at time  $t_C$ . The pair breaking and formation (PBF) process turns on and the neutrino luminosity  $L_\nu$  abruptly increases by a factor  $f$ . Thereafter,  $T$  rapidly transits, on a time scale  $\tau_{\text{TR}} = t_C/f$  toward the PBF trajectory,  $T_9 = (\tau_{\text{MU}}/ft)^{1/6}$ . Empirically, this transition takes a time  $\lesssim 2t_C$ . Right panel: When protons are superconducting, the initial evolution follows a superconducting-suppressed modified Urca (SMU) path. For the transit to start at a time  $t'_C \approx t_C$  the trajectory requires  $T'_C > T_C$ . The early transit has a shorter time scale,  $\tau'_{\text{TR}} = t'_C/f'$  with  $f' \gg f$ , and a significantly larger slope. The late time evolution converges to that of the left panel. The left (right) panel corresponds to models in Fig. 29 (Fig. 31 and 32). From [53].

In contrast, the “transit trajectory” of Eq. (65) gives a much larger slope

$$s_{\text{TR}} = \frac{1}{2} \times \frac{f}{6} \left( \frac{T}{T_C} \right)^6 \frac{t}{t_C}, \quad (69)$$

which has a maximum value  $f/12$ . Nevertheless, to match the observed slope  $s_{\text{obs}}$ ,  $f \gg 10$  is required.

The value of  $f$  considered above,  $f = L_\nu^{\text{PBF}}/L_\nu^{\text{MU}} \simeq 10$ , arose from a freely acting modified Urca neutrino emission. However, despite the many theoretical uncertainties discussed in Sec. 4, there seems little doubt that proton superconductivity exists around a few times  $\rho_{\text{nuc}}$ , as illustrated in Fig. 11. Moreover, expected values of  $T_{\text{cp}}^{\text{max}}$  are somewhat larger than  $10^9$  K, implying that protons were likely already superconducting in some part of the core of the Cas A neutron star when neutron anisotropic superfluidity set in. If such was the case, the previous neutrino luminosity of this star was due to a proton-pairing-suppressed modified Urca process with  $L_\nu^{\text{SMU}} < L_\nu^{\text{MU}}$ . This implies a much higher relative efficiency of the neutron PBF process, i.e.,  $f' = L_\nu^{\text{PBF}}/L_\nu^{\text{SMU}} \gg f \sim 10$ . The resulting transit from a “SMU trajectory” to the “PBF trajectory” is depicted in the right panel of Fig. 30 and exhibits a transit slope enhanced by a factor

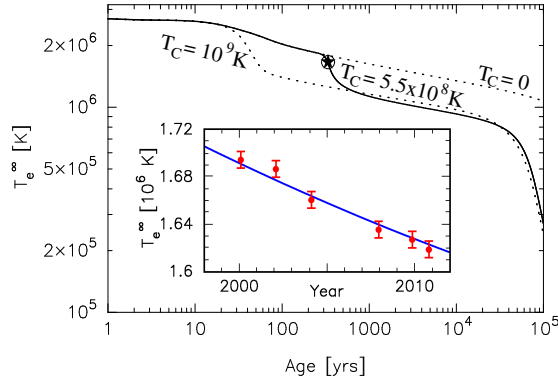


Figure 31: A fit to observations of the neutron star in Cas A assuming recent onset of neutron  ${}^3\text{P-F}_2$  superfluidity and PBF cooling. The  $1.4M_\odot$  model shown assumes the APR EOS [16] with a C atmosphere [151]. With model “CCDK” of Fig. 11 ( $T_{cp}^{\max} \gg 10^9 \text{ K}$ ), protons are superconducting from early times. The neutron  ${}^3\text{P-F}_2$  gap is model “a2” of Fig. 12 with  $T_C = T_{cn}^{\max} = 5.5 \times 10^8 \text{ K}$ . This neutron superfluid phase transition triggered the PBF process that results in a sudden cooling of the neutron star. Observations [152, 153] suggest  $|d \ln T_e^\infty / d \ln t| \simeq 1.4$ , shown in the inset. Two dotted curves with  $T_C = 0$  and  $1 \times 10^9 \text{ K}$ , respectively, illustrate the sensitivity to  $T_C$ . Figure adapted from [53].

$f'/f$ <sup>15</sup>.

With the above considerations, a very good fit to the observations can be obtained, as shown in Fig. 31, implying a maximum neutron  ${}^3\text{P-F}_2$  pairing  $T_C = 5.5 \times 10^8 \text{ K}$  along with superconducting protons with a larger  $T_{cp}^{\max}$ . Very similar results were independently obtained by [153]<sup>16</sup>. This observation of the cooling of the youngest known neutron star is unique and its interpretation potentially imposes very strong constraints on the physics of ultra-dense matter.

The requirement that protons became superconducting before the onset of neutron superfluidity places a constraint not only on the proton  ${}^1\text{S}_0$  pairing but also on the neutron star mass. If the neutron star mass is not too large, models show that proton superconductivity does not extend to very high densities.

<sup>15</sup>Presumably, at the time of the onset of proton superconductivity, another PBF episode had occurred, but, as the PBF process for singlet pairing is much less efficient than for triplet pairing, and also because protons are much less abundant than neutrons, it did not result in a significant cooling of the star. Moreover, this cooling occurred on timescales much smaller than the crustal thermal timescale.

<sup>16</sup> These authors, however, assumed that proton superconductivity extends to very high densities, with  $T_{cp} \gtrsim (2-3) \times 10^9 \text{ K}$  in the whole neutron star core. This results in a very strong suppression of  $L_\nu$  prior to the onset of neutron  ${}^3\text{P-F}_2$  superfluidity, and a neutron star much warmer than in the model of [53], from which a larger  $T_{cn}^{\max} \simeq (6-9) \times 10^8 \text{ K}$  is deduced. However, strong proton superconductivity at high densities is, at present time, not supported by the microscopic models presented in Fig. 11.



Fig. 32 illustrates the sensitivity to the neutron star mass. A better understanding of the progenitor of Cas A and its expected neutron star mass will prove important in validating this scenario.

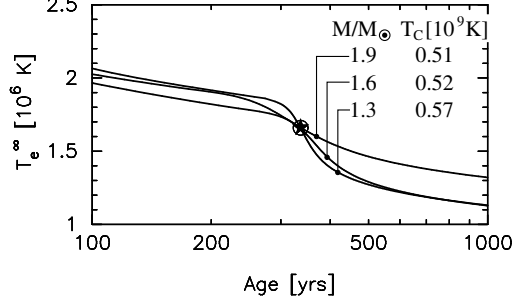


Figure 32: Dependence of the slope  $s = |d \ln T_e^\infty / d \ln t|$  of the cooling curve on the star mass at  $t = 330$  years:  $s = 1.4, 0.9$ , and  $0.5$  for  $M = 1.3, 1.6$ , and  $1.9 M_\odot$ , respectively (from [53]).

The neutron superfluid explanation for the rapid cooling of the neutron star in Cas A fits well within the *minimal cooling* scenario [51, 52]. As described in Sec. 8.2, maximal compatibility of the minimal cooling scenario [52] with data required the neutron  $^3\text{P-F}_2$  gap to have  $T_{cn}^{\max} \gtrsim 5 \times 10^8$ . This lower limit on  $T_{cn}^{\max}$  was deduced for compatibility with the measured  $T_e$  of the youngest neutron stars of age  $\sim 10^3$  yrs. The upper limit on  $T_{cn}^{\min}$  was deduced for compatibility with the oldest middle-aged stars as, e.g., the Vela pulsar. The compatibility of the neutron  $^3\text{P-F}_2$  gap inferred from the cooling data of the neutron star in Cas A with observations of other isolated neutron stars is confirmed in Fig. 33. The only marked difference between Fig. 33 and the left panel of Fig. 26 is the occurrence of the rapid cooling phase at ages  $\simeq 300$  yrs to  $\sim 500$  yrs, due to the reduced value of  $T_{cn}^{\max}$  in the former,  $0.55 \times 10^9$  K compared to  $1.0 \times 10^9$  K.

### 9.3 Alternative Scenarios

Alternative explanations for the observed rapid cooling of Cas A have been proposed. One could consider observed cooling of this star to be due to a significantly longer thermal relaxation timescale in the crust or core than assumed in [53, 153]. In such a case, the estimate of Eq. (63), which assumes the star to be isothermal, becomes invalid. In all models shown in this chapter, the crust thermal relaxation occurs on a timescale of a few decades. However, if the crust thermal conductivity is, in fact, significantly smaller, it is conceivable that the observed rapid cooling corresponds to the thermal relaxation of the crust (see, e.g., [154]). Such a low crust thermal conductivity is, however, in conflict with the observed crust relaxation time in transiently accreting neutron stars [155, 156] and is based on the assumption that the crust is in an amorphous

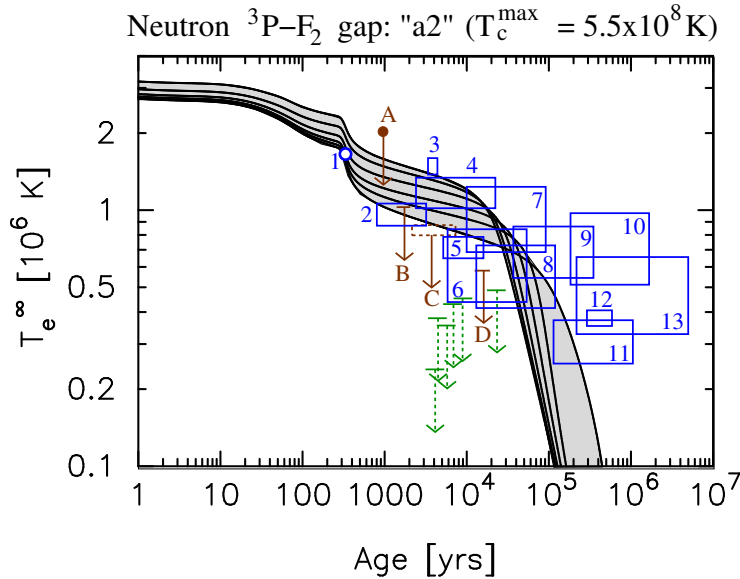


Figure 33: Comparison of the cooling scenario of Fig. 31 with data for isolated neutron stars. As in Fig. 26, the various lines show the effect of varying the amount of light elements in the envelope (from [126]).

solid state instead of a crystalline one, a possibility that is not supported by microscopic studies [157, 158].

Similarly, the core thermal relaxation time may be much larger than usually considered. For example, Blaschke et al. [159] have proposed that the inner core of the star cools rapidly and that it also takes a few hundreds years for the star to become isothermal. The latter time is when the rapid decrease of  $T_e^\infty$  would be observed. This scenario requires that the core thermal conductivity be lower than usually considered, by a factor 4 or larger, and also requires that neutrons *do not* form a superfluid until the star is much colder. This scenario, based on the “Medium-Modified Urca” neutrino emission process [72, 104], is also compatible with the cooling data, but only if the suppression of core conductivity is adjusted to fit the observed cooling of the neutron star in Cas A.

More work is required to confront these alternative possibilities with other facets of neutron star phenomenology.

## 10 Dynamical Evolution of Neutron Stars

Pulsars are rotating neutron stars whose spin rates are generally observed to be decreasing. The regularity of pulsars is outstanding; as timekeepers they rival atomic clocks. Although the pulses are remarkably regular, the time between pulses slowly but predictably increases. Their spin-downs are attributed to magnetic dipole radiation [160, 161] – the conversion of rotational energy

into electromagnetic energy – and the pulsar wind from ejection of the magnetospheric plasma [162]. That the observed evolution of pulsar spins exhibits evidence for both core and crustal superfluidity is the subject of this section.

## 10.1 Magnetic Dipole Pulsar Model

Dimensional analysis gives us a simple estimate of the pulsar energy losses. Energy and angular momentum are irreversibly lost when either the magnetic field or the plasma reaches the *light cylinder* where co-rotation with the pulsar implies a speed equal to  $c$  and whose radius is thus  $R_{lc} = c/\Omega \simeq 50(P/1 \text{ msec})$  km,  $\Omega$  being the spin rate and  $P = 2\pi/\Omega$  the spin period. The magnetic field at the light cylinder is  $B_{lc} = (R/R_{lc})^3 B_s$  assuming a dipolar field with a strength  $B_s$  at the stellar surface. Just writing that an energy density  $B_{lc}^2/4\pi$  is lost at the speed of light  $c$  from a sphere of area  $4\pi R_{lc}^2$ , one obtains

$$\dot{E}_{PSR} \simeq \frac{1}{c^3} (R^3 B_s)^2 \Omega^4. \quad (70)$$

Energy loss by *in vacuum* magneto-dipolar radiation gives the same result with just an extra factor  $(2/3)\sin^2\alpha$ ,  $\alpha$  being the angle between the rotationnal axis and the dipolar moment. An aligned rotator, i.e. with  $\alpha = 0$ , will not spin-down from magneto-dipolar radiation but rather by plasma ejection [162]. Numerical and consistent calculations of the energy loss from the ejected magnetospheric plasma have been possible only recently ([163] and [164] for a review) and the result is that the total  $\dot{E}_{PSR}$  is given by Eq. (70) with an extra factor  $\simeq (1 + \sin^2\alpha)$ . Considering the rotational energy of a uniformly rotating sphere  $E_{rot} = I\Omega^2/2$ , where  $I$  is the star's moment of inertia, the pulsar's spin-down is determined by equating  $\dot{E}_{rot}$  with  $-\dot{E}_{PSR}$ , giving

$$\dot{\Omega} = -\frac{K}{I} \Omega^3 \quad (71)$$

with  $K \simeq R^6 B_s^2/c^3$ , assuming that  $I$  and  $B_s$  remain constant. This also provides an estimate of  $B_s$ , probably reliable within a factor of a few,

$$B_s \simeq \sqrt{\frac{-c^3 \dot{\Omega}}{\Omega^3 I R^6}} \simeq 3.2 \times 10^{19} (P \dot{P})^{1/2} \text{ G} \simeq 1.5 \times 10^{12} \frac{P}{0.01 \text{ s}} \left( \frac{1000 \text{ yr}}{\tau_c} \right)^{1/2} \text{ G}, \quad (72)$$

we assumed  $M \simeq 1.4 M_\odot$  and  $R \simeq 12$  km. It is traditional to also deduce an observable characteristic pulsar age

$$\tau_c = -\frac{\Omega}{2\dot{\Omega}} \quad (73)$$

and an observable braking index

$$n \equiv \frac{\Omega \ddot{\Omega}}{\dot{\Omega}^2} \quad (74)$$

In the case of the magnetic dipole model and assuming both  $I$  and  $B_s$  are constant,  $n = 3$ .

The ATFN catalogue<sup>17</sup> [165] lists 1759 pulsars (as of December 2012) with measured values of  $\dot{P}$ . The measurement of a second derivative  $\ddot{\Omega}$ , allowing the determination of  $n$ , requires a very accurate long term and smooth fit of  $\dot{\Omega}$  and is much more difficult due in part to timing noise and to glitches. To date, there are only 11 published values of  $n$  [166], all with values less than 3 and ranging from  $-1.5$  to  $+2.91$  (see Table 10.2). Anomalous values  $n < 3$  may be due to a growing magnetic field [167] and/or to a growing fraction of the star's core becoming superfluid [168]. The latter could be due to the onset and growth of  $^1\text{S}_0$  p and  $^3\text{P-F}_2$  n components (further evidence for this stems from observations of the cooling of the neutron star in the Cassiopeia A supernova remnant, which is discussed in Sec. 9).

## 10.2 Anomalous Braking Indices

Consider the evolution of the spin of a pulsar if we allow changes in the surface field  $B_s$  and the moment of inertia  $I$ . Assume the star has both normal matter and superfluid matter with moments of inertia  $I_n$  and  $I_s$ , respectively. Although the onset of superfluidity is unlikely to significantly change the total moment of inertia, the portion of the star that is superfluid may be considered to spin frictionlessly and its spin rate  $\Omega_s$  to remain constant. The observed spin rate of the star is that of the star's surface, which is composed of normal matter. We therefore have

$$I = I_n + I_s, \quad \dot{I} = 0, \quad \Omega_n = \Omega, \quad \dot{\Omega}_s = 0. \quad (75)$$

With these two components, the rate of change of angular momentum in the magnetic dipole model is

$$\frac{d}{dt} [I_n \Omega_n + I_s \Omega_s] = I_n \dot{\Omega} + \dot{I}_n (\Omega - \Omega_s) = -K \Omega^3. \quad (76)$$

Taking a time derivative of the above, one finds

$$n = 3 + 4\tau_c \left[ \frac{\dot{I}_n}{I_n} - \frac{\dot{B}_s}{B_s} \right] + \tau_c \left( \frac{\Omega_s}{\Omega} - 1 \right) \frac{\dot{I}_n}{I_n} \left[ 6 + 4\tau_c \left( \frac{\ddot{I}_n}{\dot{I}_n} - 2 \frac{\dot{B}_s}{B_s} \right) \right]. \quad (77)$$

Since  $\Omega_s - \Omega \ll \Omega$ , we can drop the last term in Eq. (77). Thus, the growth of either the surface magnetic field and/or the superfluid component leads to  $n < 3$ . In fact, the growth of a core superfluid component could lead to field ejection from the core and an increase in the surface field strength. Note that there has been a long history of study of the opposite possibility of *decay* of pulsar magnetic fields. However, statistical studies of the pulsar population [169] no longer support this idea and the present consensus is that magnetic

<sup>17</sup>On-line version: <http://www.atnf.csiro.au/research/pulsar/psrcat/>

Pulsar (SNR)	$P$ s	$\tau_c$ kyr	$B_s$ $10^{12}$ G	$n$	$\mathcal{A}$ $10^{-9}/\text{d}$	$2\tau_c\mathcal{A}$ %
B0531+21 (Crab)	0.0331	1.24	3.78	2.5		
J0537-6910 (N157B)	0.0161	4.93	0.925	-1.5	2.40	0.9
B0540-69 (0540-693)	0.0505	1.67	4.98	2.1		
J0631+1036	0.2878	43.6	5.55		0.48	1.5
B0833-45 (Vela)	0.0893	11.3	3.38	1.7	1.91	1.6
J1119-6127 (G292.2-0.5)	0.4080	1.61	41	2.9		
B1338-62 (G308.8-0.1)	0.1933	12.1	7.08		1.31	1.2
B1509-58 (G320.4-1.2)	0.1513	1.56	15.4	2.8		
J1734-3333	1.1693	8.13	52.2	0.9		
B1737-30	0.6069	20.6	17		0.79	1.2
J1747-2958	0.0988	25.5	2.49	< 1.3		
B1757-24 (G5.4-1.2)	0.1249	15.5	4.04	-1	1.35	1.5
B1758-23 (W28?)	0.4158	58.3	6.93		0.24	1.0
B1800-21 (G8.7-0.1(?))	0.1367	15.8	4.29	2	1.57	1.8
B1823-13	0.1015	21.4	2.8	2	0.78	1.2
J1846-0258 (Kes75)	0.3266	0.728	48.8	2.6		
B1930+22	0.1445	39.8	2.92		0.95	2.8
B2229+6114 (G106.6+2.9)	0.0516	10.5	2.03		0.63	0.5

Table 2: Observed pulsar properties (“SNR” is the associated supernova remnant). Values of spin period  $P$ , characteristic age  $\tau_c$  [Eq. (73)] and dipole surface field strength  $B_s$  [Eq. (72)] rounded from the ATFN catalogue [165]. Values of the braking index  $n$  [Eq. (74)] rounded from [166]. Values of  $\mathcal{A}$  [Eq. (79)] taken from [176].

field decay is significant only in the case of super-strong fields as in magnetars or after a long phase of accretion in a binary system.

Nevertheless, observed values  $n < 3$  do not prove that superfluidity exists. The growth of the surface field of a pulsar can be obtained in the case that the initial magnetic field was partially buried, e.g., by post-supernova hypercritical accretion [170, 171, 172], into the stellar interior and is now slowly diffusing outwards [167]. Detailed numerical models show that observed values of  $n$  can be reproduced [173] without invoking superfluidity. Alternatively, magnetospheric currents may deform the field into a non-dipolar geometry [174, 175] that results in  $n < 3$  (but  $n \ll 3$  is unreachable in these models and  $n < 0$  is impossible). The truth may be a superposition of these three types of arguments:  $\dot{I}_n < 0$ ,  $\dot{B}_s > 0$ , and non-dipolar fields.

### 10.3 Glitches

The second indication of superfluidity in neutron stars stems from the fact that many pulsars exhibit sporadic spin jumps, or glitches (see Fig. 34). The Jodrell

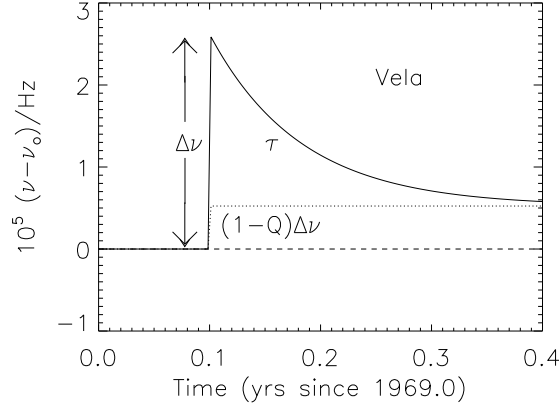


Figure 34: Schematic illustration of a Vela pulsar glitch. The observed pulsar spin frequency  $\nu$  has been corrected by the average accumulated spindown since 1969.0 ( $\nu_o = \dot{\nu}(t - 1969.0)$ ) to make the glitch easier to discern. The glitch is observed as a relatively sudden jump  $\Delta\nu$  in spin frequency. The frequency afterwards relaxes roughly exponentially on a timescale  $\tau$  to a new spindown line (dotted) which has a higher average frequency  $(1-Q)\Delta\nu$  than the pre-glitch spindown line  $\nu = \nu_o$  (dashed).

Bank glitch catalogue<sup>18</sup> lists 420 glitches (as of December 2012) [177]. These are thought to represent angular momentum transfer between the crust and a liquid, possibly superfluid, interior [178, 179, 180]. As the star's crust spins down under the influence of magnetic torque, differential rotation develops between the crust (and whatever other parts of the star are tightly coupled to it) and a different portion of the interior containing a superfluid (recall in the above that  $\dot{\Omega}_s = 0$ ), but possibly a superfluid component different from those in the core. The now more rapidly rotating (superfluid) component then acts as an angular momentum reservoir which exerts a spin-up torque on the crust as a result of an instability. The Vela pulsar, one of the most active glitching pulsars, glitches about every 3 years, with a fractional change in the rotation rate averaging a part in a million [181, 182], as shown in Fig. 35.

The stochastic nature of glitches implies that they represent a self-regulating instability for which the star prepares over a waiting interval. The amount of angular momentum transferred is observed to increase linearly with time, as shown in Fig. 35 for Vela and for the X-ray pulsar J0537-6910. Assume that the moment of inertia of the superfluid component responsible for glitches is  $I_g$  and that of the crust and whatever parts of the star are tightly coupled to it is  $I_c$ . In an individual glitch  $i$ , an amount of angular momentum  $I_c\Delta\Omega_i$  is transferred

<sup>18</sup>On-line version: <http://www.jb.man.ac.uk/pulsar/glitches.html>

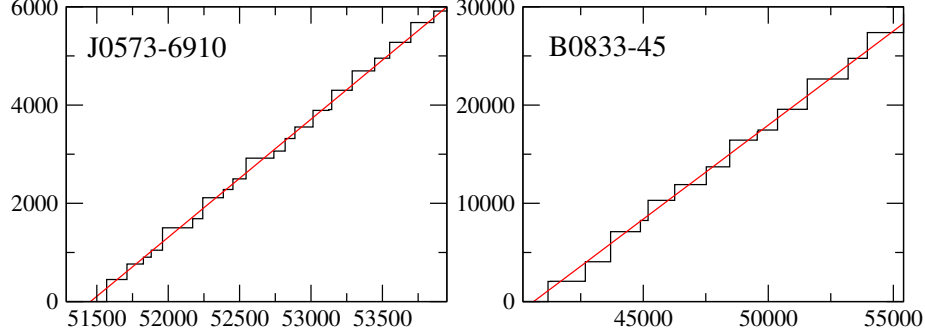


Figure 35: The accumulated relative angular velocity  $10^{-9} \sum_i \Delta\Omega_i/\Omega$  as a function of time in days for the X-ray pulsar J0537-6910 and for Vela (B0833-45).  $\Delta\Omega_i$  is the change in angular velocity of a single glitch. Linear fits are indicated, with respective slopes [ Eq. (79)]  $\mathcal{A} = 2.4 \times 10^{-9} \text{ d}^{-1}$  and  $1.91 \times 10^{-9} \text{ d}^{-1}$ . (From [176])

to the crust, where  $\Delta\Omega_i$  is the observed jump in angular velocity. Over the interval  $t_i$  between the last glitch and the current glitch, the star spins down by the amount  $\Delta\Omega = -\dot{\Omega}t_i$  and the total angular momentum differentially stored in the superfluid component is  $I_g\Delta\Omega$ . These two angular momenta are equal, and over a total observed time  $t_{obs} = \sum_i t_i$ , we have

$$I_g \gtrsim 2\tau_c \mathcal{A} I_c, \quad (78)$$

where the observed quantity  $\mathcal{A}$  is related to the accumulated jumps,

$$\mathcal{A} = \left( \sum_i \Delta\Omega_i/\Omega \right) t_{obs}^{-1}. \quad (79)$$

In the case of the Vela pulsar, the magnitude of  $\mathcal{A}$  implies that  $I_g/I_c = 2\tau_c \mathcal{A} \gtrsim 0.016$ [183]. Minimum values for this ratio for other pulsars are given in the last column of Table 10.2.

Since the moment of inertia in the inner crust (with the n  $^1\text{S}_0$  type superfluid) is  $I_{sc}$  and satisfies

$$I_{sc} \simeq 0.04I, \quad (80)$$

where  $I$  is the star's total moment of inertia, glitches can be naturally explained by the inner-crust superfluid since  $I_g \lesssim I_{sc}$ . Although the magnitudes of individual glitches varies somewhat, the maximum-sized glitches have stable and limited sizes. This would be difficult to explain if glitches originated from the inner core's superfluid component, whose associated moment of inertia is a much larger fraction of the star's total.

Recently it has been shown that most of the neutron mass of the dripped neutrons in the inner crust is entrained by Bragg scattering with the nuclear

lattice, effectively increasing the neutron mass by factors of 4–5 [184, 178]. With this entrainment, Eq. (78) becomes, for Vela,

$$I_g \gtrsim 0.08 I_c, \quad (81)$$

precluding an inner crust superfluid explanation for  $I_g$  if  $I_c \simeq I$ . Entrainment results in most of the neutron fluid spinning down with the crust, and the unentrained conduction neutrons cannot accumulate angular momentum at a high-enough rate to produce the largest observed glitches [185].

B. Link [185] has pointed out, however, that  $I_c$  is likely to be smaller than  $I$ , perhaps considerably so, if the outer core decouples from the crust over timescales of weeks to years. In fact, this is the observed timescale  $\tau$  of the post-glitch relaxation (see Fig. 34), which may simply represent the dynamical recovery of the outer core. For older pulsars, which are cooler, the relaxation timescale is long, of the order of years, and this could explain the nearly step-like behavior of many pulsar glitches. As a consequence, for example, if  $I_c \simeq I/2$ , Eq. (81) and (80) regain consistency. The upshot is that spin glitches could then originate in either the inner crust or the outer core. The observed limited maximum magnitude of glitches retains its natural explanation in terms of the small and regular sizes of neutron star crusts as opposed to the wider variations in sizes of core superfluid regions.

It should be noted that the above is at odds with the results of Sidery and Alpar [186], who obtain relaxation times of only about 2 days. This discrepancy is the subject of ongoing discussions.

## 11 Discussion and Conclusions

In this chapter, the influence of pairing, leading to neutron superfluidity and proton (and quark) superconductivity, on key observables of neutron stars is described. The observables include aspects of their thermal evolution, composed of surface temperatures, cooling rates, and ages, and dynamical evolution, comprised of pulsar spin-down characteristics and glitch information. The major effects of pairing on the thermal evolution of an isolated neutron star are the quenching of neutrino emissions and the reduction of specific heat of the paired fermions, be they nucleons, hyperons or deconfined quarks, in their cores. However, the onset of pairing also triggers short episodes of increased neutrino emission through pair breaking and formation (PBF) processes when the ambient temperature falls below the superfluid critical temperature. The PBF emission of neutrino pairs through weak interactions of strongly interacting particles is unique to dense neutron-star matter, as a similar phenomenon does not occur in nuclei for  $^1S_0$  paired fermions as it is forbidden on the basis of symmetry. The major effects of pairing on dynamical evolution include the reduction of the so-called braking index, a measure of spin deceleration, of pulsars, and the possible triggering of glitches from weak coupling of superfluid vortices to neutron star crusts.



The sizes and density dependences of superfluid and superconducting gaps play a crucial role. Pairing is observed in nuclei as an energy difference between even-even and odd-even nuclei with a typical magnitude, ranging from 0.5 to 3 MeV, that decreases with atomic number. The basic cause of pairing in nuclei is due to the attractive interaction between neutrons in the spin  $S = 0$  channel. Gaps of similar magnitude for nucleon pairing in neutron stars are expected. Both spin-singlet  $^1S_0$  (at lower densities) and spin-triplet  $^3P_2$  (at higher densities) configurations appear possible from scattering phase shifts arguments. Pairing appears as a gap  $\Delta$  in the single particle energy spectrum, leading to a strong suppression ( $\sim e^{-2\Delta/T}$ ) of both specific heat and neutrino emissivities at low temperatures. In the simple BCS approximation, however, the gap depends exponentially on the pairing potential. Hence, uncertainties associated with in-medium effects of strong-interactions at high density have prevented a consensus about the sizes and density dependences of gaps from being reached. In addition, the nature and abundance of possible candidates for pairing (nucleons and strangeness-bearing hyperons, quarks, Bose condensates) are also uncertain.

In the neutron star crust, the density of unbound neutrons is high enough that  $^1S_0$  pairing is expected to occur. Most theoretical models suggest that the associated gap disappears at neutron densities higher than that of the core-crust interface, so it is confined to the crust. The latest calculations indicate a maximum gap magnitude of about  $1.5 \times 10^{10}$  K. Since proton-neutron correlations reduce the effective mass of the proton below that of the neutron, the size of the proton  $^1S_0$  gap is smaller than that of the neutron. “Unbound” protons exist only at densities greater than  $\rho_{\text{nuc}}$  where nuclei disappear, so proton superconductivity in the spin-singlet state is expected to exist from the core-crust boundary to deep into the core once temperatures fall below a few times  $10^9$  K. The  $^1S_0$  neutron gap vanishes close to the core-crust interface and the dominant pairing for neutrons in the core occurs in the anisotropic  $^3P\text{-}F_2$  channel. Uncertainties in the size and density range for this gap are larger than for  $^1S_0$  gaps, however, with maximum magnitudes ranging from a few times  $10^7$  K to a few times  $10^9$  K.

The greatest influence of pairing will be on the thermal evolution of neutron stars. The occurrence of pairing leads to three important effects for neutron star cooling: alteration and eventual suppression of nucleon specific heats, suppression of neutrino emissivities, and triggering of PBF neutrino emission for temperatures just below the critical temperature. Presently, 13 isolated neutron stars with thermal spectra in the soft X-ray band have been identified. In addition, there are four pulsars with detected X-rays but with only upper limits to thermal emission. Finally, there are six gravitational-collapse supernova remnants that might contain neutron stars (if not, then black holes), but no detected thermal emission as yet. Atmospheric modeling of the thermal sources yields estimates of surface temperatures, and together with age estimates, allows these stars to be compared to theoretical cooling models. Most observed sources are younger than a million years, during which time they cool primarily through neutrino emission.

Neutrino cooling can be either very fast (i.e., *enhanced*), or relatively slow. Enhanced cooling occurs by way of the direct Urca process on nucleons, hyperons, Bose condensates, or deconfined quark matter. It is allowed when energy and momentum can be conserved with 3 or fewer degenerate fermions involved. If additional “bystander” nucleons are required to conserve momentum, neutrino emission is suppressed by about a factor of a million. If pairing is not present and enhanced neutrino emission does not occur, it is found that several observed neutron stars are too cold to match cooling models. Therefore, an important first conclusion is that *either pairing or enhanced neutrino emission must occur in some neutron stars*. On the other hand, if pairing is not present and enhanced neutrino emission does occur, *all* observed neutron stars are too hot to match cooling models. Thus, a second conclusion is that *in the presence of enhanced cooling, superfluidity and/or superconductivity must occur*. However, as there are many combinations of pairing gap sizes and extents, neutron star masses and envelope compositions, and enhanced cooling candidates that can match observations, it is not possible to determine either gap properties or the specific enhanced cooling reactions involved. Therefore, for example, neutron star cooling cannot lead to an unambiguous detection of hyperons, Bose condensates or deconfined quark matter in the interior of neutron stars at this time.

A final scenario, known as the *minimal cooling paradigm*, assumes enhanced neutrino emission does not occur, but allows pairing. In this case, *all* observed stars, with the possible exception of the pulsar in the supernova remnant CTA 1, for which only an upper temperature limit is available, and the six undetected neutron stars in gravitational-collapse supernova remnants, none of which is certain to be a neutron star at all, can be fit by theoretical cooling models. However, fitting observations *requires* two constraints on neutron stars:

- The neutron  ${}^3\text{P-F}_2$  gap must have a maximum critical temperature  $T_{cn}^{\text{max}}$  larger than  $\sim 0.5 \times 10^9$  K, but unlikely larger than  $1.5 - 2 \times 10^9$  K; and
- some, but not all, neutron stars must have envelopes composed of light elements (H/He/C) and some, but not all, must have envelopes composed of heavy elements.

The assumed mass of a neutron star has only a minor influence on the results of the minimal cooling scenario. The source CTA 1 and some of the undetected neutron stars in gravitational-collapse supernova remnants might then be candidates for enhanced neutrino emission via the direct Urca process. One obvious way in which this could occur is that, since there is a density threshold for the onset of the direct Urca process, only neutron stars above a critical mass could participate. From observed and theoretically-predicted neutron star mass distributions, this critical mass is estimated to be in the range  $1.6 - 1.8M_{\odot}$ . This result is itself supported by recent experimental and observational restrictions on how fast the symmetry energy of nuclear matter can increase with density [140], which suggest that the nucleon direct Urca threshold density is much greater than  $\rho_{\text{nuc}}$ .

The recently detected rapid cooling of the neutron star in Cas A provides an unprecedented opportunity to overcome the dilemma of deciding whether “exotica” are needed, or if the minimal cooling paradigm is sufficient, to account for observational cooling data. The rapidity of the stellar cooling in Cas A remnant points to both the onset of core neutron superfluidity within the last few decades and the prior existence of core proton superconductivity with a larger critical temperature. The PBF process, with its time-dependent burst of neutrinos at the critical temperature, is central to the success of model calculations fitting both Cas A cooling observations and the entire body of data for other observed isolated neutron stars. Furthermore, the Cas A cooling observations can be fit only if  $T_{cn}^{\max} \simeq 5 - 6 \times 10^8$  K, *precisely in the range independently found* for the minimal cooling scenario based on other isolated neutron star cooling data. Sherlock Holmes would not have deemed this a coincidence. “Enhanced” processes appear to be ruled out in the case of Cas A, as its star would presently be too cold. Further observations of the cooling of the neutron star in Cas A can confirm these conclusions.

Final indications of the existence of pairing in neutron stars is afforded by observations of the deceleration of the spin frequency and glitches of pulsars. The standard paradigm to explain the pulsar mechanism is based on the magnetic rotating dipole model, for which it can be shown that the spin-down parameter  $n = -\Omega\ddot{\Omega}/\dot{\Omega}^2 = 3$ . All non-accreting pulsars for which  $n$  has been determined have  $n < 3$ , which can be understood either if the surface dipolar magnetic field is increasing in strength or if there is a growing superfluid or superconducting component within the neutron star’s core. An increasing surface field could, in fact, be due to the expulsion of magnetic flux from the core by superconductors. The leading model for pulsar glitches is that a more-rapidly rotating, and essentially frictionless, superfluid in the crust sporadically transfers angular momentum to the more slowly-rotating crust and the parts of the star strongly coupled to it.

In conclusion, there is abundant evidence that the ultimate “high-temperature” superfluid (or superconductor) exists in nearly every neutron star. Unmistakably, superfluidity and superconductivity exhibited by the constituents of neutron stars provide avenues by which the observed cooling behaviors of these stars can be explained. Theoretical predictions of pairing gaps being as yet uncertain, astronomical data are pointing to a path forward in their determinations. A remarkable recent development is that, despite the nearly three-order-of-magnitude theoretical uncertainty in the size of the neutron  ${}^3\text{P-F}_2$  gap, and the factor of 3 uncertainty in the size of the proton  ${}^1\text{S}_0$  gap, observations of the neutron star in Cas A now appear to restrict their magnitudes to remarkably small ranges. It will be interesting to see if these considerable restrictions translate into a more complete understanding of the pairing interaction between nucleons and provide insights into other aspects of condensed matter and nuclear physics. Continued X-ray observations of this star and other isolated sources, and, hopefully, the discovery of additional cooling neutron stars, will further enhance these efforts.

## Acknowledgments

DP acknowledges support by grants from UNAM-DGAPA, # PAPIIT-113211, and Conacyt, CB-2009-01, #132400. MP, JML and AWS acknowledge research support from the U.S. DOE grants DE-FG02-93ER-40746, DE-AC02-87ER40317 and DE-FG02-00ER41132, respectively, and by the DOE Topical Collaboration “Neutrinos and Nucleosynthesis in Hot and Dense Matter”, contract #DE-SC0004955.

## References

- [1] L. N. Cooper. Bound Electron Pairs in a Degenerate Fermi Gas. *Phys. Rev.* **104**:1189, 1956.
- [2] J. Bardeen, L. N. Cooper, and J. R. Schrieffer. Theory of Superconductivity. *Phys. Rev.* **108**:1175, 1957.
- [3] A. Bohr, B. R. Mottelson, and D. Pines. Possible Analogy between the Excitation Spectra of Nuclei and Those of the Superconducting Metallic State. *Phys. Rev.* **110**:936, 1958.
- [4] E. Segrè. *Nuclei and Particles*. W. A. Benjamin, 1965.
- [5] L. M. Robledo and G. F. Bertsch. Pairing in finite systems: beyond the HFB theory. In *50 Years of Nuclear BCS: Pairing in Finite Systems*, R. A. Broglia and V. Zelevinsky, editors. World Scientific, 2013. [arXiv:1205.4443].
- [6] D. M. Brink and R. A. Broglia. *Nuclear Superfluidity: pairing in finite systems*. Cambridge University Press, 2005.
- [7] R. A. Broglia and V. Zelevinsky. *50 Years of Nuclear BCS: Pairing in Finite Systems*. World Scientific, 2013.
- [8] A. Migdal. Superfluidity and the moments of inertia of nuclei. *Nucl. Phys. A* **13**:655, 1959.
- [9] W. Baade and F. Zwicky. Cosmic rays from super-novae. *Proc. Nat. Acad. Sci.* **20**:259, 1934.
- [10] S. E. Woosley, A. Heger, and T. A. Weaver. The evolution and explosion of massive stars. *Rev. Mod. Phys.* **74**:1015, 2002.
- [11] J. W. T. Hessels, S. M. Ransom, I. H. Stairs, P. C. C. Freire, V. M. Kaspi, and F. Camilo. A Radio Pulsar Spinning at 716 Hz. *Science* **311**:1901, 2006.
- [12] J. M. Lattimer and M. Prakash. Ultimate Energy Density of Observable Cold Baryonic Matter. *Phys. Rev. Lett.* **94**(11):111101, 2005.

- [13] J. R. Oppenheimer and G. M. Volkoff. On Massive Neutron Cores. *Phys. Rev.* **55**:374, 1939.
- [14] A. Burrows and J. M. Lattimer. The birth of neutron stars. *Astrophys. J.* **307**:178, 1986.
- [15] D. Page and S. Reddy. Dense Matter in Compact Stars: Theoretical Developments and Observational Constraints. *Annu. Rev. Nucl. & Part. Sci.* **56**:327, 2006.
- [16] A. Akmal, V. R. Pandharipande, and D. G. Ravenhall. Equation of state of nucleon matter and neutron star structure. *Phys. Rev. C* **58**:1804, September 1998.
- [17] D. Lai. Matter in strong magnetic fields. *Rev. Mod. Phys.* **73**:629, 2001.
- [18] D. R. Tilley and J. Tilley. *Superfluidity & Superconductivity*. Graduate Student Series in Physics. Institute of Physics Publishing, 1990.
- [19] C. J. Pethick and A. Y. Potekhin. Liquid crystals in the mantles of neutron stars. *Phys. Lett. B* **427**:7, 1998.
- [20] C. A. Bertulani and J. Piekarewicz. *Neutron Star Crust*. Nova Publisher, 2012.
- [21] R. Tamagaki. Superfluid state in neutron star matter. I. Generalized Bogoliubov transformation and existence of  $^3\text{P}_2$  gap at high density. *Prog. Theor. Phys.* **44**:905, 1970.
- [22] L. P. Gorkov and T. K. Melik-Barkhudarov. Contribution to the Theory of Superfluidity in an Imperfect Fermi Gas. *Sov. Phys. JETP* **13**:1018, 1961.
- [23] U. Lombardo and H.-J. Schulze. Superfluidity in Neutron Star Matter. In *Physics of Neutron Star Interiors*, D. Blaschke, N. K. Glendenning, & A. Sedrakian, editors, vol. 578 of *Lecture Notes in Physics*, Springer Verlag, page 30, 2001. [arXiv:astro-ph/0012209].
- [24] D. J. Dean and M. Hjorth-Jensen. Pairing in nuclear systems: from neutron stars to finite nuclei. *Rev. Mod. Phys.* **75**:607, 2003.
- [25] A. Sedrakian and J. W. Clark. Nuclear Superconductivity in Compact Stars: BCS Theory and Beyond. In *Pairing in Fermionic Systems: Basic Concepts and Modern Applications*, A. Sedrakian, J. W. Clark, and M. Alford, editors, page 135. World Scientific, 2006. [arXiv:nucl-th/0607028].
- [26] A. A. Abrikosov, L. P. Gorkov, and Dzyaloshinski I. E. *Methods of Quantum Field Theory in Statistical Physics*. Dover Publications, 1963.

- [27] L. D. Landau, E. M. Lifshitz, and L. P. Pitaevskii. *Statistical Physics: Theory of the Condensed State. (Vol. 9 of Course of Theoretical Physics)*. Butterworth-Heinemann, 1980.
- [28] T. Takatsuka. Superfluid state in neutron star matter. III. Tensor coupling effect in  $^3P_2$  energy gap. *Prog. Theor. Phys.* **47**:1062, 1972.
- [29] L. Amundsen and E. Østgaard. Superfluidity of neutron matter (II). Triplet pairing. *Nucl. Phys. A* **442**:163, 1985.
- [30] M. Baldo, J. Cugnon, A. Lejeune, and U. Lombardo. Proton and neutron superfluidity in neutron star matter. *Nucl. Phys. A* **536**:349, 1992.
- [31] K. P. Levenfish and D. G. Yakovlev. Specific heat of neutron star cores with superfluid nucleons. *Astron. Rep.* **38**:247, 1994.
- [32] H.-J. Schulze, J. Cugnon, A. Lejeune, M. Baldo, and U. Lombardo. Medium polarization effects on neutron matter superfluidity. *Phys. Lett. B* **375**:1, 1996.
- [33] J. M. C. Chen, J. W. Clark, R. D. Davé, and V. V. Khodel. Pairing gaps in nucleonic superfluids. *Nucl. Phys. A* **555**:59, 1993.
- [34] J. Wambach, T. L. Ainsworth, and D. Pines. Quasiparticle interactions in neutron matter for applications in neutron stars. *Nucl. Phys. A* **555**:128, 1993.
- [35] A. Schwenk, B. Friman, and G. E. Brown. Renormalization group approach to neutron matter: quasiparticle interactions, superfluid gaps and the equation of state. *Nucl. Phys. A* **713**:191, 2003.
- [36] S. Gandolfi, A. Y. Illarionov, F. Pederiva, K. E. Schmidt, and S. Fantoni. Equation of state of low-density neutron matter, and the  $^1S_0$  pairing gap. *Phys. Rev. C* **80**(4):045802, 2009.
- [37] A. Gezerlis and J. Carlson. Low-density neutron matter. *Phys. Rev. C* **81**(2):025803, 2010.
- [38] E. Vigezzi, F. Barranco, R. A. Broglia, G. Colò, G. Gori, and F. Ramponi. Pairing correlations in the inner crust of neutron stars. *Nucl. Phys. A* **752**:600, 2005.
- [39] M. Baldo, U. Lombardo, É. E. Saperstein, and S. V. Tolokonnikov. Self-consistent description of the inner crust of a neutron star with allowance for superfluidity effects. *Physics of Atomic Nuclei* **68**:1812, 2005.
- [40] J. Margueron and N. Sandulescu. Pairing Correlations and Thermodynamic Properties of Inner Crust Matter. In *Neutron Star Crust*, C. A. Bertulani and J. Piekarewicz, editors. Nova Publisher, 2012. [arXiv:1201.2774].

- [41] N. Chamel, J. M. Pearson, and S. Goriely. Pairing: from atomic nuclei to neutron-star crusts. In *50 Years of Nuclear BCS: Pairing in Finite Systems*, R. A. Broglia and V. Zelevinsky, editors. World Scientific, 2013. [arXiv:1204.2076].
- [42] N.-C. Chao, J. W. Clark, and C.-H. Yang. Proton superfluidity in neutron-star matter. *Nucl. Phys. A* **179**:320, 1972.
- [43] T. Takatsuka. Proton Superfluidity in Neutron-Star Matter. *Prog. Theor. Phys.* **50**:1754, 1973.
- [44] L. Amundsen and E. Østgaard. Superfluidity of neutron matter (I). Singlet pairing. *Nucl. Phys. A* **437**:487, 1985.
- [45] Ø. Elgarøy, L. Engvik, M. Hjorth-Jensen, and E. Osnes. Model-space approach to  $^1S_0$  neutron and proton pairing in neutron star matter with the Bonn meson-exchange potentials. *Nucl. Phys. A* **604**:466, 1996.
- [46] M. Baldo and H.-J. Schulze. Proton pairing in neutron stars. *Phys. Rev. C* **75**(2):025802, 2007.
- [47] L. G. Cao, U. Lombardo, and P. Schuck. Screening effects in superfluid nuclear and neutron matter within Brueckner theory. *Phys. Rev. C* **74**(6):064301, 2006.
- [48] M. Baldo, Ø. Elgarøy, L. Engvik, M. Hjorth-Jensen, and H.-J. Schulze.  $^3P_2$ - $^3F_2$  pairing in neutron matter with modern nucleon-nucleon potentials. *Phys. Rev. C* **58**:1921, 1998.
- [49] X.-R. Zhou, H.-J. Schulze, E.-G. Zhao, F. Pan, and J. P. Draayer. Pairing gaps in neutron stars. *Phys. Rev. C* **70**(4):048802, 2004.
- [50] A. Schwenk and B. Friman. Polarization Contributions to the Spin Dependence of the Effective Interaction in Neutron Matter. *Phys. Rev. Lett.* **92**(8):082501, 2004.
- [51] D. Page, J. M. Lattimer, M. Prakash, and A. W. Steiner. Minimal Cooling of Neutron Stars: A New Paradigm. *Astrophys. J. Suppl.* **155**:623, 2004.
- [52] D. Page, J. M. Lattimer, M. Prakash, and A. W. Steiner. Neutrino Emission from Cooper Pairs and Minimal Cooling of Neutron Stars. *Astrophys. J.* **707**:1131, 2009.
- [53] D. Page, M. Prakash, J. M. Lattimer, and A. W. Steiner. Rapid Cooling of the Neutron Star in Cassiopeia A Triggered by Neutron Superfluidity in Dense Matter. *Phys. Rev. Lett.* **106**(8):081101, 2011.
- [54] M. Hoffberg, A. E. Glassgold, R. W. Richardson, and M. Ruderman. Anisotropic Superfluidity in Neutron Star Matter. *Phys. Rev. Lett.* **24**:775, 1970.

- [55] T. Takatsuka. Energy Gap in Neutron-Star Matter. *Prog. Theor. Phys.* **48**:1517, 1972.
- [56] W. Zuo, C. X. Cui, U. Lombardo, and H.-J. Schulze. Three-body force effect on  $^3\text{PF}_2$  neutron superfluidity in neutron matter, neutron star matter, and neutron stars. *Phys. Rev. C* **78**(1):015805, 2008.
- [57] D. Page and J. H. Applegate. The cooling of neutron stars by the direct URCA process. *Astrophys. J. Lett.* **394**:L17, 1992.
- [58] T. Takatsuka and R. Tamagaki. Nucleon Superfluidity in Neutron Star Core with Direct URCA Cooling. *Prog. Theor. Phys.* **97**:345, 1997.
- [59] M. Prakash, M. Prakash, J. M. Lattimer, and C. J. Pethick. Rapid cooling of neutron stars by hyperons and Delta isobars. *Astrophys. J. Lett.* **390**:L77, 1992.
- [60] W. Chen, B.-J. Li, D.-H. Wen, and L.-G. Liu.  $^3\text{P}_2$  superfluidity in neutron star matter. *Phys. Rev. C* **77**(6):065804, 2008.
- [61] M. Prakash. The nuclear equation of state and neutron stars. In A. Ansari and L. Satpathy, editors, *The Nuclear Equation of State*, page 229. World Scientific Publishing Co, 1996.
- [62] S. Balberg and N. Barnea. S-wave pairing of  $\Lambda$  hyperons in dense matter. *Phys. Rev. C* **57**:409, 1998.
- [63] A. Gal and E. Hungerford. Proceedings of the eighth international conference on hypernuclear and strange particle physics. *Nucl. Phys. A* **754**:1, 2005.
- [64] O. Hashimoto and H. Tamura. Spectroscopy of lambda hypernuclei. *Prog. Part. Nucl. Phys.* **57**:564, 2006.
- [65] C. J. Batty, E. Friedman, and A. Gal. Strong interaction physics from hadronic atoms. *Phys. Rep.* **287**:385, 1997.
- [66] S. R. Beane, E. Chang, S. D. Cohen, W. Detmold, H.-W. Lin, T. C. Luu, K. Orginos, A. Parreño, M. J. Savage, and A. Walker-Loud. Hyperon-nucleon interactions from quantum chromodynamics and the composition of dense nuclear matter. *Phys. Rev. Lett.* **109**:172001, 2012.
- [67] I. Vidaña and L. Tolós. Superfluidity of  $\Sigma^-$  hyperons in  $\beta$ -stable neutron star matter. *Phys. Rev. C* **70**(2):028802, 2004.
- [68] T. Takatsuka, S. Nishizaki, Y. Yamamoto, and R. Tamagaki. Occurrence of Hyperon Superfluidity in Neutron Star Cores. *Prog. Theor. Phys.* **115**:355, 2006.
- [69] Y. N. Wang and H. Shen. Superfluidity of  $\Lambda$  hyperons in neutron stars. *Phys. Rev. C* **81**(2):025801, 2010.



- [70] D. G. Yakovlev and K. P. Levenfish. Modified URCA process in neutron star cores. *Astron. & Astrophys.* **297**:717, 1995.
- [71] E. Flowers, M. Ruderman, and P. Sutherland. Neutrino pair emission from finite-temperature neutron superfluid and the cooling of young neutron stars. *Astrophys. J.* **205**:541, 1976.
- [72] D. N. Voskresenskii and A. V. Senatorov. Neutrino emission by neutron stars. *Zh. Eksp. Teor. Fiz.* **90**:1505, 1986.
- [73] J. C. Collins and M. J. Perry. Superdense matter: Neutrons or asymptotically free quarks? *Phys. Rev. Lett.* **34**:1353, 1975.
- [74] F. Wilczek. Asymptotic Freedom: From Paradox to Paradigm. *Proc. Nat. Acad. Sci.* **102**(24):84038413, 2005.
- [75] *Lattice 2011: Proceedings of the XXIX International Symposium on Lattice Field Theory*, 2011. SISSA, Proceedings of Science.
- [76] A. R. Bodmer. Collapsed nuclei. *Phys. Rev. D* **4**:1601, 1971.
- [77] E. Witten. Cosmic separation of phases. *Phys. Rev. D* **30**:272, 1984.
- [78] E. Farhi and R. L. Jaffe. Strange matter. *Phys. Rev. D* **30**:2379, 1984.
- [79] C. Alcock, E. Farhi, and A. Olinto. Strange stars. *Astrophys. J.* **310**:261, 1986.
- [80] P. Haensel, J. L. Zdunik, and R. Schaefer. Strange quark stars. *Astron. & Astrophys.* **160**:121, 1986.
- [81] B. C. Barrois. Superconducting quark matter. *Nucl. Phys. B* **129**:390, 1977.
- [82] D. Bailin and A. Love. Superfluid quark matter. *J. Phys. A: Math. Gen.* **12**:L283, 1979.
- [83] M. Alford, K. Rajagopal, and F. Wilczek. QCD at finite baryon density: nucleon droplets and color superconductivity. *Phys. Lett. B* **422**:247, 1998.
- [84] R. Rapp, T. Schäfer, E. V. Shuryak, and M. Velkovsky. Diquark bose condensates in high density matter and instantons. *Phys. Rev. Lett.* **81**: 53, 1888.
- [85] M. Alford, A. Schmitt, K. Rajagopal, and T. Schäfer. Color superconductivity in dense quark matter. *Rev. Mod. Phys.* **80**:1455, 2008.
- [86] J. Polchinski. Effective field theory and the Fermi surface. *arXiv:hep-th/9210046*, 1999.
- [87] R. Shankar. Renormalization-group approach to interacting fermions. *Rev. Mod. Phys.* **66**:129, 1994.

- [88] D. K. Hong. An effective field theory of QCD at high density. *Phys. Lett. B* **473**:118, 2000.
- [89] T. Schäfer. Hard loops, soft loops, and high density effective field theory. *Nucl. Phys. A* **728**:251, 2003.
- [90] Y. Nambu and G. Jona-Lasinio. Dynamical Model of Elementary Particles Based on an Analogy with Superconductivity. I. *Phys. Rev.* **122**:345, 1961.
- [91] T. Hatsuda and T. Kunhiro. QCD phenomenology based on a chiral effective lagrangian. *Phys. Rev.* **247**:221, 1994.
- [92] M. Buballa. NJL-model analysis of dense quark matter. *Phys. Rep.* **407**:205, 2005.
- [93] A. W. Steiner, S. Reddy, and M. Prakash. Color-neutral superconducting quark matter. *Phys. Rev. D* **66**:094007, 2002.
- [94] G. 't Hooft. Symmetry breaking through Bell-Jackiw anomalies. *Phys. Rev. Lett.* **37**:8, 1976.
- [95] M. Buballa and M. Oertel. Quark droplets in the NJL mean field. *Nucl. Phys. A* **642**:39, 1998.
- [96] I. Shovkovy and M. Huang. Gapless two-flavor color superconductor. *Phys. Lett. B* **564**:205, 2003.
- [97] P. F. Bedaque and T. Schäfer. High-density quark matter under stress. *Nucl. Phys. A* **697**:802, 2002.
- [98] T. Schäfer. Quark matter. In *Quarks and Mesons*, A. B. Santra *et al.*, editors. Narosa Publishing House, New Dehli, 2004. [arXiv:hep-ph/0304281].
- [99] P. Fulde and R. A. Ferrell. Superconductivity in a strong spin-exchange field. *Phys. Rev.* **135**:A550, 1964.
- [100] A. I. Larkin and Y. N. Ovchinnikov. Inhomogeneous state of superconductors. *Sov. Phys. JETP* **20**:762, 1965.
- [101] M. Alford, J. A. Bowers, and K. Rajagopal. Crystalline color superconductivity. *Phys. Rev. D* **63**:074016, 2001.
- [102] M. Alford, M. Braby, M. W. Paris, and S. Reddy. Hybrid stars that masquerade as neutron stars. *Astrophys. J.* **629**:969, 2005.
- [103] D. G. Yakovlev, A. D. Kaminker, O. Y. Gnedin, and P. Haensel. Neutrino emission from neutron stars. *Phys. Rep.* **354**:1, 2001.
- [104] D. N. Voskresensky. Neutrino Cooling of Neutron Stars: Medium Effects. In *Physics of Neutron Star Interiors*, D. Blaschke, N. K. Glendenning, & A. Sedrakian, editors. *Lecture Notes in Physics*, vol. 578, page 467. Springer Verlag, 2001. [arXiv:astro-ph/0101514].

- [105] J. M. Lattimer, M. Prakash, C. J. Pethick, and P. Haensel. Direct URCA process in neutron stars. *Phys. Rev. Lett.* **66**:2701, 1991.
- [106] B. L. Friman and O. V. Maxwell. Neutrino emissivities of neutron stars. *Astrophys. J.* **232**:541, 1979.
- [107] E. G. Flowers, P. G. Sutherland, and J. R. Bond. Neutrino pair bremsstrahlung by nucleons in neutron-star matter. *Phys. Rev. D* **12**:315, 1975.
- [108] N. Iwamoto. Neutrino emissivities and mean free paths of degenerate quark matter. *Ann. Phys.* **141**:1, 1982.
- [109] O. Maxwell, G. E. Brown, D. K. Campbell, R. F. Dashen, and J. T. Manassah. Beta decay of pion condensates as a cooling mechanism for neutron stars. *Astrophys. J.* **216**:77, 1977.
- [110] G. E. Brown, K. Kubodera, D. Page, and P. Pizzochero. Strangeness condensation and cooling of neutron stars. *Phys. Rev. D* **37**:2042, 1988.
- [111] D. N. Voskresensky and A. V. Senatorov. Description of nuclear interaction in the Keldysh diagram technique and neutrino luminosity of neutron stars. *Sov. J. Nucl. Phys.* **45**:411, 1987.
- [112] A. V. Senatorov and D. N. Voskresensky. Collective excitations in nucleonic matter and the problem of cooling of neutron stars. *Phys. Lett. B* **184**:119, 1987.
- [113] C. Schaab, D. Voskresensky, A. D. Sedrakian, F. Weber, and M. K. Weigel. Impact of medium effects on the cooling of non-superfluid and superfluid neutron stars. *Astron. & Astrophys.* **321**:591, 1997.
- [114] D. Page. Thermal Evolution of Isolated Neutron Stars. In *The Many Faces of Neutron Stars*. R. Buccheri, J. van Paradijs, & A. Alpar, editors. NATO ASIC Proc. 515, page 539, 1998. [arXiv:astro-ph/9802171].
- [115] L. B. Leinson and A. Pérez. Vector current conservation and neutrino emission from singlet-paired baryons in neutron stars. *Phys. Lett. B* **638**:114, 2006.
- [116] A. W. Steiner and S. Reddy. Superfluid response and the neutrino emissivity of neutron matter. *Phys. Rev. C* **79**(1):015802, 2009.
- [117] D. G. Yakovlev, A. D. Kaminker, and K. P. Levenfish. Neutrino emission due to Cooper pairing of nucleons in cooling neutron stars. *Astron. & Astrophys.* **343**:650, 1999.
- [118] P. Jaikumar and M. Prakash. Neutrino pair emission from Cooper pair breaking and recombination in superfluid quark matter. *Phys. Lett. B* **516**:345, 2001.

- [119] G. Baym and C. Pethick. *Landau Fermi-Liquid theory*. Wiley-VCH, 2004.
- [120] R. W. Romani. Model atmospheres for cooling neutron stars. *Astrophys. J.* **313**:718, 1987.
- [121] D. Page. Surface temperature of a magnetized neutron star and interpretation of the ROSAT data. I. Dipolar fields. *Astrophys. J.* **442**:273, 1995.
- [122] E. H. Gudmundsson, C. J. Pethick, and R. I. Epstein. Structure of neutron star envelopes. *Astrophys. J.* **272**:286, 1983.
- [123] D. Page, U. Geppert, and F. Weber. The cooling of compact stars. *Nucl. Phys. A* **777**:497, 2006.
- [124] J. M. Lattimer, K. A. van Riper, M. Prakash, and M. Prakash. Rapid cooling and the structure of neutron stars. *Astrophys. J.* **425**:802, 1994.
- [125] M. Prakash, J. M. Lattimer, and T. L. Ainsworth. Equation of state and the maximum mass of neutron stars. *Phys. Rev. Lett.* **61**:2518, 1988.
- [126] D. Page. Pairing and the Cooling of Neutron Stars. In *50 Years of Nuclear BCS: Pairing in Finite Systems*, R. A. Broglia and V. Zelevinsky, editors. World Scientific, 2013. [arXiv:1206.5011].
- [127] A. Y. Potekhin and D. G. Yakovlev. Thermal structure and cooling of neutron stars with magnetized envelopes. *Astron. & Astrophys.* **374**:213, 2001.
- [128] U. Geppert, M. Küker, and D. Page. Temperature distribution in magnetized neutron star crusts. *Astron. & Astrophys.* **426**:267, 2004.
- [129] J. F. Pérez-Azorín, J. A. Miralles, and J. A. Pons. Anisotropic thermal emission from magnetized neutron stars. *Astron. & Astrophys.* **451**:1009, 2006.
- [130] U. Geppert, M. Küker, and D. Page. Temperature distribution in magnetized neutron star crusts. II. The effect of a strong toroidal component. *Astron. & Astrophys.* **457**:937, 2006.
- [131] D. Page, U. Geppert, and M. Küker. Cooling of neutron stars with strong toroidal magnetic fields. *Astrophys. & Sp. Sci.* **308**:403, 2007.
- [132] D. N. Aguilera, J. A. Pons, and J. A. Miralles. 2D Cooling of magnetized neutron stars. *Astron. & Astrophys.* **486**:255, 2008.
- [133] D. L. Kaplan, D. A. Frail, B. M. Gaensler, E. V. Gotthelf, S. R. Kulkarni, P. O. Slane, and A. Nechita. An X-Ray Search for Compact Central Sources in Supernova Remnants. I. SNRS G093.3+6.9, G315.4-2.3, G084.2+0.8, and G127.1+0.5. *Astrophys. J. Suppl.* **153**:269, 2004.

- [134] P. Chang and L. Bildsten. Evolution of Young Neutron Star Envelopes. *Astrophys. J.* **605**:830, 2004.
- [135] D. Page, M. Prakash, J. M. Lattimer, and A. W. Steiner. Prospects of Detecting Baryon and Quark Superfluidity from Cooling Neutron Stars. *Phys. Rev. Lett.* **85**:2048, 2000.
- [136] M. E. Gusakov, A. D. Kaminker, D. G. Yakovlev, and O. Y. Gnedin. Enhanced cooling of neutron stars via Cooper-pairing neutrino emission. *Astron. & Astrophys.* **423**:1063, 2004.
- [137] A. D. Kaminker, M. E. Gusakov, D. G. Yakovlev, and O. Y. Gnedin. Minimal models of cooling neutron stars with accreted envelopes. *Mon. Not. R. Astron. Soc.* **365**:1300, 2006.
- [138] C. O. Heinke, P. G. Jonker, R. Wijnands, C. J. Deloye, and R. E. Taam. Further Constraints on Thermal Quiescent X-Ray Emission from SAX J1808.4-3658. *Astrophys. J.* **691**:1035, 2009.
- [139] P. G. Jonker, D. Steeghs, D. Chakrabarty, and A. M. Juett. The Cold Neutron Star in the Soft X-Ray Transient 1H 1905+000. *Astrophys. J. Lett.* **665**:L147, 2007.
- [140] J. M. Lattimer. The nuclear equation of state and neutron star masses. *Annu. Rev. Nucl. Part. Phys.* **62**:485, 2012.
- [141] C. L. Fryer and V. Kalogera. Theoretical Black Hole Mass Distributions. *Astrophys. J.* **554**:548, 2001.
- [142] W. B. Ashworth, Jr. A Probable Flamsteed Observations of the Cassiopeia-A Supernova. *J. Hist. Astron.* **11**:1, 1980.
- [143] J. E. Reed, J. J. Hester, A. C. Fabian, and P. F. Winkler. The Three-dimensional Structure of the Cassiopeia A Supernova Remnant. I. The Spherical Shell. *Astrophys. J.* **440**:706, 1995.
- [144] R. A. Fesen, M. C. Hammell, J. Morse, R. A. Chevalier, K. J. Borkowski, M. A. Dopita, C. L. Gerardy, S. S. Lawrence, J. C. Raymond, and S. van den Bergh. The Expansion Asymmetry and Age of the Cassiopeia A Supernova Remnant. *Astrophys. J.* **645**:283, 2006.
- [145] O. Krause, S. M. Birkmann, T. Usuda, T. Hattori, M. Goto, G. H. Rieke, and K. A. Misselt. The Cassiopeia A Supernova Was of Type IIb. *Science* **320**:1195, 2008.
- [146] R. Willingale, J. A. M. Bleeker, K. J. van der Heyden, and J. S. Kaastra. The mass and energy budget of Cassiopeia A. *Astron. & Astrophys.* **398**:1021, 2003.
- [147] R. A. Chevalier and J. Oishi. Cassiopeia A and Its Clumpy Presupernova Wind. *Astrophys. J. Lett.* **593**:L23, 2003.

- [148] B. van Veelen, N. Langer, J. Vink, G. García-Segura, and A. J. van Marle. The hydrodynamics of the supernova remnant Cassiopeia A. The influence of the progenitor evolution on the velocity structure and clumping. *Astron. & Astrophys.* **503**:495, 2009.
- [149] P. A. Young, C. L. Fryer, A. Hungerford, D. Arnett, G. Rockefeller, F. X. Timmes, B. Voit, C. Meakin, and K. A. Eriksen. Constraints on the Progenitor of Cassiopeia A. *Astrophys. J.* **640**:891, 2006.
- [150] G. G. Pavlov, D. Sanwal, and M. A. Teter. Central Compact Objects in Supernova Remnants. In *Young Neutron Stars and Their Environments*, F. Camilo & B. M. Gaensler, editors. *IAU Symposium*, vol. 218 page 239, 2004. [arXiv:astro-ph/0311526].
- [151] W. C. G. Ho and C. O. Heinke. A neutron star with a carbon atmosphere in the Cassiopeia A supernova remnant. *Nature* **462**:71, 2009.
- [152] C. O. Heinke and W. C. G. Ho. Direct Observation of the Cooling of the Cassiopeia A Neutron Star. *Astrophys. J. Lett.* **719**:L167, 2010.
- [153] P. S. Shternin, D. G. Yakovlev, C. O. Heinke, W. C. G. Ho, and D. J. Patnaude. Cooling neutron star in the Cassiopeia A supernova remnant: evidence for superfluidity in the core. *Mon. Not. R. Astron. Soc.* **412**:L108, 2011.
- [154] D. G. Yakovlev, W. C. G. Ho, P. S. Shternin, C. O. Heinke, and A. Y. Potekhin. Cooling rates of neutron stars and the young neutron star in the Cassiopeia A supernova remnant. *Mon. Not. R. Astron. Soc.* **411**:1977, 2011.
- [155] P. S. Shternin, D. G. Yakovlev, P. Haensel, and A. Y. Potekhin. Neutron star cooling after deep crustal heating in the X-ray transient KS 1731-260. *Mon. Not. R. Astron. Soc.* **382**:L43, 2007.
- [156] E. F. Brown and A. Cumming. Mapping Crustal Heating with the Cooling Light Curves of Quasi-Persistent Transients. *Astrophys. J.* **698**:1020, 2009.
- [157] C. J. Horowitz, O. L. Caballero, and D. K. Berry. Thermal conductivity and phase separation of the crust of accreting neutron stars. *Phys. Rev. E* **79**(2):026103, 2009.
- [158] J. Daligault and S. Gupta. Electron-Ion Scattering in Dense Multi-Component Plasmas: Application to the Outer Crust of an Accreting Neutron Star. *Astrophys. J.* **703**:994, 2009.
- [159] D. Blaschke, H. Grigorian, D. N. Voskresensky, and F. Weber. Cooling of the neutron star in Cassiopeia A. *Phys. Rev. C* **85**(2):022802, 2012.
- [160] F. Pacini. Rotating Neutron Stars, Pulsars and Supernova Remnants. *Nature* **219**:145, 1968.

- [161] J. E. Gunn and J. P. Ostriker. Magnetic Dipole Radiation from Pulsars. *Nature* **221**:454, 1969.
- [162] P. Goldreich and W. H. Julian. Pulsar Electrodynamics. *Astrophys. J.* **157**:869, 1969.
- [163] I. Contopoulos, D. Kazanas, and C. Fendt. The Axisymmetric Pulsar Magnetosphere. *Astrophys. J.* **511**:351, 1999.
- [164] A. Spitkovsky. Pulsar Magnetosphere: The Incredible Machine. In *40 Years of Pulsars: Millisecond Pulsars, Magnetars and More*, C. Bassa, Z. Wang, A. Cumming, and V. M. Kaspi, editors. *American Institute of Physics Conference Series*, vol. 983 page 20, 2008.
- [165] R. N. Manchester, G. B. Hobbs, A. Teoh, and M. Hobbs. The Australia Telescope National Facility Pulsar Catalogue. *Astron. J.* **129**:1993, 2005.
- [166] C. M. Espinoza. The spin evolution of young pulsars. In *Neutron Stars and Pulsars: Challenges and Opportunities after 80 years*, J. van Leeuwen, editor. IAUS Proceedings, vol. 291, 2012. [arXiv:1211.5276].
- [167] A. Muslimov and D. Page. Delayed switch-on of pulsars. *Astrophys. J. Lett.* **440**:L77, 1995.
- [168] W. C. G. Ho and N. Andersson. Rotational evolution of young pulsars due to superfluid decoupling. *Nature Physics* **8**:787, 2012.
- [169] C.-A. Faucher-Giguère and V. M. Kaspi. Birth and Evolution of Isolated Radio Pulsars. *Astrophys. J.* **643**:332, 2006.
- [170] U. Geppert, D. Page, and T. Zannias. Submergence and re-diffusion of the neutron star magnetic field after the supernova. *Astron. & Astrophys.* **345**:847, 1999.
- [171] C. G. Bernal, W. H. Lee, and D. Page. Hypercritical accretion onto a magnetized neutron star surface: a numerical approach. *Rev. Mex. Astron. & Astrof.* **46**:309, 2010.
- [172] C. G. Bernal, D. Page, and W. H. Lee. Hypercritical Accretion onto a New-born Neutron Star and Magnetic Field Submergence. arXiv:1212.0464, 2012.
- [173] A. Muslimov and D. Page. Magnetic and Spin History of Very Young Pulsars. *Astrophys. J.* **458**:347, 1996.
- [174] R. D. Blandford and R. W. Romani. On the interpretation of pulsar braking indices. *Mon. Not. R. Astron. Soc.* **234**:57P, 1988.
- [175] A. Melatos. Spin-down of an oblique rotator with a current-starved outer magnetosphere. *Mon. Not. R. Astron. Soc.* **288**:1049, 1997.

- [176] N. Andersson, K. Glampedakis, W. C. G. Ho, and C. M. Espinoza. Pulsar Glitches: The Crust is not Enough. *Phys. Rev. Lett.* **109(24)**:241103, 2012.
- [177] C. M. Espinoza, A. G. Lyne, B. W. Stappers, and M. Kramer. A study of 315 glitches in the rotation of 102 pulsars. *Mon. Not. R. Astron. Soc.*, **414**:1679, 2011.
- [178] P. W. Anderson and N. Itoh. Pulsar glitches and restlessness as a hard superfluidity phenomenon. *Nature* **256**:25, 1975.
- [179] M. Ruderman. Crust-breaking by neutron superfluids and the VELA pulsar glitches. *Astrophys. J.* **203**:213, 1976.
- [180] D. Pines and M. A. Alpar. Superfluidity in neutron stars. *Nature* **316**:27, 1985.
- [181] P. M. McCulloch, A. R. Klekociuk, P. A. Hamilton, and G. W. R. Royle. Daily observations of three period jumps of the VELA pulsar. *Australian J. of Phys.* **40**:725, 1987.
- [182] J. M. Cordes, G. S. Downs, and J. Krause-Polstorff. JPL pulsar timing observations. V - MACRO and microjumps in the VELA pulsar 0833-45. *Astrophys. J.* **330**:847, 1988.
- [183] B. Link, R. I. Epstein, and J. M. Lattimer. Pulsar Constraints on Neutron Star Structure and Equation of State. *Phys. Rev. Lett.* **83**:3362, 1999.
- [184] N. Chamel. Crustal Entrainment and Pulsar Glitches. *Phys. Rev. Lett.* **110(1)**:011101, 2012.
- [185] B. Link. Observable core response in neutron star spin glitches. arXiv:1211.2209, 2012.
- [186] T. Sidery and M. A. Alpar. The effect of quantized magnetic flux lines on the dynamics of superfluid neutron star cores. *Mon. Not. R. Astron. Soc.* **400**:1859, 2009.